

Biodiversity and dynamics of direction finding accuracy in bat biosonar

Syed Uzair Gilani

Dissertation submitted to the Faculty of the
Virginia Polytechnic Institute and State University
in partial fulfillment of the requirements for the degree of

Doctor of Philosophy
in
Electrical Engineering

Rolf Müller, Co-Chair
William T Baumann, Co-Chair
Richard Buehrer
Ting Chung Poon
Dhruv Batra

Feb 18th, 2015
Blacksburg, Virginia

Keywords: Biodiversity, Dynamics, Bats
Copyright 2016, Syed Uzair Gilani

Biodiversity and dynamics of direction finding accuracy in bat biosonar

Syed Uzair Gilani

ABSTRACT

In the biosonar systems of bats, emitted acoustic energy and receiver sensitivity are distributed over direction and frequency through beampattern functions that have diverse and often complicated geometries. This complexity could be used by the animals to determine the direction of incoming sounds based on spectral signatures. The present study in its first part has investigated how well bat biosonar beampatterns are suited for direction finding using a measure of the smallest estimator variance that is possible for a given direction (Cramér-Rao lower bound, CRLB). CRLB values were estimated for numerical beampattern estimates derived from 330 individual shape samples, 157 noseleaves (used for emission) and 173 outer ears (pinnae). At an assumed 60 dB signal-to-noise ratio, the average value of the CRLB was 3.9° , which is similar to previous behavioral findings. Distribution for the CRLBs in individual beampatterns were found to have a positive skew indicating the existence of regions where a given beampattern does not support a high accuracy. The highest supported accuracies were for direction finding in elevation (with the exception of phyllostomid emission patterns). Beampatterns in the dataset were also characterized based upon the differences in the type of acoustic signal they are associated with, the functionality of the baffle shape producing them and their phylogeny. In the second part of the study, functionality of various local shape features was investigated under static and dynamic conditions. Each local shape feature was found to have an impact on the estimation performance of the baffle shape. Interaction of the local shape features among themselves as well as their dynamic motion produced a plethora of results, not achievable through either single features or through their static states only.

This work was supported by grants from the U.S. Army Research Office (Grant No. 451069), the National Science Foundation (Award Ids 1053130, 1362886), the National Natural Science Foundation of China (grant numbers 11374192, 11074149, and 11574183), the Fundamental Research Fund of Shandong University (No. 2014QY008) and the Government of Pakistan, establishment of Jalojai campus scholarship program.

Acknowledgments

I would like to express first, my deepest gratitude to the co-chair of my Ph.D. advising committee, Dr. Rolf Müller, for the support and guidance that I received from him during the course of my Ph.D. Obtaining a Ph.D. degree from a prestigious university such as Virginia Tech is an accomplishment that can only be achieved while standing on the shoulders of several giants. Dr. Müller is one such academic giant in the field of bioinspired technology. His support in various ways from financial to administrative, from his help in choosing my research direction to his mentoring and advice while making important decisions, was decisive in my success. I can never forget the day of my preliminary exam when I was struggling to set up the projector while the time for my exam had started and Dr. Müller helped me in it. His presence, 5 to 10 minutes before the start of any examination (both in the case of the preliminary and the final exam) was of immense psychological help to me. He was the first to reply to my polls for scheduling my preliminary exam or final exam and that was a pronouncement of his support as well as his trust in my capabilities. His excellence as a teacher, a researcher, a writer, a hardworking person who is in the lab early in the morning and leaves late at night and many other qualities will remain a source of inspiration to me for a long period of time. I would also like to thank Dr. Jin Ping (Mrs. Dr. Müller) for taking out time from her busy schedule and advising all the students in the lab.

Dr. William T Baumann is the next academic giant on my list to whom I am deeply indebted to. I got introduced to Dr. Baumann at the time of my qualifying exam when he was chairing the control group. His questions during my qualifying exam helped me immensely in improving my understanding of the problem. His clear way of thinking helped me on several occasions, ranging from the selection of my Ph.D. advising committee to the decision of taking my preliminary exams. His brief arguments in favor of taking the preliminary exams in fall 2014 instead of any reliance on unexpected promises of TA positions in the future, convinced me to go

through the exam even though I personally wanted to take it at a later date. His (and Dr. Müller 's) ability to ask difficult questions in a simple way as well as to explain the question of their fellows when appropriate has helped many students including myself in their exams. Dr. Baumann also painstakingly went through my dissertation and helped me in improving its language, figures, mathematics and the overall structure for which i am grateful to him.

Dr. Ting Chung Poon is the third academic giant on my list. He was my interim adviser during 2012 and I worked with him as a grader. His kind nature and his tendency to allow graders to work independently helped me a lot. Under his mentorship, I developed an aptitude to grade assignments generously while at the same time remaining consistent as well as meticulous in pointing out the mistakes. Such habits remain inculcated in me as I graded for other professors in the future.

Dr. Richard Buehrer is yet another important faculty member in my Ph.D. advisory committee in terms of my research. His long barrage of questions during my preliminary exam helped me understand my research question and its scope in a better way. The final exam was no different than the preliminary exam as still, the major chunk of my research somehow overlapped with the expertise of Dr. Buehrer. However, I cannot forget the happy face with which he greeted me after my final exam, which made me wonder as if Dr. Buehrer had graduated rather than me. I came to know about him through my roommate who used to mention him a lot while he was taking a course with him. Dr. Buehrer was also in his advising committee and the poor gentleman went through a similar grilling in his master's defense. In spite of this, he never questioned my choice of requesting Dr. Buehrer to be in my Ph.D. advising committee, something I would stick to as well.

The last four charismatic faculty members I would like to talk about are Dr. Dhruv Batra, Dr. Hongxiao Zhu, Dr. Daniel J. Stilwell and Dr. Sandeep Shukla. Dr. Dhurv Batra is a brilliant and an energetic young researcher from whom there was much to learn yet because of financial and time limitations I could not efficiently tie my research to his area of expertise, however, I did see his active lifestyle and would like to draw lessons from it for myself. I am also grateful to Dr. Hongxiao Zhu who introduced me to various statistical methods and guided me as I applied them to my data. Special thanks goes to Dr. Daniel J. Stilwell and Dr. Sandeep Shukla for guiding me during my initial days at Virginia tech.

I would also like to thank my lab mates, Yuan Lin, Mittu Pannala, Fu Yanqing, Anupam Kumar Gupta, Praveen, Philip Caspers, Ming Chen, Mingyi Liu, Joseph Sutlive and Todd Estep for their support.

Lastly, a lot of credit goes to the Government of Pakistan, National Science Foundation (USA), Physics department of Virginia Tech and ECE department of Virginia tech for their generous financial support, without which all this was not possible.

Contents

1	Introduction	1
1.1	Biologically inspired engineering	1
1.2	Sensing and sensors	2
1.3	Acoustic sensing and bat biosonar	2
1.4	Objectives and approach	4
1.5	Main contributions	5
1.6	Chapter outline	7
2	Biodiversity in bat biosonar	8
2.1	Introduction	8
2.2	Biodiversity in bats	9
2.3	Characterization of bat's performance	12
2.4	Beampatterns	13
2.5	Generation of beampatterns	14
2.6	Biodiversity in beampatterns	15
3	Information-theoretic analysis of beampatterns	18
3.1	Introduction	18
3.2	Estimation problem	20

3.3	Results	33
3.4	Discussion	50
4	Local shape features and dynamic motion	54
4.1	Introduction	54
4.2	Static local shape features in pinna	55
4.3	Dynamic motion in baffle shapes	59
4.3.1	Dynamic motion in pinna	61
4.3.2	Dynamic motion in noseleaf	66
4.4	Combined effect of static shape features and their dynamic motion . .	71
4.5	Discussion	73
5	Summary	74
5.1	Research findings and their brief explanation	74
5.2	Suggestions for future work	77
	References	79
	Appendices	87
A		88
A.1	Physically implemented local shape features	88
B		92
B.1	Hipposideridae (Reception beampatterns)	92
B.2	Rhinolophidae (Reception beampatterns)	93
B.3	Vespertilionidae (Reception beampatterns)	94
B.4	Pteropodidae (Reception beampatterns)	96

B.5	Megadermatidae (Reception beampatterns)	97
B.6	Molossidae (Reception beampatterns)	98
B.7	Hipposideridae (Emission beampatterns)	98
B.8	Rhinolophidae (Emission beampatterns)	99
B.9	Phyllostomidae (Emission beampatterns)	101
B.10	Nycteridae (Emission beampatterns)	102
B.11	Megadermatidae (Emission beampatterns)	103
B.12	Molossidae (Emission beampatterns)	103

List of Figures

2.1	Biodiversity in bats	10
2.2	High-resolution, three dimensional models of pinnae from different bat species.	11
2.3	High-resolution, three dimensional models of noseleaves from different bat species.	12
2.4	Orthographic projection used for the display of beampatterns.	16
2.5	Biodiversity in beampatterns.	16
3.1	Types of error ellipses.	26
3.2	Analysis of an error ellipse, aligned perfectly to the coordinate axes.	27
3.3	Analysis of an error ellipse not aligned to any coordinate axis	28
3.4	Effect of beampattern rotation on the CRLB error ellipses.	30
3.5	Interspecific diversity in the patterns of CRLB error ellipses.	33
3.6	Distributions of various metrics across all samples in the analyzed beam pattern dataset.	35
3.7	Frequency dependence of the probability density functions for a) length of minor axis, b) length of major axis, c) error anisotropy.	36
3.8	Distribution (histograms) of the shape (a) and spread (b) parameters of generalized extreme value distributions that were used for modelling minor and major axes lengths in individual samples of bats.	37
3.9	Distribution of the directions of the major axes of the error ellipses over the entire sample (emission and reception beampatterns).	39

3.10	Distribution of the directions of the major axes of the error ellipses for emission (solid lines) and reception (dashed lines) beampatterns.	40
3.11	Minimum estimation error and error anisotropy for emission and reception beampatterns in rhinolophids and hipposiderids.	42
3.12	Histogram for the values of angle, Ψ , between the points of maximum sensitivity and minimum estimation error.	43
3.13	Distribution (histograms) of the shape parameter of generalized extreme value distributions that modelled the minor and major axes lengths in CFFM and FM bats.	44
3.14	Inter family and inter duty cycle differences in the distribution of shape parameter for the reception and emission beampatterns at lower beam gain threshold of -18 dB and -30 dB respectively.	45
3.15	Circular distribution of the orientation angle of error ellipses in the case of CFFM and FM bats.	46
3.16	Interfrequency variations in the position of maximum sensitivity in reception beampatterns are much bigger in FM bats than in CFFM bats.	48
3.17	Distribution of individual samples (marked by family) with respect to average values of error ellipse size.	49
4.1	Local shape features in an actual horseshoe pinna and in its prototype.	55
4.2	Obliquely truncated cone augmented with three local shape features in a stepwise manner, thereby producing eight different prototypes.	56
4.3	Beampatterns for the truncated cone to which combination of local shape features are added in a stepwise manner.	57
4.4	Angular histogram for the direction of maximum estimation error in the case of pinna prototypes augmented with different local shape features.	58
4.5	Depiction of non rigid motion of pinna in a Horseshoe bat using high speed video images, numerical models of pinna and numerical beam-pattern estimates.	60

4.6	Depiction of the effects of bending in physical pinna on the localization performance of a bat using error ellipses plot.	62
4.7	Effects of bending in physical pinna on metric values like maximum estimation error and error anisotropy.	63
4.8	Depiction of the effects of bending in numerical pinna on the localization performance of a bat using error ellipses plot.	65
4.9	Effects of bending in numerical pinna on metric values like maximum estimation error and error anisotropy.	66
4.10	Bending of a lancet in noseleaf encodes useful sensory information that reduces estimation error.	67
4.11	Effects of a bending lancet in physical noseleaf on metric values like maximum estimation error and error anisotropy.	69
4.12	Depiction of the effects of bending in numerical noseleaf on the localization performance of a bat using error ellipses plot.	70
4.13	Effects of a bending lancet in numerical noseleaf on metric values like maximum estimation error and error anisotropy.	71
4.14	Error ellipses plot for the prototype of a horseshoe pinna carrying no local shape features.	72
4.15	Error ellipses plot for the prototype of a horseshoe pinna augmented with all the features (ridge, incision and antitragus).	72

List of Tables

2.1	Taxonomic composition of the analyzed dataset of noseleaf and pinna samples.	17
3.1	Circular standard deviation	47
A.1	Metric values for the local shape features ridge, incision, antitragus and their combinations, when the pinna is in position no. 1 (The upright position)	88
A.2	Metric values for the local shape features ridge, incision, antitragus and their combinations, when the pinna is in position no. 2.	89
A.3	Metric values for the local shape features ridge, incision, antitragus and their combinations, when the pinna is in position no. 3.	89
A.4	Metric values for the local shape features ridge, incision, antitragus and their combinations, when the pinna is in position no. 4.	90
A.5	Metric values for the local shape features ridge, incision, antitragus and their combinations, when the pinna is in position no. 5.	90
A.6	Metric values for the local shape features ridge, incision, antitragus and their combinations, when the pinna is in position no. 6.	91
A.7	Metric values for the local shape features ridge, incision, antitragus and their combinations, when the pinna is in position no. 7 (The bent position).	91
B.1	Values of major axis, minor axis and error anisotropy for the reception beampatterns in family Hipposideridae	93

B.2	Values of major axis, minor axis and error anisotropy for the reception beampatterns in family Rhinolophidae	94
B.3	Values of major axis, minor axis and error anisotropy for the reception beampattern in family Vespertilionidae	96
B.4	Values of major axis, minor axis and error anisotropy for the reception beampattern in family Pteropedia	97
B.5	Values of major axis, minor axis and error anisotropy for the reception beampatterns in family Megadermatidae	97
B.6	Values of major axis, minor axis and error anisotropy for the reception beampatterns in family Molossidae	98
B.7	Values of major axis, minor axis and error anisotropy for the emission beampatterns in family Hipposideridae	99
B.8	Values of major axis, minor axis and error anisotropy for the emission beampatterns in family Rhinolophidae	101
B.9	Values of major axis, minor axis and error anisotropy for the emission beampatterns in family Phyllostomidae	102
B.10	Values of major axis, minor axis and error anisotropy for the emission beampatterns in family Nycteridae	103
B.11	Values of major axis, minor axis and error anisotropy for the emission beampatterns in family Megadermatidae	103
B.12	Values of major axis, minor axis and error anisotropy for the emission beampatterns in family Molossidae	104

Chapter 1

Introduction

1.1 Biologically inspired engineering

Biologically inspired engineering is a scientific discipline that seeks to understand the principles of biology from an engineering perspective and applies them to engineering problems. It answers questions by taking inspiration from nature which has taken millions of years to perfect its processes. Insights provided by natural processes are useful as it assists problem solvers at various levels such as in the choice of materials, ways of putting materials together, use of materials in perceiving the environment and finally responding to it. The solutions provided by nature are effective, efficient and adaptive. Examples of engineering inspired from such solutions include aircraft wing design like ACT (Adaptive Compliant Trailing Edge) inspired from the wings of birds¹, smart combination of different flight techniques like flapping and gliding for micro aerial vehicles, the inspiration of which comes from swifts^{2;3}, methods of locomotion such as legged locomotion, limbless locomotion etc inspired from animals⁴, improvement of cutting tools through the study of self-sharpening teeth of animals⁵, improved digital displays and everlasting color inspired by the light refracting properties of butterfly wings⁶, better solar power collection inspired by the arrangement of leaves on a plant^{7;8}, better ceramics by copying the properties of seashells⁹ etc. These and many other examples of success inspired from nature are an indicator of the untapped potential existing around us. As studies in biology and engineering becomes more quantitative and complex respectively, and the evolution of many biological systems in widely different and ever changing environments is studied in detail, remarkable advancements are expected to materialize in different

fields of science and technology.

1.2 Sensing and sensors

The study of sensing and sensors has been a hot topic for several decades. Sensors in their basic form sense a change in environment and respond to it. In nature, sensors and sensing are visible in every form of life from microorganisms^{10;11;12} to larger animals¹³. It is diverse and goes beyond the visual, acoustic, olfactory and somatic sensing that humans are familiar with. Infrared receptors in snakes (that help in detecting warm blooded prey)^{14;15} and pyrophilous insects (that have infrared sensors to detect fire from large distances so as move towards it to exploit the damaged resources)^{16;17}, the electroreceptors of fish^{18;19}, the magnetoreceptors of birds^{20;21;22} and the lateral line of fish and amphibians^{23;24;25} (that help in detecting water movements and pressure gradients) are some examples. Sensory systems in nature are not only diverse but also well developed even at the levels of microorganisms, such as bacteria, which use sensing to find food, avoid poisons and to target cells. Such level of diversity and development thus provides a lot of new insight which when harnessed together with modern developments in material sciences and fabrication technology could bring major breakthroughs in many fields of science and technology.

1.3 Acoustic sensing and bat biosonar

Acoustic sensing plays a conspicuous role in biological systems as well as in engineering systems. In engineering and related fields, acoustic sensing has been applied to all types of medium (gaseous, liquid and solid) by carefully selecting the range of frequencies in the acoustic spectrum (from infrasonic to ultrasonic) together with an appropriate propagation mode (longitudinal, transverse, surface, plate etc). This has been possible primarily due to the inherent advantages that acoustic sensing enjoys over other forms of sensing (like radar, lidar etc) in different sensing tasks. For example, in smoke filled environment, fog or in turbid water, sound propagates further than electromagnetic waves²⁶. In such environments, it can also penetrate objects thereby allowing to see inside, around and through the objects that cannot be penetrated by electromagnetic waves²⁶. Additionally, sonar requires comparatively small input-output data rates as an individual ultrasonic echo signal is a function of a single independent variable (amplitude as a function of time) thus making it suitable

for small autonomous robots²⁶. Major application areas of acoustic sensing are materials characterization, structural health monitoring, acoustic and medical imaging, defect characterization, distributed acoustic sensing, defense etc. In the context of biology, acoustic sensing is used by most living organisms with some specializing it to the level of sonar. Such animals include bats, odontocetes (toothed whales and dolphins), shrews, swiftlets and oilbirds etc, with their sonar being referred to as biosonar.

A biosonar works by emission of sound waves, the echoes of which are processed by animals for navigation or foraging purposes. Such a system outperforms its man made peers in several respects, for example, such systems comprise one transmitter (nose or mouth) and two receivers (two ears) unlike human-made sonars that rely on extremely narrow beam and too many receivers for localization purposes. Other differences include the acuity of the sonar system, the power and information carrying capacity of the projected signals, beam width and the spatial resolution, the amount of auditory memory, the speed of auditory recall, the degree of coupling between the biomechanics/mechanics and signal processing systems etc²⁷. Differences like these become worth investigating especially in the case of bats and dolphins that carry the most complex and sophisticated biosonar systems in nature.

Biosonar in bats is an example of a highly capable acoustic sensory system in nature. It is remarkable not only for the performance it achieves, but also for its ability to adapt to a large range of sensing tasks, and the comparatively small size scale it operates on. For example, the efficiency with which a bat detects, localizes, tracks, identifies and finally captures a prey is only possible if bats are able to perceive the world in multidimensional spatial images that could convey information about the size, shape, distance, direction and velocity of the target etc. Such delicate spatial information is extracted by bats using acoustic signals that suffer from spreading losses, geometric losses, reflection losses etc on their way towards the target and back from the target²⁹. Despite these shortcomings, bats are yet capable of tracking and capturing insects as small as mosquitoes. They can avoid fine wires less than a millimeter in diameter³⁰, and can locate and enter small cave openings. They can travel through dense vegetation for long distances and at high speeds (over 10 m/s). Their ability to localize insects in a dynamic acoustic environment in which predator and prey are in continuous motion outperforms any man-made system³¹. Sensing strategies, therefore, discovered from a bat biosonar can be useful to technical sonars as the physical principles governing the operation of the two are same. However, such strategies cannot be applied immediately as a technical sonar and a bat biosonar differ in their goals and in the constraints under which these goals are achieved.

For example, in terms of goals, it is unlikely that a technical sonar system will be used for finding nectar in flowers. Similarly, in terms of constraints, differences exist between the tracking operations of a bat and an aircraft as an aircraft operates at a much higher speed and tracks its target over large distances²⁶. The sensing strategies discovered from the biosonar sensing can, however, be generalized to an extent that they can be applied to technical applications. After generalization, sensing strategies discovered from a bat biosonar can improve the performance of technical sonar in areas like nondestructive testing, biomedical ultrasound, burglar alarms, sensors of autonomous systems, wireless communications, land mark recognition in a natural environment and navigational aid to visually impaired people etc.

1.4 Objectives and approach

Bats are the second most diverse mammal on earth after the rodent. Their diversity in terms of kinds of habitats they live in, types of food they prey on, different forms of echolocation signals they generate provides ample evidence to support the notion that bats are a success story. Learning from their success story and applying its lessons to different fields requires characterization of bats performance. Behavioral and physiological approaches attempted at drawing lessons are too few and have a lot of drawbacks, starting with the lack of echolocation specific information about most species of bats to the non-availability of living samples, difficulty in reproducing the results, differences in a lab and an open field conditions and its impact on bats performances etc. Numerically estimating the distribution or reception of power in a frequency and direction dependent way from the 3d baffle shapes is a plausible solution to some of the problems mentioned above. Along the same lines, in the current work, a database comprising numerically generated beampatterns estimates for 330 individual shape samples, 157 noseleaves (used for emission) and 173 outer ears (pinnae) was analyzed to determine the diversity in direction finding performance of bats resulting from their beampatterns. Earlier attempts at characterizing diversity involved obtaining lower dimensional fingerprints of beampattern estimates using spherical harmonic decomposition³² and the use of the eigenbeams to describe the beampatterns³³. The former approach though successful in differentiating beampatterns did not provide readily interpretable results while the latter successful in describing beampattern shape had no information on the quantitative aspects of biosonar performance. Such aspects of performance like the magnitude and direction of error in estimating the location of a target based on the information available in beampatterns can be obtained by finding the Cramér-Rao lower bound, thus not

only achieving the capability to characterize the performances of biosonar systems of various species of bats but also finding quantitatively, the functional role played by various static and dynamic shape features in the estimation process employed by the bats. In particular, efforts are made in the current study to investigate the following questions:

- How well bat biosonar beampatterns are suited for direction finding using a measure of the smallest estimator variance that is possible for a given direction (Cramér-Rao lower bound, CRLB)
- Is it possible to characterize beampatterns into functional types (Emission or reception), acoustic signal types (Frequency Modulated denoted by FM and Constant Frequency-Frequency Modulated denoted by CFFM) and phylogenetic types based on their direction finding performance obtained from beampatterns
- When baffle shapes are practically implemented what role do simple local shape features like ridge, incision, antitragus and their combinations play in direction finding performance of baffle shapes
- Baffle shapes(ear and noseleaf) in some bats undergo rapid deformation as sound waves impinge on them. How does such deformation effect the direction finding performance of bats
- How much is the performance of local shape features in bats affected by the dynamic deformation of the baffle shapes

1.5 Main contributions

- The current work has provided for the first ever time, predictions of direction finding performance for 88 different species of bats, belonging to nine different families. The predictions were mainly described in terms of minor and major axis lengths of error ellipses as such descriptions do not require any knowledge about the frame of reference that a bat uses. The average values for the major and minor axes length, across all analyzed samples and all directions that were evaluated for each sample, supported the notion that the bat biosonar beampatterns supports fairly precise direction finding at the signal-to-noise ratio (60 dB) assumed here. The average lengths of the minor axis were 3.9

°and 2.81 °at lower beam gain thresholds of -30 dB and -18 dB respectively which are well aligned with the results of behavioral experiments (3 degrees) for angular resolution in big brown bat (*Eptesicus fuscus*). The distributions for the lengths of the major and minor axes of the error ellipses, also displayed a positive skew, indicating that bat biosonar beampatterns contain regions of comparatively low estimation accuracy. The skew could mean several things one of which is the use of prior knowledge by the bats for orienting their beampatterns so as to avoid the occurrence of targets in regions of low accuracy.

- Major differences were observed between the two types of beampatterns (emission and reception beampatterns) in terms of preferred orientation of the error ellipses. Most of the error ellipses in reception beampatterns were aligned in nearly the same direction (i-e azimuth) perhaps owing to the fact that an ear has to sense weak signals for which it has to align the region of maximum sensitivity at different frequencies together as much as possible at least in the detection phase. It also shows that the estimation accuracy obtained from the use of monaural cues is better along the elevation direction than in azimuth. In the case of noseleaf, the error ellipses were oriented in all directions with ones in the azimuth slightly more in number than in other directions. The probable reason for this asymmetry is the complementary role of noseleaf in assisting the ear in detection phase. Noseleaf serve this purpose by distributing the energy in all direction but slightly more along the elevation thus improving the signal to noise ratio in the direction in which ears are most sensitive.
- Bats can be classified broadly into two categories, based on the design of their echolocation calls. These categories are FM bats and CFFM bats. Only reception beampatterns belonging to these two groups of bats at higher beam gain thresholds were found to be distinctly different from each other in terms of the distribution of the shape parameter of the generalized extreme value distributions that modelled the minimum and maximum estimation errors. The reception beampatterns for the two groups also differed in terms of orientation of error ellipses with CFFM bats having a larger scatter in their orientation of the error ellipses than FM bats. The apparent reason for this could be the large inter frequency variations in the position of maximum sensitivity in FM bats that produces comparatively more notches and peaks and hence makes the effect of monaural cues stronger thereby making the direction finding along the elevation direction better. This can be recognized by the orientation of a large number of error ellipses in the azimuth direction in FM case.

- Local shape features like ridge, incision and antitragus were found to have a profound effect on the estimation performance of the baffle shape. Among the three, incision provided the best estimation performance while the ridge and antitragus were found to have the worst estimation performance. However, the two local shape features, ridge and antitragus together, provided the best or close to the best performance possible in combinations. Similarly, incision together with ridge provided the worst estimation performance out of all the possible four combinations of the three local shape features. Each added feature changed the directionality of the beampattern and the orientation of the error ellipses in a unique way.
- Some species of bats in the family Rhinolophidae undergo dynamic motion in their baffle shapes during the echolocation process. Two such types of dynamic motions are the motion of lancet and pinna from an upright position to the bent position. In the current work, through the analysis of beampatterns generated by numerical models as well as through physical models, it was demonstrated that dynamic motion adds new information to the bat biosonar system thereby improving its direction finding performance.

1.6 Chapter outline

The remaining chapters of this dissertation are organized as follows:

Chapter 2 discusses the concept of biodiversity and its manifestation in bats using beampatterns.

Chapter 3 discusses Cramér-Rao lower bounds and their use in direction finding accuracy of a dataset comprising beampatterns for 330 individual shape samples of bats, 157 noseleaves (used for emission) and 173 outer ears (pinnae).

Chapter 4 investigates the effect of physically implemented static local shape features, dynamically moving lancet and dynamically moving local shape features on the direction finding accuracy of bats.

Chapter 5 gives a summary of the current research findings and comments on the possible future work.

Chapter 2

Biodiversity in bat biosonar

(Parts of this chapter have been published by the author and his adviser in the Journal of Acoustic Society of America³⁴)

2.1 Introduction

According to the Convention on Biological Diversity, biodiversity is defined as: "the variability among living organisms from all sources including, inter alia, terrestrial, marine and other aquatic ecosystems and the ecological complexes of which they are a part; this includes diversity within species, between species, and of ecosystems". An example of this is a pond of water with aquatic plants, seaweeds, vertebrates or invertebrates, terrestrial, aquatic or amphibious animals along with thousands of bacteria living in the pond water, thus constituting a biodiverse ecosystem.

Biodiversity can be studied at various levels ranging from the study of species to the study of ecosystems. It involves studies at the genetic level where the differences existing within the species and between species are studied as well as studies of differences existing between habitats, ecosystems and the ways of interactions between species and their environment. Such studies have a potential to contribute immensely to the disciplines of economy, medicine, engineering, geography, environmental sciences etc.

At the species level, biodiversity mainly stems from "adaptive radiation" in which an organism diversifies rapidly into new forms as a result of changes in its environment.

Such changes produce new challenges and hence new solutions. Understanding ways in which different solutions in the biological solution space are reached by natural systems from a single starting point can act as an inspiration for the design of adaptive systems and customized technology²⁸. The research presented here is an exploratory study that uses high resolution 3d models of baffle shapes (noseleaf and pinnae, Figure 2.2, 2.3) across different species of bats for characterizing their biosonar performance. Such characterization could act as a stepping stone for the design of biosonar systems that use baffle based beamforming mechanisms instead of commonly employed array signal processing techniques.

2.2 Biodiversity in bats

Bats are the second largest mammalian order³⁵. They are found on all continents of the world except Antarctica and have colonized all but the most remote oceanic islands. They have adapted to all climates except those of extreme desert and polar regions. As with many other animals, the greatest diversity and abundance of bat species occur in tropical regions and decline as one progresses to more temperate areas³⁶. There are an estimated 1230 species of bats and their number grows annually as new species are named primarily through the splitting of the existing species based on genetic evidence. About 1000 of these 1230 species utilize some form of biosonar sensing. Some of these species are shown below:

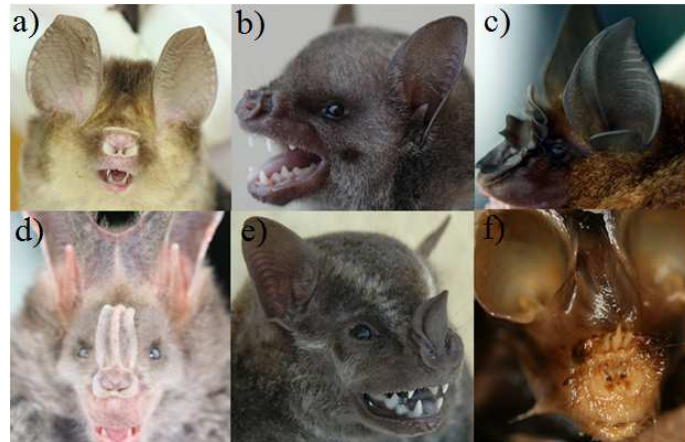


Figure 2.1: Biodiversity in bats, a) Least Leaf-nosed Bat (*Hipposideros cineraceus*) b) Antillean fruit-eating bat (*Brachyphylla cavernarum*) c) Acuminate horseshoe bat (*Rhinolophus acuminatus*) d) Greater false vampire bat (*Megaderma lyra*) e) Mexican fruit bat (*Artibeus jamaicensis*) f) Trident Bat (*Cloeotis percivali*)

The diversity apparent from Figure 2.1 exists not only in the baffle shapes of bats but also in their food sources and habitats. For example, aerial insects, arthropods, fruits, nectar, the blood of animals, fish, small terrestrial vertebrates like frogs and lizards and even other bats constitute the food sources of bats. Their habitats include caves, mines, old and abandoned buildings, tree cavities and bridges etc. Such diversity in lifestyles, in terms of their food sources and habitats, has been achieved by bats by conforming their most essential skills, their biosonar capabilities to different sensing objectives and constraints. Baffle shapes, in particular, play a major role in such adaptations.

Most species of microbats emit their echolocation signals through mouth though some use their nostrils as well. The species emitting their calls through their nostrils often have elaborate facial ornamentation. Typically, the ornaments are leaf-like and hence called noseleaves. The details of these noseleaves vary from species to species. High resolution 3d models for some noseleaves are shown in figure 2.2.

The external ear of echolocating bats is another baffle shape that serves as a receiver to collect sound. It consists of two major parts, the pinna and the tragus. The tragus is a piece of skin that stands in front of the ear canal and affects the incoming acoustic signal. The size of the tragus varies across bat species but is typically a prominent structure, particularly compared with other mammalian ears. While the

pinna is generally believed to amplify the faint sounds, the tragus helps in generating spectral cues for vertical sound localization. High resolution 3d models of ear for various species of bats are shown in the figure 2.3.

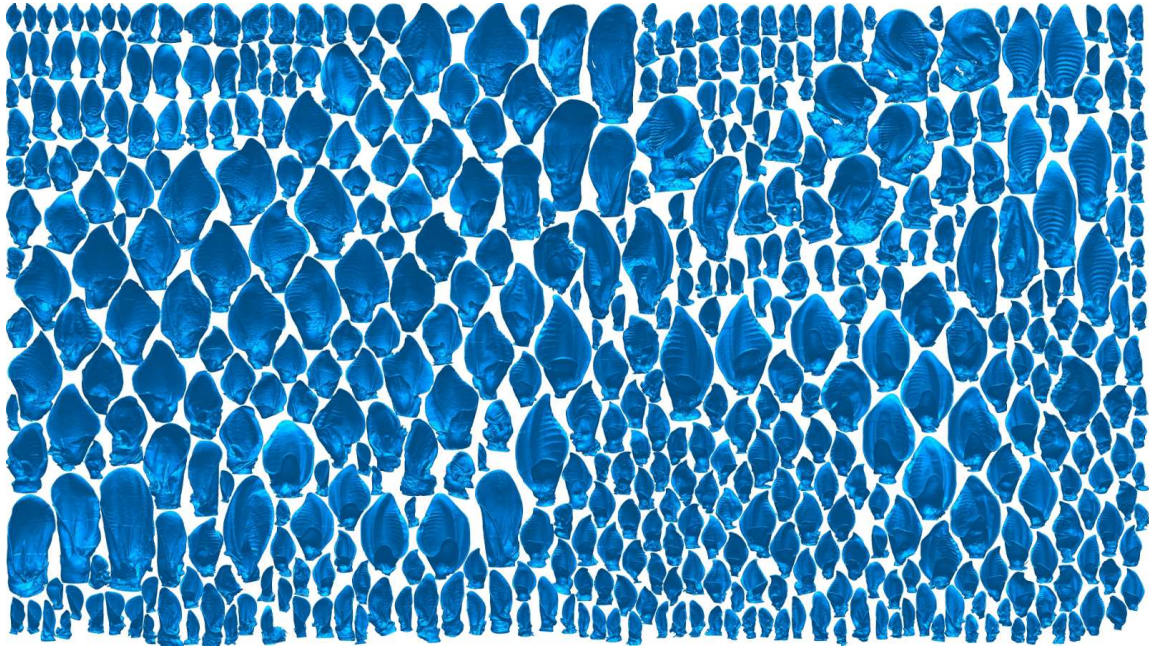


Figure 2.2: High-resolution, three dimensional models of pinnae from different bat species. Reproduced with permission from the author²⁸, Copyright 2010, Acoustical Society of America.

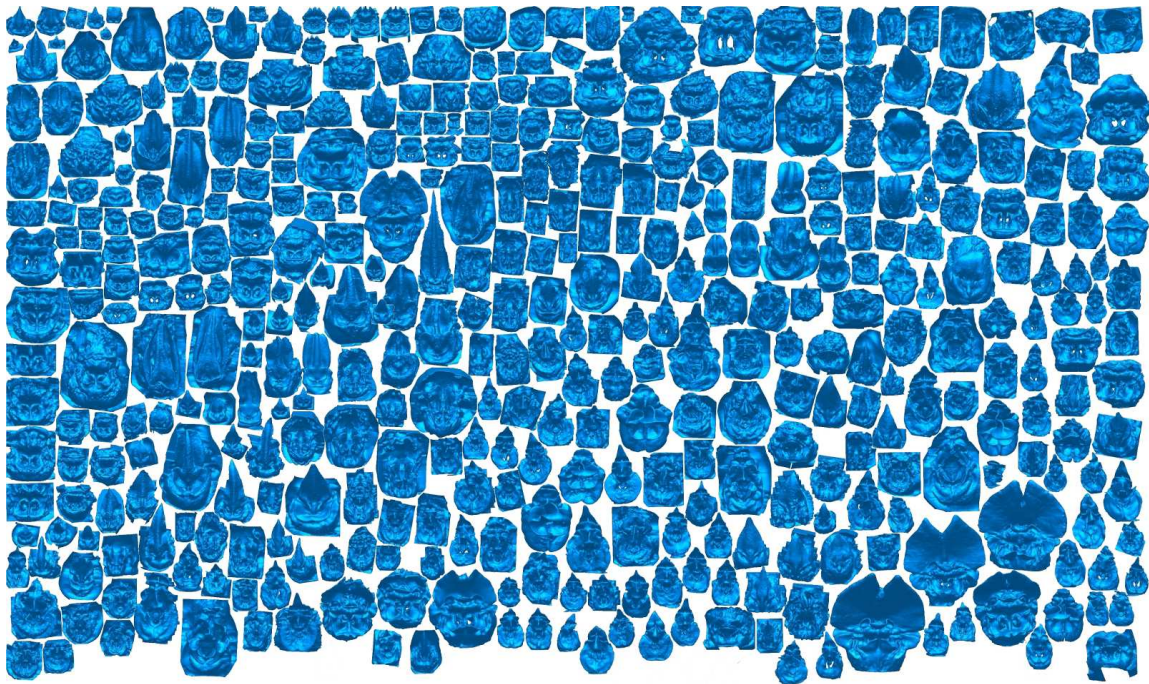


Figure 2.3: High-resolution, three dimensional models of noseleaves from different bat species. Reproduced with permission from the author²⁸, Copyright 2010, Acoustical Society of America.

2.3 Characterization of bat's performance

Echolocating bats emit sound at different rates depending upon the amount of spatial information needed from the environment. Quantifying the amount of spatial information gathered by a bat is difficult though attempts have been made to measure it indirectly. *Eptesicus fuscus*, an oral vocalizer and *Phyllostomus hastatus*, a nasal vocalizer are reported³⁷ to have the ability to distinguish one spherical target from another in the horizontal plane when the angle separating the objects is more than 6-8 degrees and 4-6 degrees respectively. Later research³⁸ shows *Eptesicus fuscus* as having the ability to distinguish angular differences in the horizontal direction down to a limit of 1.5 degrees (with 75 percent correct-response threshold) and in the vertical direction to a limit of 3 degrees to 3.5 degrees^{39;40}. The accuracy for vertical direction was calculated for targets centered at 0 degrees. At more extreme vertical positions bats showed loss of acuity; (e.g at 240 degrees, Vertical angle acuity was 6.7

degrees or 8.3 degrees and at 140 degrees, VAA was worse than 21 degrees). Other investigations⁴¹, have reported bats to have the ability to detect, localize and capture spheres as small as 1/16 inch diameter in 1/4 seconds from a distance of more than two feet. In some cases, localization accuracies of 1 cubic centimeter were achieved, even in the presence of multiple targets though the interception performance tended to degrade in the presence of massive clutter backgrounds. Similarly, echolocating bats of the species *E. fuscus* are reported⁴² to have the ability to direct their beam at a target with an accuracy of about 3 degrees in one plane. Furthermore, a directionality index has been presented⁴³ for 17 species belonging to different families of bat.

In terms of passive sound-localization, the big brown bat, *Eptesicus fuscus*, is reported⁴⁴ to have been trained and tested for discriminating left sounds from the right sounds. The results indicated an average value of the minimum audible angle to be around 14 degrees to 15 degrees. For the sound localization in two dimensions simultaneously by bats, only one investigative study⁴⁴ was found where a pallid bat was reported to land within 1 degree to its target after listening to its call (use of passive sonar) briefly from a perch 4.9 m away.

Summarizing the literature review on characterization of bats biosonar performance, most of the research cited above, provides localization accuracy for a few species of bats and that too in one dimension. The current work is the first study to apply an immediate and quantitative measure of estimation accuracy to a large and taxonomically diverse set of bat biosonar beam pattern data. The results from this study provides the first opportunity to make predictions of the direction-finding performance across many bat species and to investigate the diversity in bat biosonar beam patterns as it relates to the accuracy of direction finding.

2.4 Beampatterns

Spatial information in the form of localization accuracy can be extracted from the directivity patterns which in turn can be obtained by estimating the diffraction effects of sound from the surface geometries of 3d numerical models, representing noseleaf and pinna. A directivity pattern or beampattern describes the distribution of system's emitted power or the receiver sensitivity over direction and frequency in the far field. It is typically made up of lobes, a main lobe and sidelobes. The main lobe represents a maxima or peak in the directivity function that is separated by notches of varying depth (minima in the directivity function). At lower frequencies

with wavelengths comparatively larger than the size of the beamforming baffle, the beampattern usually consists of a single main lobe that breaks into many lobes as the wavelengths become comparable to the size of the baffle shapes. In such a case, the lobe with the highest sensitivity is referred to as the main lobe, while the weaker ones surrounding it are called sidelobes²⁸. Beampatterns of the bats are different from the beampatterns of the engineered systems in the sense that technical systems tend to have a main lobe as narrow as possible and almost no sidelobes while bats show a lot of diversity in their beampatterns in the form of location of main lobes, sidelobes, their dependency on space and frequency³².

2.5 Generation of beampatterns

Beampatterns can be measured or predicted numerically. Numerical prediction offer advantages like higher angular resolution and relative ease with which they can be estimated for different frequencies and shapes. Such beampatterns can be obtained by using the high-resolution, three-dimensional representations of noseleaf or pinna shapes, shown in Figure 2.2,2.3 which in turn can be generated by using X-ray computer tomography⁴⁵. Each sample is embedded into a computational domain meshed with cuboidal elements that represent the air volume surrounding the sample. The boundaries of the computational domain are treated as follows: All surfaces of the biological structures are assumed to be perfectly reflecting whereas the interfaces of the computational domain with the free-field are covered with infinite elements that approximate reflection-free outward propagation⁴⁶.

The cuboidal-element mesh is used to compute a finite-element approximation of the solution to the Helmholtz differential equation²⁸:

$$\nabla^2\Phi + k^2\Phi = -b \quad (2.1)$$

where Φ is the sound pressure, k the wave number, and b the force term representing sources.

The source terms for both sample types, noseleaves and pinnae, are chosen to represent monopole sources. For the noseleaves, two in-phase monopole sources are used, one for each nostril. For each pinnae model, a single monopole source is added. In either case, the source locations are chosen at the end of an artificial canal that is added to the sample to recreate the nasal tubes or the ear canal respectively^{45;47}.

The numerical solution to the Helmholtz equation is used as an estimate of the acous-

tic near field in the vicinity of the noseleaf or the pinna. To obtain the distribution of the emitted energy in the far field, a Kirchhoff integral formulation that describes sound propagation into the free field is used. In this formulation, the wave field $\Psi(x)$ at position x outside of the boundary surface S is expressed as²⁸:

$$\Psi(\vec{x}) = -\frac{1}{4\pi} \int_S \frac{e^{jkR}}{R} n[\nabla\Psi + jk(1 + \frac{j}{kR}) \frac{\mathbf{R}}{R}\Psi] dS, \quad (2.2)$$

where \vec{R} is the vector between the surface element dS and the position \vec{x} , \vec{n} is the outward pointing surface normal, Ψ the field value on S , and k the wave number. The product $n\nabla\Psi = \frac{\partial\Psi}{\partial\vec{n}}$ is the derivative of the field Ψ with respect to the surface normal \vec{n} . The positions x are chosen on a hemisphere with a radius value such that the lower boundary conditions for the far field are satisfied. Since the positions on the surface of the hemisphere differ only in direction and not in distance, the normalized field amplitudes $\Psi(x)$ are taken as estimates of the beampattern. Such numerical beampattern estimates derived from 330 individual shape samples and previously investigated^{77;32;33} were used in the current study for the purpose of analysis.

2.6 Biodiversity in beampatterns

As each noseleaf and pinnae operate in a certain frequency band therefore in the current research, beampattern estimates that were generated at 10 linearly spaced frequencies, sampled from the operating frequency band of each shape sample, were used for the purpose of analysis. The estimates were computed over a range of angles spanning 180 degrees along elevation and 360 across azimuth with a resolution of 1 degree along each direction. Orthographic projection shown in Figure 2.4 was used throughout this current work to represent beampatterns.

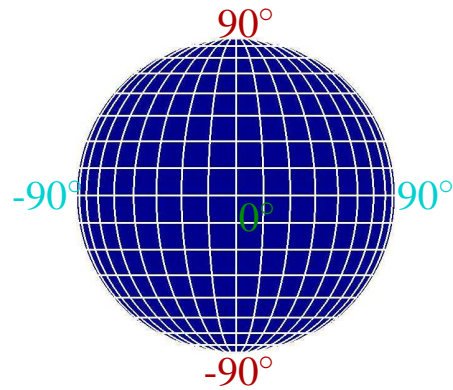


Figure 2.4: Orthographic projection used for the display of beampatterns. Numbers in red and light blue color represent elevation and azimuth values respectively. The origin is represented by a number 0 in green color. The lines of the coordinate grid are spaced 10° in azimuth and 10° in elevation.

Some of the beampatterns estimates used in the analysis are shown below

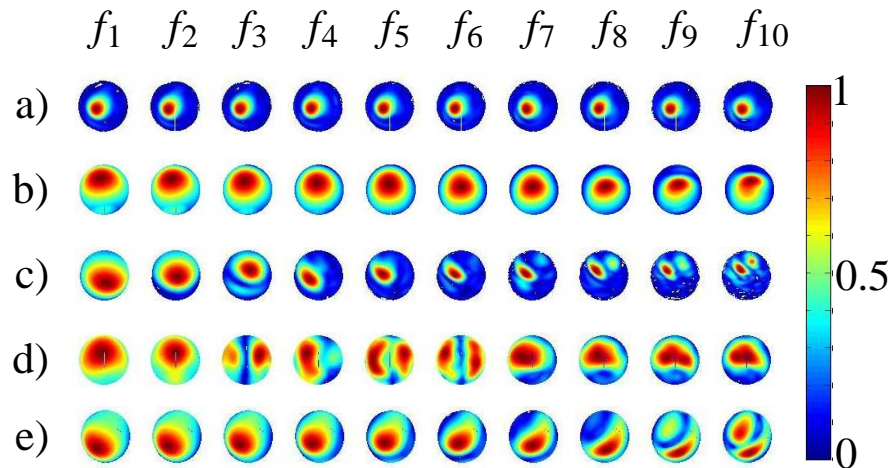


Figure 2.5: Biodiversity in beampatterns ; a) Stoliczka's trident bat (*Aselliscus stoliczkanus*), b) Asian Barbastelle bat (*Barbastella leucomelas*), c) Serotine bat (*Eptesicus serotinus*), d) Cape Leaf-nosed bat (*batHipposideros caffer*), e) Common Pipistrelle bat (*Pipistrellus pipistrellus*).

The differences between the beampattern estimates in Figure 2.5 becomes apparent,

just by inspection. For example, in Figure 2.5(a), the size of the main lobe remains almost the same with the increase in frequency. In Figure 2.5(c), the size of the lobe decreases with the increase in frequency. In Figure 2.5 (a), there is only one main lobe throughout ten frequencies while in Figure 2.5(e), the main lobe divides into two sidelobes as frequency increases. In figure 2.5(d), the main lobe divides into two lobes as frequency increases but eventually at higher frequencies the two lobes join together to form a single lobe. The shape of the main lobe also plays an important role. For example, in Figure 2.5a) the main lobe is symmetrical in shape and it retains its symmetrical shape throughout ten frequencies. In Figure 2.5 b), c), d), e) it is neither symmetrical at lower frequencies nor does it become symmetrical at higher frequencies.

In the current analysis, 283 (Table 2.1) different numerical beampattern estimates were utilized for the purpose of research. The estimates covered 88 different species in total of which 70 species belonged to four major families: Rhinolophidae, Hipposideridae, Phyllostomidae, and Vespertilionidae. The remaining 18 species were distributed over five families (s. Table 2.1). On average 3 samples were considered for analysis in the case of each noseleaf and pinnae with the maximum approaching to six. Their overall distribution is tabulated below :

Family	Species	Noseleaf samples	Pinna samples
Rhinolophidae	17	49	36
Hipposideridae	14	40	22
Vespertilionidae	25	0	89
Phyllostomidae	14	40	0
Nycteridae	8	24	0
Pteropodidae	6	0	17
Megadermatidae	2	1	1
Molossidae	1	3	3
Emballonuridae	1	0	5
total	88	157	173

Table 2.1: Taxonomic composition of the analyzed dataset of noseleaf and pinna samples.

Chapter 3

Information-theoretic analysis of beampatterns

(Parts of this chapter have been published by the author and his adviser in Journal of Acoustic Society of America³⁴)

3.1 Introduction

An important characteristic of any sonar system – including bat biosonar – is how the system distributes the emitted acoustic energy and the receiver sensitivity over direction and frequency. This can be described by a beampattern, i.e., a relative gain value for emission or reception as a function of direction and frequency. Bat biosonar beampatterns have been shown to exhibit diverse geometries with features that can be tied to the morphology of the noseleaves (for nasal emitters) and the pinna²⁸, but an understanding of the functional diversity across different bat species has yet to be accomplished. Early work⁴⁸ on beampatterns across a larger number (47) of bat species has been limited to comparing species by the overall beamwidth. However, bat biosonar beampatterns are often complicated and feature multiple lobes separated by notches for which overall beamwidth is not a good measure to capture diversity.

To reduce the complexity in the beampatterns in a more gradual and controlled fashion than can be achieved by a single scalar measure such as beamwidth, low-dimensional fingerprints of beampattern functions have been obtained by virtue of

a spherical harmonics decomposition³². Even fairly short fingerprints (e.g., with coefficients for 15 spherical harmonics) were found to capture a diversity in the beampatterns, e.g., in the form of differences between emission and reception or differences between taxonomic groups (families)³².

The central shortcoming of a low-dimensional fingerprint as provided by the spherical harmonics coefficients is that while it can be used to demonstrate the existence of differences between species groups, the nature of these differences are hard to visualize or interpret. To remedy this shortcoming, the beampattern diversity has been described in terms of eigenvectors (“eigenbeams”³³). Since the eigenbeams can be rendered in the same coordinate system as the original beampatterns, their role in producing a given beampattern shape can be easily visualized and interpreted.

The interpretation of the eigenbeams is limited to the shape of the beampatterns and is not readily linked to the performance of the biosonar system in a quantitative way. For the (bio)sonar task of finding the direction of an impinging sound based on a spectral signature, such a link can be established: A local lower bound (Cramér-Rao lower bound, CRLB) on the variance of an estimator can be computed based on the shape of the beampatterns and the signal-to-noise ratio. Examples in literature where such bounds have been calculated for engineering systems are many^{49;50;51;52}. In biological systems, two closely related examples of the use of such bound are⁵³ and⁵⁴ where in the foremost, a lower bound on the direction-finding accuracy has been obtained to quantify the effects of certain pinna features in a brown long-eared bat, *Plecotus auritus* while in the latter the amount of spatial information present in an emission beampattern simulated using piston model is being studied along with some other factors not relevant to the current work. The work reported here extends the application of ⁵³ to a much larger, species-diverse data set. In addition, the method previously described in⁵³ has been generalized to go beyond the bounds of estimation errors in a fixed coordinate system (azimuth and elevation) to find the directions of minimum or maximum error. This generalized approach hence not only yields estimates for how large the direction-finding errors could be at minimum but also in which directions the estimation performance is best or worse. The goals of this first, exploratory study are to get a sense of the CRLB values across different species of bats, to see if they have preferred directions for determining a target and how variable measures related to the CRLB are to arrive at a broader picture of how well bat biosonar beampatterns are suited for direction finding without having to conduct behavioral experiments with a large number of bat species that would require a prohibitive effort.

3.2 Estimation problem

In the present study, it has been assumed that the bat's estimate of the direction of a sonar target is based on the observation of signal amplitudes in a set of frequency channels fed by a monaural input. The noise (measurement noise/receiver noise or channel noise) in these channels is assumed to Gaussian additive noise that has been distributed independently and identically over frequency and direction. Each frequency channel is treated as a beampattern, a joint space frequency filter on the environment that carries spatial information about the sound source and the scatterers²⁸. For simplicity, a clutter-free environment, a 100 dB SPL emission level of a bat⁶⁹, a total loss of -40 dB (due to target strength and propagation), a 0 dB SPL hearing threshold⁷⁰ of a bat and a signal-to-noise ratio of 60 dB has been assumed. Under these assumptions, the spatial information encoded in various types of beampatterns can be inferred by calculating their respective Cramér-Rao lower bounds which have the most conservative (largest) values under the Gaussian noise assumption^{71;72}.

A Cramér-Rao lower bound expresses a lower bound on the variance of estimators for a deterministic parameter. In the case of beampatterns, the deterministic parameters are the location of a sound source, (θ, ϕ) . For the purpose of derivation in the current study, let $D_f(\theta, \phi)$ represents the directivity gain at a frequency channel f and a location (θ, ϕ) and $\overline{D_f(\theta, \phi)}$ is its mean value that is the measurable quantity then,

$$D_f(\theta, \phi) = \overline{D_f(\theta, \phi)} + w(0, \sigma^2) \quad (3.1)$$

Where w is the Gaussian noise with mean 0 and covariance σ^2 . Or

$$D_f(\theta, \phi) \sim \mathcal{N}(\overline{D_f(\theta, \phi)}, \sigma^2) \quad (3.2)$$

In the case of N frequencies,

$$\mathbf{D}_f(\theta, \phi) \sim \mathcal{N}(\overline{\mathbf{D}_f(\theta, \phi)}, C) \quad (3.3)$$

Where

$$\mathbf{D}_f(\theta, \phi) = \begin{bmatrix} D_{f_1}(\theta, \phi) \\ D_{f_2}(\theta, \phi) \\ \vdots \\ D_{f_N}(\theta, \phi) \end{bmatrix} \quad (3.4)$$

$$\overline{\mathbf{D}_f}(\theta, \phi) = \begin{bmatrix} \overline{D_{f_1}(\theta, \phi)} \\ \overline{D_{f_2}(\theta, \phi)} \\ \vdots \\ \overline{D_{f_N}(\theta, \phi)} \end{bmatrix} \quad (3.5)$$

and

$$C = \begin{bmatrix} \sigma^2 & 0 & 0 & \cdots & 0 \\ 0 & \sigma^2 & 0 & \cdots & 0 \\ & \vdots & & \ddots & \\ 0 & 0 & 0 & \cdots & \sigma^2 \end{bmatrix} = \sigma^2 I \quad (3.6)$$

Here C is assumed to be independent of θ and ϕ . From⁵⁵, if $\mathbf{X} \sim \mathcal{N}(\boldsymbol{\mu}(\boldsymbol{\theta}), C(\boldsymbol{\theta}))$ with $\boldsymbol{\theta}$ being a set of unknown parameters defined as $\boldsymbol{\theta} = [\theta_1 \ \theta_2 \ \dots \ \theta_p]$ then the first element of the Fisher information matrix, $[I(\boldsymbol{\theta})]_{ij}$ is given by :

$$[I(\boldsymbol{\theta})]_{ij} = \left[\frac{\partial \boldsymbol{\mu}(\boldsymbol{\theta})}{\partial \theta_i} \right]^T C^{-1}(\boldsymbol{\theta}) \left[\frac{\partial \boldsymbol{\mu}(\boldsymbol{\theta})}{\partial \theta_j} \right] + \frac{1}{2} \text{tr} \left[C^{-1}(\boldsymbol{\theta}) \frac{\partial C(\boldsymbol{\theta})}{\partial \theta_i} C^{-1}(\boldsymbol{\theta}) \frac{\partial C(\boldsymbol{\theta})}{\partial \theta_j} \right] \quad (3.7)$$

where

$$\frac{\partial \boldsymbol{\mu}(\boldsymbol{\theta})}{\partial \theta_i} = \begin{bmatrix} \frac{\partial [\boldsymbol{\mu}(\boldsymbol{\theta})]_1}{\partial \theta_i} \\ \frac{\partial [\boldsymbol{\mu}(\boldsymbol{\theta})]_2}{\partial \theta_i} \\ \vdots \\ \frac{\partial [\boldsymbol{\mu}(\boldsymbol{\theta})]_N}{\partial \theta_i} \end{bmatrix} \quad (3.8)$$

and

$$\frac{\partial \mathbf{C}(\boldsymbol{\theta})}{\partial \theta_i} = \begin{bmatrix} \frac{\partial [\mathbf{C}(\boldsymbol{\theta})]_{11}}{\partial \theta_i} & \frac{\partial [\mathbf{C}(\boldsymbol{\theta})]_{12}}{\partial \theta_i} & \cdots & \frac{\partial [\mathbf{C}(\boldsymbol{\theta})]_{1N}}{\partial \theta_i} \\ \frac{\partial [\mathbf{C}(\boldsymbol{\theta})]_{21}}{\partial \theta_i} & \frac{\partial [\mathbf{C}(\boldsymbol{\theta})]_{22}}{\partial \theta_i} & \cdots & \frac{\partial [\mathbf{C}(\boldsymbol{\theta})]_{2N}}{\partial \theta_i} \\ \vdots & & & \\ \frac{\partial [\mathbf{C}(\boldsymbol{\theta})]_{N1}}{\partial \theta_i} & \frac{\partial [\mathbf{C}(\boldsymbol{\theta})]_{N2}}{\partial \theta_i} & \cdots & \frac{\partial [\mathbf{C}(\boldsymbol{\theta})]_{NN}}{\partial \theta_i} \end{bmatrix} \quad (3.9)$$

In our case, $\mathbf{D}_f(\theta, \phi) \sim \mathcal{N}(\overline{\mathbf{D}_f(\theta, \phi)}, C)$. Hence the first element of the resulting Fisher information matrix $I(\theta, \phi)$ is given by :

$$[I(\theta, \phi)]_{1,1} = \left[\frac{\partial \overline{\mathbf{D}_f(\theta, \phi)}}{\partial \theta} \right]^T C^{-1}(\theta, \phi) \left[\frac{\partial \overline{\mathbf{D}_f(\theta, \phi)}}{\partial \theta} \right] + \frac{1}{2} \text{tr} \left[C^{-1}(\theta, \phi) \frac{\partial C(\theta, \phi)}{\partial \theta} C^{-1}(\theta, \phi) \frac{\partial C(\theta, \phi)}{\partial \theta} \right] \quad (3.10)$$

As C is not a function of θ and ϕ in the current work, therefore,

$$[I(\theta, \phi)]_{1,1} = \left[\frac{\partial \overline{\mathbf{D}_f(\theta, \phi)}}{\partial \theta} \right]^T C^{-1} \left[\frac{\partial \overline{\mathbf{D}_f(\theta, \phi)}}{\partial \theta} \right] \quad (3.11)$$

or

$$[I(\theta, \phi)]_{1,1} = \frac{1}{\sigma^2} \sum_f \left[\frac{\partial \overline{D_f(\theta, \phi)}}{\partial \theta} \right]^2 \quad (3.12)$$

Other elements of the Fisher information matrix can be derived in a similar way. The final Fisher information matrix is given by :

$$I(\theta, \phi) = \frac{1}{\sigma^2} \begin{bmatrix} \sum_f \left[\frac{\partial \overline{D_f(\theta, \phi)}}{\partial \theta} \right]^2 & \sum_f \left[\frac{\partial \overline{D_f(\theta, \phi)}}{\partial \theta} \frac{\partial \overline{D_f(\theta, \phi)}}{\partial \phi} \right] \\ \sum_f \left[\frac{\partial \overline{D_f(\theta, \phi)}}{\partial \phi} \frac{\partial \overline{D_f(\theta, \phi)}}{\partial \theta} \right] & \sum_f \left[\frac{\partial \overline{D_f(\theta, \phi)}}{\partial \phi} \right]^2 \end{bmatrix} \quad (3.13)$$

If the vectors \vec{v}_θ and \vec{v}_ϕ are defined as 3.14 below :

$$\vec{v}_\theta = \begin{bmatrix} \frac{\partial D_{f_1}(\theta, \phi)}{\partial \theta} \\ \frac{\partial D_{f_2}(\theta, \phi)}{\partial \theta} \\ \vdots \\ \frac{\partial D_{f_n}(\theta, \phi)}{\partial \theta} \end{bmatrix}, \quad \vec{v}_\phi = \begin{bmatrix} \frac{\partial D_{f_1}(\theta, \phi)}{\partial \phi} \\ \frac{\partial D_{f_2}(\theta, \phi)}{\partial \phi} \\ \vdots \\ \frac{\partial D_{f_n}(\theta, \phi)}{\partial \phi} \end{bmatrix} \quad (3.14)$$

then 3.13 can be expressed as :

$$I(\theta, \phi) = \frac{1}{\sigma^2} \begin{bmatrix} |\vec{v}_\theta|^2 & \langle \vec{v}_\theta, \vec{v}_\phi \rangle \\ \langle \vec{v}_\theta, \vec{v}_\phi \rangle & |\vec{v}_\phi|^2 \end{bmatrix} \quad (3.15)$$

The inverse of the Fisher information matrix is the covariance matrix for the direction finding errors⁵³.

$$C = [I(\theta, \phi)]^{-1} = \begin{bmatrix} \sigma_{\hat{\theta}}^2 & \sigma_{\hat{\theta}\hat{\phi}} \\ \sigma_{\hat{\theta}\hat{\phi}} & \sigma_{\hat{\phi}}^2 \end{bmatrix} \quad (3.16)$$

The two diagonal entries of the covariance matrix are the lower limits, i.e., the Cramér-Rao lower bounds⁵⁵ on the variance in the estimates of azimuth ($\hat{\theta}$) and elevation ($\hat{\phi}$) and are defined in equations 3.17 and 3.18 below, i-e

$$\sigma_{\hat{\theta}}^2 = \text{Var}(\hat{\theta}) \geq \sigma^2 \frac{|\vec{v}_\phi|^2}{|\vec{v}_\theta|^2 |\vec{v}_\phi|^2 - \langle \vec{v}_\theta, \vec{v}_\phi \rangle^2} \quad (3.17)$$

$$\sigma_{\hat{\phi}}^2 = \text{Var}(\hat{\phi}) \geq \sigma^2 \frac{|\vec{v}_\theta|^2}{|\vec{v}_\theta|^2 |\vec{v}_\phi|^2 - \langle \vec{v}_\theta, \vec{v}_\phi \rangle^2}, \quad (3.18)$$

Hence it is clear from 3.17 and 3.18 that the lower bounds on the estimator variance depends on the product of signal-to-noise ratio (term $\frac{1}{\sigma^2}$, here set to 60 dB) and a term that depends on the partial derivatives of the beam gains.

Direction estimates that are based on inputs taken from a function that is differentiable with respect to direction and has zero-mean noise added to it will be distributed

around the true value of the direction. Since two independent variables (direction angles) need to be estimated to determine a direction, the error can also be decomposed into two orthogonal components. One geometrical figure with two orthogonal axes that can encompass such distribution of the direction estimates is an error ellipse⁵⁶, i.e., elliptical contour lines on the surface of a sphere that delineate the set of directions into which a certain percentage of the direction estimates will fall. The major and minor axes of such an error ellipse represent the largest and the smallest component of the uncertainty present in the direction estimates and can be found from the covariance matrix of the direction-finding errors as follows:

$$(\mathbf{C} - \lambda \mathbf{I}) = \begin{bmatrix} \sigma_{\hat{\theta}}^2 - \lambda & \sigma_{\hat{\theta}\hat{\phi}} \\ \sigma_{\hat{\theta}\hat{\phi}} & \sigma_{\hat{\phi}}^2 - \lambda \end{bmatrix} = \lambda^2 - \lambda(\sigma_{\hat{\theta}}^2 + \sigma_{\hat{\phi}}^2) + \sigma_{\hat{\theta}}^2\sigma_{\hat{\phi}}^2 - \sigma_{\hat{\theta}\hat{\phi}}^2 = 0 \quad (3.19)$$

$$\Rightarrow \lambda = \frac{\sigma_{\hat{\theta}}^2 + \sigma_{\hat{\phi}}^2}{2} \pm \sqrt{\frac{(\sigma_{\hat{\theta}}^2 - \sigma_{\hat{\phi}}^2)^2}{4} + \sigma_{\hat{\theta}\hat{\phi}}^2} \quad (3.20)$$

A more rigorous derivation is available in⁵⁷. Thus, the square roots of the two eigenvalues of the covariance matrix give the lengths of the semi-major (larger eigenvalue) and semi-minor axes (smaller eigenvalue). This means that the length of the semi-major and semi-minor axes correspond to the standard deviation of the estimates along the direction of the respective axis. The axes can be scaled by a factor α to get confidence ellipses for a particular confidence level. For 68.3%(1 σ) confidence level, the value of α can be calculated as follows:

Let U be a random variable such that

$$U = \left(\frac{\Omega_{maj}}{\sigma_{\Omega_{maj}}} \right)^2 + \left(\frac{\Omega_{min}}{\sigma_{\Omega_{min}}} \right)^2 \quad (3.21)$$

where Ω_{maj} and Ω_{min} represents the coordinates of an estimate along the direction of maximum estimation error and minimum estimation error respectively while $\sigma_{\Omega_{maj}}$ and $\sigma_{\Omega_{min}}$ represent the uncertainties in each direction which are further assumed to be Gaussian for the purpose of simplicity, then U will have a Chi-square distribution with two degrees of freedom. As the probability density function for any random variable y with a Chi-square distribution, is given by:

$$f(y) = \frac{1}{2^{\frac{n}{2}} \Gamma(\frac{n}{2})} y^{\frac{n}{2}-1} e^{-\frac{y}{2}} \quad (3.22)$$

Where n represents the degrees of freedom. In the case of U with two degrees of freedom, the probability density function is given by:

$$f(u) = \frac{1}{2^{\frac{2}{2}}\Gamma(\frac{2}{2})}u^{\frac{2}{2}-1}e^{-\frac{u}{2}} \quad (3.23)$$

$$= \frac{1}{2}e^{-\frac{u}{2}} \quad (3.24)$$

The probability that a location with its coordinates represented by Ω_{maj} and Ω_{min} would fall on or inside the error ellipse is given by:

$$p = P \left[\left(\frac{\Omega_{maj}}{\sigma_{\Omega_{maj}}} \right)^2 + \left(\frac{\Omega_{min}}{\sigma_{\Omega_{min}}} \right)^2 \leq \alpha^2 \right] = P [U \leq \alpha^2] \quad (3.25)$$

$$= \int_0^{\alpha^2} \frac{1}{2}e^{-\frac{u}{2}}du \quad (3.26)$$

$$= 1 - e^{-\frac{\alpha^2}{2}} \quad (3.27)$$

or

$$\alpha = [-2\ln(1 - p)]^{\frac{1}{2}} \quad (3.28)$$

For (1σ) deviation confidence ellipse ($p= 0.683$), the value of α , from equation 3.28 comes out to be 1.52.^{58;59}

The orientation of the error ellipse is given by the eigenvectors of the covariance matrix, with the eigenvector associated with the larger eigenvalue pointing in the direction of the major axis and the other eigenvector pointing in the direction of the minor axis. Figure 3.1 shows examples of individual error ellipses.

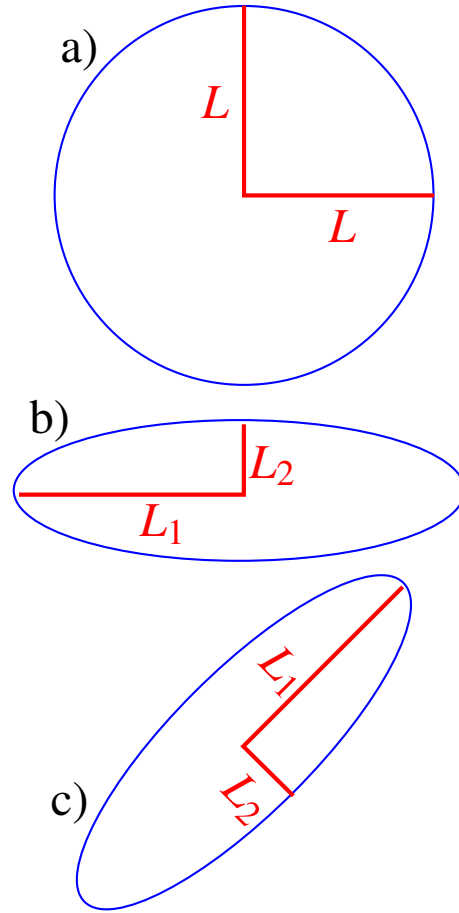


Figure 3.1: Types of error ellipses: a) circular error ellipse (representing isotropic estimation error), b) anisotropic error with the major axis aligned with one of the direction coordinate axes (azimuth), c) anisotropic error ellipse not aligned with any of the direction axes. L_1 , L_2 , and L represent the length of semi-major axis, the semi-minor axis, and the radius of the error ellipses respectively.

In the current research, error ellipses were computed over regular grid of directions that were obtained by tessellating a spherical surface into at least 49 000 curvilinear quadrilaterals using the Hierarchical Equal Area isoLatitude Pixelization of a sphere (HEALPix) library⁶⁰. Error ellipses were then computed for all these points and included in the analysis based on the respective value of the average beam gain (average over frequency). Individual error ellipses were then characterized based on four measures: (i) orientation of the error ellipse (ii) minimum estimation error (i.e.,

length of the minor axis of the error ellipses), (iii) maximum estimation error (i.e., length of the major axis of the error ellipses) and (iv) error anisotropy (ratio of major to minor axis length)

In terms of orientation, the axes of an error ellipse can be either aligned with the definition of the coordinates axes (azimuth and elevation) as shown in Figure 3.2 or can be oriented at some oblique angle with respect to them (Figure 3.3). If the axes of the error ellipses are aligned with one of the major axes, the vectors \vec{v}_θ and \vec{v}_ϕ in Eq. 3.14 become orthogonal to each other, making $\text{Var}(\theta)$ uncorrelated to $\text{Var}(\phi)$. Mathematically at a point A, in figure 3.2,

$$\text{Var}(\hat{\theta}) \geq \sigma^2 \frac{|\vec{v}_\phi|^2}{|\vec{v}_\theta|^2 |\vec{v}_\phi|^2 - \langle \vec{v}_\theta, \vec{v}_\phi \rangle^2} \quad (3.29)$$

Since in the case of Figure 3.2, $\langle \vec{v}_\theta, \vec{v}_\phi \rangle = 0$ and the vectors \vec{v}_θ and \vec{v}_ϕ are orthogonal to each other, therefore at point A, the location under consideration,

$$\text{Var}(\hat{\theta}) \geq \sigma^2 \frac{1}{|\vec{v}_\theta|} \quad (3.30)$$

This, in the context of Figure 3.2, means that the value of Cramér-Rao lower bound in direction θ is inversely related to the rate of change of directivity in the direction θ . Thus, greater the change in the magnitude of directivity along the θ axis, higher will the derivative with respect to θ and lower will be the Cramér-Rao lower bound along the θ axis.

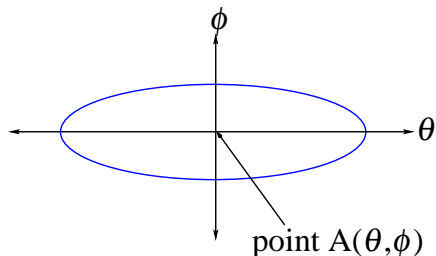


Figure 3.2: Analysis of an error ellipse, aligned perfectly to the coordinate axes. Location of point A represents the true value of the parameters. As the orientation axis of the error ellipse is aligned with the θ axis (one of the coordinate axis) therefore error across θ axis is independent of the error across ϕ axis.

Error ellipses can also have some oblique orientation that is not aligned with any of the chosen coordinate axes as shown in Figure 3.3. In such a case, if the orientation of the error ellipse represented by the principle axis of the error ellipse (arrow at an angle α with respect to θ axis) is less than 45 degrees then CRLB with respect to θ is greater than CRLB with respect to ϕ and vice versa. If the orientation angle is exactly 45 degrees then CRLB with respect to θ is equal to CRLB with respect to ϕ .

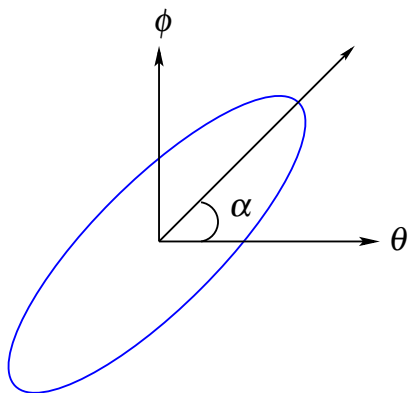


Figure 3.3: Analysis of an error ellipse not aligned to any coordinate axis. The orientation of the error ellipse, represented by the direction of its major axis is α degrees, counter clock wise with respect to θ axis. Hence, the estimation error across θ axis is correlated to the estimation error across ϕ axis.

In terms of axes length ratio, the axes of an error ellipse can either have equal or different length. If the lengths of the axes are equal, the error is isotropic and the error ellipse takes the shape of a circle (Figure 3.2 a). If the major and minor axes of an error ellipse have different lengths, the local direction finding accuracy is anisotropic with the uncertainty in one direction being larger than in the orthogonal direction. The amount of this error anisotropy can be quantified using the ratio of the length of the major and the minor axis. It should be noted that metrics like the length of minor axis of an error ellipse or length of major axis provide info on the accuracy(size) of the estimates while other metrics like the ratio of length of major axis to the length of minor axis and orientation of error ellipses provide info on the shape and directionality of estimation errors. Additionally, all these metrics like the orientation of error ellipses, the length of major and minor axis and the error anisotropy are caused by and solely dependent on the shape of the beampattern, i.e., beam gain as a function of direction. They do not depend on the arbitrary choice for

the orientation of the coordinate axes, i.e., azimuth and elevation. This is evident when the beampattern is rotated about an axis (s. Figure 3.4). In this case, the error ellipses rotate with the beampattern and retain their properties relative to the new orientation of the beampattern.

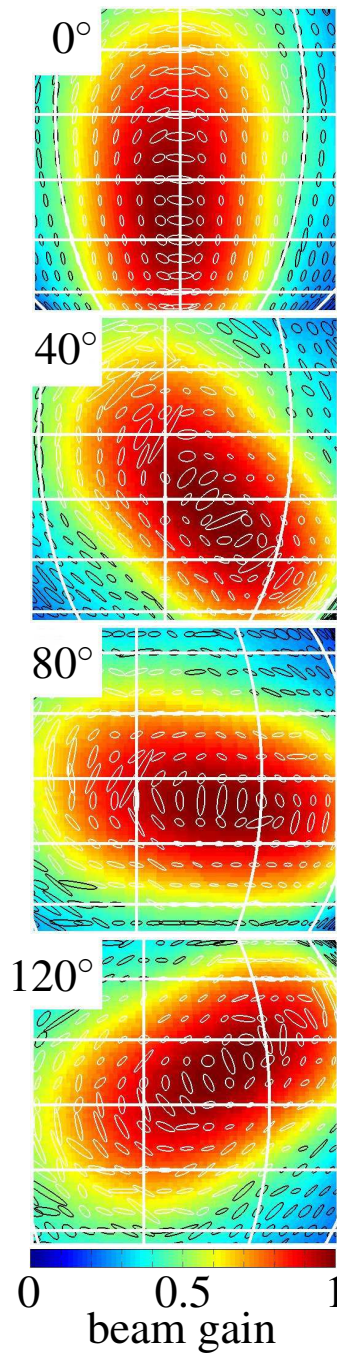


Figure 3.4: Effect of beam pattern rotation on the CRLB error ellipses. The error ellipses rotate with the beam pattern which shows that error ellipses are a property of the beam pattern and not of the coordinate system. The error ellipses were computed based on 10 different beam patterns (frequencies). The beam gain values shown are an average over the beam gains of all beam patterns used in the calculation. To enhance contrast, the lines of the error ellipses are plotted in white in areas of high beam gains (>0.5) and black for areas of low beam gains. The lines of the coordinate grid are spaced 30° in azimuth and 15° in elevation. The example beam pattern shown is an emission beam pattern of the Jamaican fruit bat.

In the current research work, distributions of the error ellipse properties were estimated for individual beampatterns as well as over the entire sample so as to obtain an overall characterization of a given beampattern's suitability for accurate target-direction finding. In order to provide sufficient flexibility for different distribution shapes as well as to model tail behaviors, the generalized extreme value distribution⁶¹ was used to fit the distributions for three error ellipse parameters (length of minor and major axis, error anisotropy).

A generalized extreme value distribution predicts the probability of rare or extreme events. It is the only possible limit distribution of properly normalized maxima of a sequence of independent and identically distributed random variables. I-e If N data sets, independent and identically distributed are generated from a distribution, and the maximum values from each dataset are collected together into a set A then the data in set A will have one of the three distributions for sufficiently large value of N. These three distributions are Gumbel, Fréchet and Weibull distribution depending upon the value of the shape parameter being equal to zero, being greater than zero and being less than zero respectively. In the case where the shape parameter is greater than zero, the fatness of the tail increases with the increase in the value of the shape parameter. Additionally, the other two cases, Gumbel and Weibull distributions have an exponential tail and an upper finite end point respectively. Overall the generalized extreme value distribution is characterized by three parameters, location, spread (scale), and shape parameter. All three parameters (location in the form of an average) were surveyed over the entire sample to obtain an overview of the shape of the distributions of the error ellipse properties in the individual beampatterns. In all these distribution analyses, only error ellipses for directions where the average beampattern gain (average over frequency) exceeded ≥ -30 dB were included. For comparisons between taxonomic groups, other variable gain thresholds were also used.

For the direction of the major axes, polar histograms were used and the scatter of the orientations was characterized by circular standard deviation, a measure that ranges between 0 and $\sqrt{2}$ with 0 signifying perfect alignment of all orientation vectors⁶³. The circular standard deviation was calculated as follows:

Let $\theta_1 \theta_2 \dots \theta_n$ be the n circular observations in radians then by applying polar to rectangular transformation, the resultant vector R is given by:

$$R = \sqrt{C^2 + S^2} \tag{3.31}$$

where

$$C = \sum_{i=1}^N \cos(\theta_i) \quad (3.32)$$

and

$$S = \sum_{i=1}^N \sin(\theta_i) \quad (3.33)$$

Thus the mean resultant length, \bar{R} is given by :

$$\bar{R} = \frac{R}{n} \quad (3.34)$$

According to Batschelet⁶², angular variance or circular variance is defined as

$$V = 2(1 - \bar{R}) \quad (3.35)$$

and correspondingly angular standard deviation or circular standard deviation is given by :

$$s = \sqrt{2(1 - \bar{R})} \quad (3.36)$$

where s is in radians.

3.3 Results

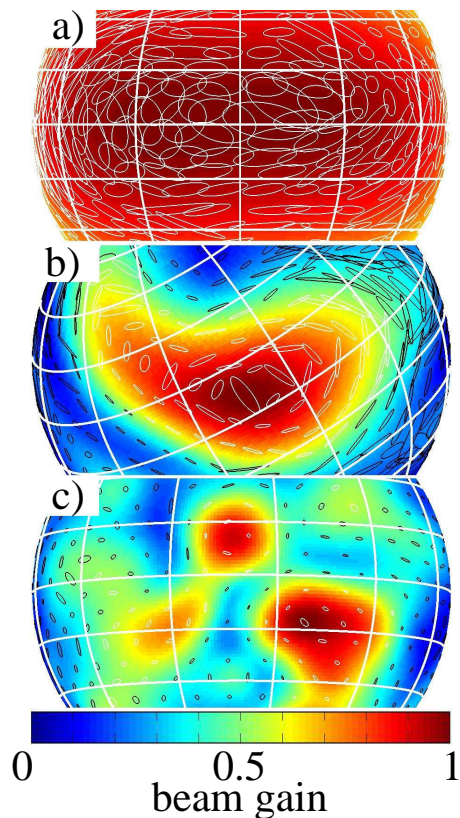


Figure 3.5: Interspecific diversity in the patterns of CRLB error ellipses. Beampatterns from three different bat species: a) Buffy flower bat (*Erophylla sezekorni*), b) Big-eared horseshoe bat (*Rhinolophus macrotis*), c) Stoliczka’s trident bat (*Aselliscus stoliczkanus*). The CLR estimates were computed for 10 frequencies. The beam gains depicted are averages over all beampatterns used in the CRLB calculations. To enhance contrast, the lines of the error ellipses are plotted in white in areas of high beam gains (>0.5) and black for areas of low beam gains. The lines of the coordinate grid are spaced 30° in azimuth and 15° in elevation.

A large diversity in the size, aspect ratio (i.e., error anisotropy), and orientation of the error ellipses was seen across the different beampattern samples analyzed: In some cases, the estimated error bounds were either uniformly large (Figure 3.5a) or uniformly small (Figure 3.5c) over the entire direction space. In other cases, the

size of the ellipses varied substantially across the beampattern's evaluated direction space (Figure 3.5b). Since the orientation of the error ellipses is determined by the gradients of the beampatterns, the orientation patterns of the ellipses over direction followed the slopes of the beampatterns' lobes with the minor axis pointing into the direction of the steepest slope (e.g., Figure 3.5b). Error ellipses at the center of the major lobe were found to be fat and big compared to the error ellipses on the edges of the major lobe. This is in accordance with the facts, established in the literature⁶⁶ that bats steer the direction of their sonar beam depending upon the requirements of their task. Thus in an ideal detection scenario where a strong signal to noise ratio is needed, a bat would tend to focus the portion of beampattern with maximum energy (center of the major lobe) onto the target and it would do that for each frequency so as to obtain a stronger echo that is well above the listening threshold. As the variations in the beam gain across direction and frequency are small at the center of the major lobe, therefore, error ellipses in such a region would be comparatively big. In the localization process where small estimation error is required, a bat would tend to focus the portion of beampattern with maximum slope onto the target. Such a region constitute various parts of the beampattern including the edges of the major lobe where the beam gain changes rapidly across direction and frequency, hence producing maximum slope and thus smaller error ellipses. (Figure 3.5)

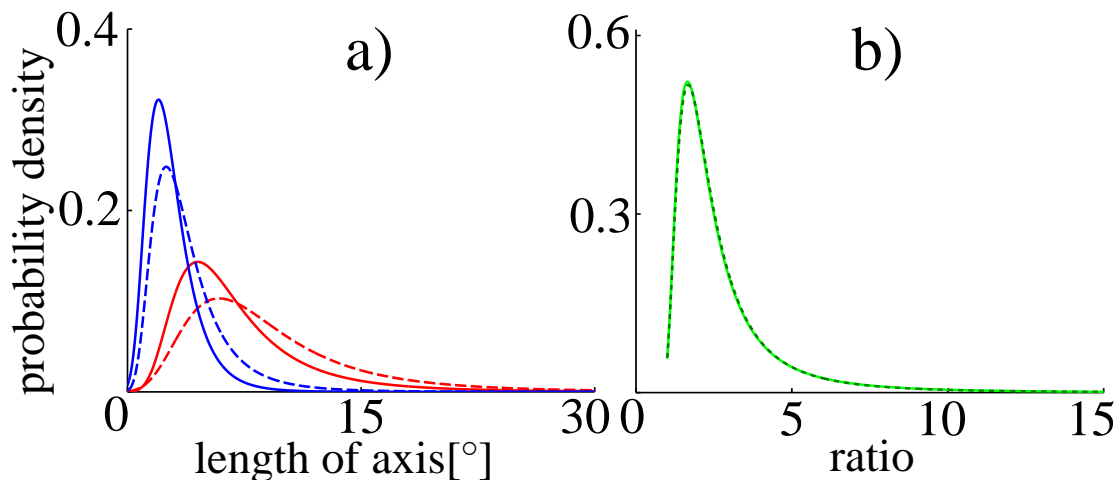


Figure 3.6: Distributions of various metrics across all samples in the analyzed beam pattern dataset. Blue lines and red lines represent the length of minor axis and major axis in panel a respectively while the green lines in panel b represent error anisotropy (ratio of major and minor axis length). The solid and dotted lines in both panels (a and b) represent the distributions calculated at lower beam gain threshold of -18 dB and -30 dB respectively. The distributions were fit using generalized extreme value distributions.

The overall distribution of major and minor axes length across all analyzed samples and all directions that were evaluated for each sample supported the notion that bat biosonar beampatterns supports fairly precise direction finding at the signal-to-noise ratio (60 dB) assumed here: The average length of the minor axis were 3.9° and 2.81° at lower beam gain thresholds of -30 dB and -18 dB respectively and 90% of minor axis lengths in each case were shorter than 7.1° and 4.9° respectively (Figure 3.6a). The average length of the major axis were 9.3° and 7.2° for lower beam gain threshold of -30 dB and -18 dB respectively. The error ellipses in the analyzed data were for the most part anisotropic, with the ratio between major and minor axis having an average value of about three in each case (Figure 3.6b). The distributions for minor axis, major axis lengths, and the error anisotropy over the entire dataset were found to have a systematic but weak dependency on the frequency band that was used to compute the CRLB estimates. Such a dependence in the case of lower beam gain threshold of -30 dB is shown in Figure 3.7. The peak of the probability density function in each case in Figure 3.7 shifted towards smaller axes lengths as the frequency band was changed from low to medium and on to high frequencies. For the

length of the minor axis, for examples, the shift in the peak of the probability density function was less than one degree (Figure 3.7a). Similar behavior was observed in the case of lower beam gain threshold of -18 dB.

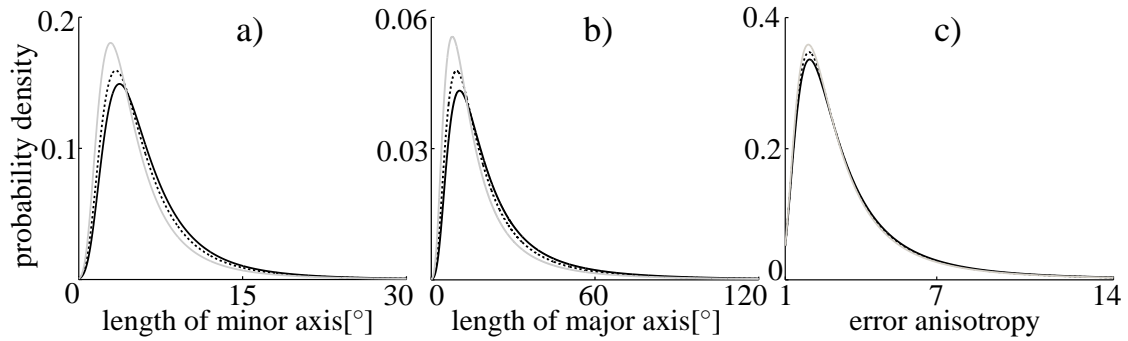


Figure 3.7: Frequency dependence of the probability density functions for a) length of minor axis, b) length of major axis, c) error anisotropy. The lines in each graph represent the three different subbands studied: solid black line: low-frequency band (frequencies 1 to 5), dashed line: medium-frequency band (frequencies 3 to 7), gray line: high-frequency band (frequencies 5 to 10).

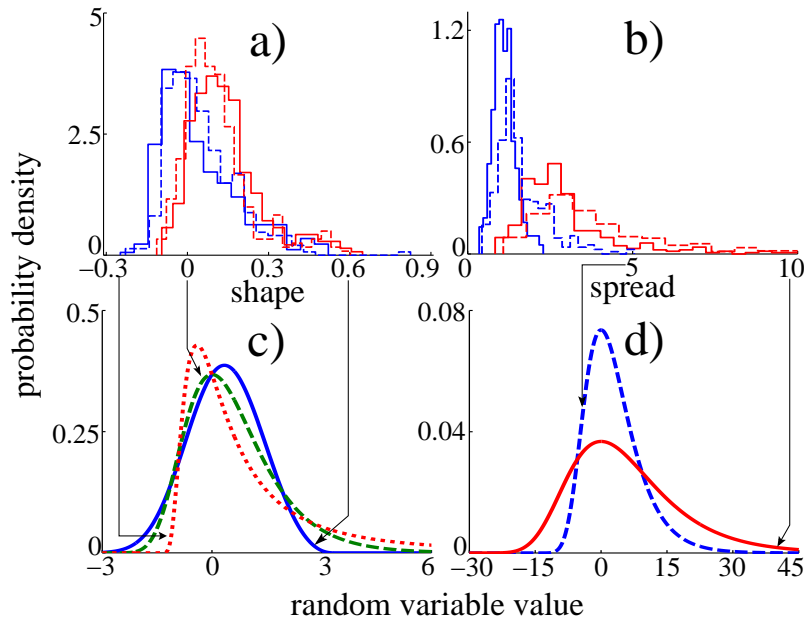


Figure 3.8: Distribution (histograms) of the shape (a) and spread (b) parameters of generalized extreme value distributions that were used for modelling minor and major axes lengths in individual samples of bats. Blue and red lines in graphs a) and b) represent the histograms for the minor and major axis error respectively while solid and dashed lines represent the histograms at lower beam gain thresholds of -18 dB and -30 dB respectively. b) Example distributions for different values of the shape parameter. d) Example distributions for different values of the spread parameter.

For individual samples of bats within the dataset, the distributions of minor axis length, major axis length and their ratio were found to be well described by the generalized extreme value distribution model. The goodness of fit (RMS error) for this model at lower beam gain threshold of -18 dB and -30 dB ranged between values of 0.00007 and 0.1 with 99 % of values being less than 0.074. Hence even for the largest observed RMS errors, no systematic differences between the histogram estimates and the respective model distribution were evident. For lower beam gain threshold of -30 dB, the shape parameter assumed values greater than 0 for 68% of the analyzed beampatterns with an average value of 0.066 (Figure 3.8a) making lengths of major and minor axes follow mostly a Fréchet distribution, i.e., a special case of the generalized extreme value distribution that is characterized by a positive skew. As a consequence, the distribution of the major and minor axes had a heavy

right-hand tail which means that the errors associated with these analyzed beam-patterns tended to have frequent outliers with large major and minor axes. Apart from that, the distributions for the shape parameter did not differ much between the data obtained for minor and major axis length (Figure 3.8a). This was different for the spread parameter (Figure 3.8b), where the average value of the parameter was 4.1 for the major axis data and 1.5 for the minor axis data. Thus, the major axes were not only longer than the minor axes, their length was also more variable with the variability scaling approximately with the mean values, i.e., at 9.3° the average length of the major axis was about 2.4 times that of the minor axis (3.9°) and the average shape parameter was 2.5 times larger for the distributions of the major axes than for the distributions of the minor axes. Analysis at lower beam gain threshold of -18 dB yielded similar results as evident by solid blue and red lines in figure 3.8.

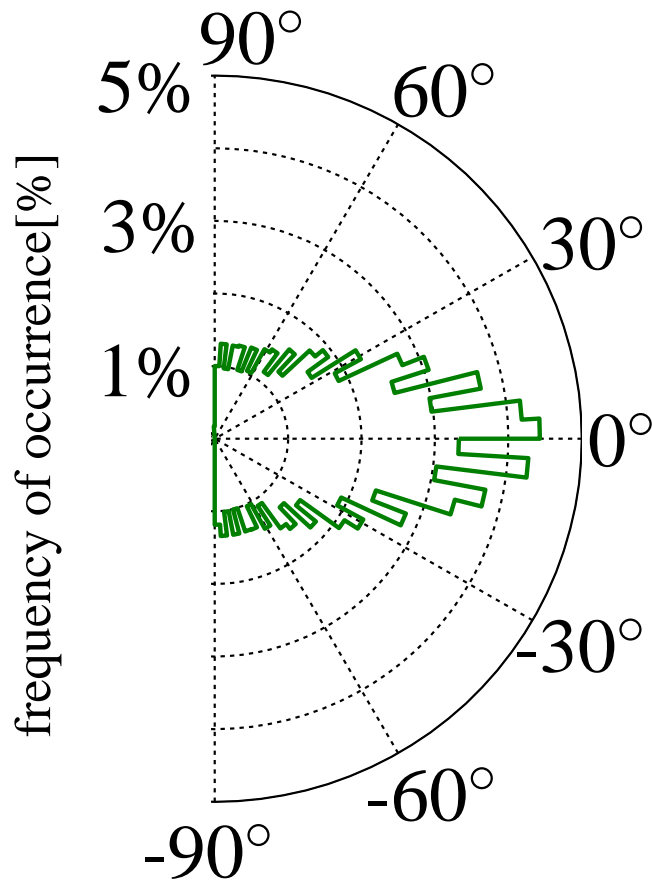


Figure 3.9: Distribution of the directions of the major axes of the error ellipses over the entire sample (emission and reception beampatterns). The circular data has been distributed into 100 bins and 0° refers to an axis that is aligned with the horizontal.

The directions of largest estimation error bounds, i.e., the major axes, over the entire dataset were found to have a preferred orientation that was roughly aligned with azimuth (Figure 3.9), i.e., the error ellipses were – on average – oriented to provide a better accuracy in elevation than in azimuth.

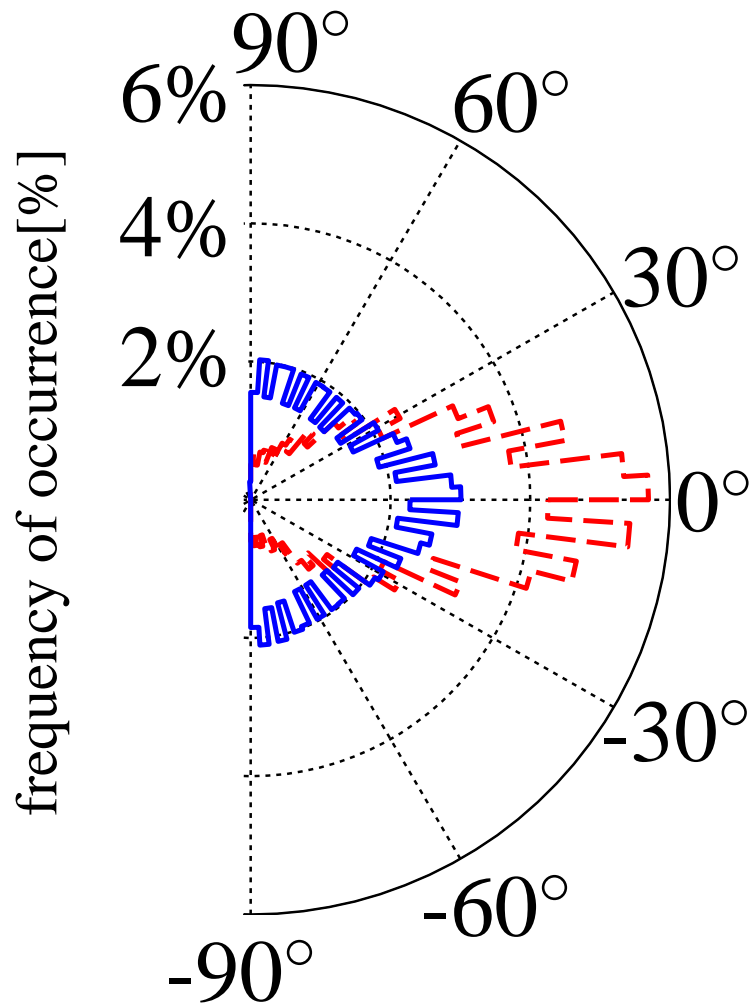


Figure 3.10: Distribution of the directions of the major axes of the error ellipses for emission (solid lines) and reception (dashed lines) beam patterns. The circular data has been distributed into 100 bins in each case and 0° refers to an axis that is aligned with the horizontal.

In terms of functional differences between the beam patterns, it was found that beam patterns could be characterized into two groups (emission beam patterns and reception beam patterns) based upon the scatter in the orientation angle of the error ellipses in their error ellipses plot. The orientation of the error ellipses scattered much less for the reception beam patterns (dotted red line, Figure 3.10) than for the emission

beam patterns (blue solid line, Figure 3.10) with the circular standard deviation being 0.82 radians for the emission and 0.58 radians for the reception (Figure 3.10). The majority of the error ellipses in the case of the ear (dotted red line, Figure 3.10) were oriented along the azimuth direction thereby emphasizing the role of monaural cues in estimation along the elevation direction. For the case of noseleaf (Figure 3.10), the number of ellipses directed along the horizontal were slightly more than the number of error ellipses directed in all other directions. This is because even though noseleaf distributes energy in all the directions in frontal hemisphere, it focuses energy slightly more along the elevation direction thus improving signal to noise ratio for the echo, in the direction in which ears are most sensitive (the elevation direction).

Aside from the differences in the preferred orientation angle of the error ellipses, differences of the order less than 2° were observed between emission and reception beam patterns available in the dataset in terms of their minimum estimation error. Reception beam patterns were also found to be slightly more anisotropic than emission beam patterns with percent difference between their average values being 19%. As reception and emission beam patterns were not available for the purpose of analysis in the case of all nine families of bats, therefore, to remove any phylogenetic bias from the results, emission and reception beam patterns were also compared for only those families of bats in which both types of beam patterns were available. The results for two such families of bats (Rhinolophidae and Hipposideridae) are shown in the Figure 3.11.

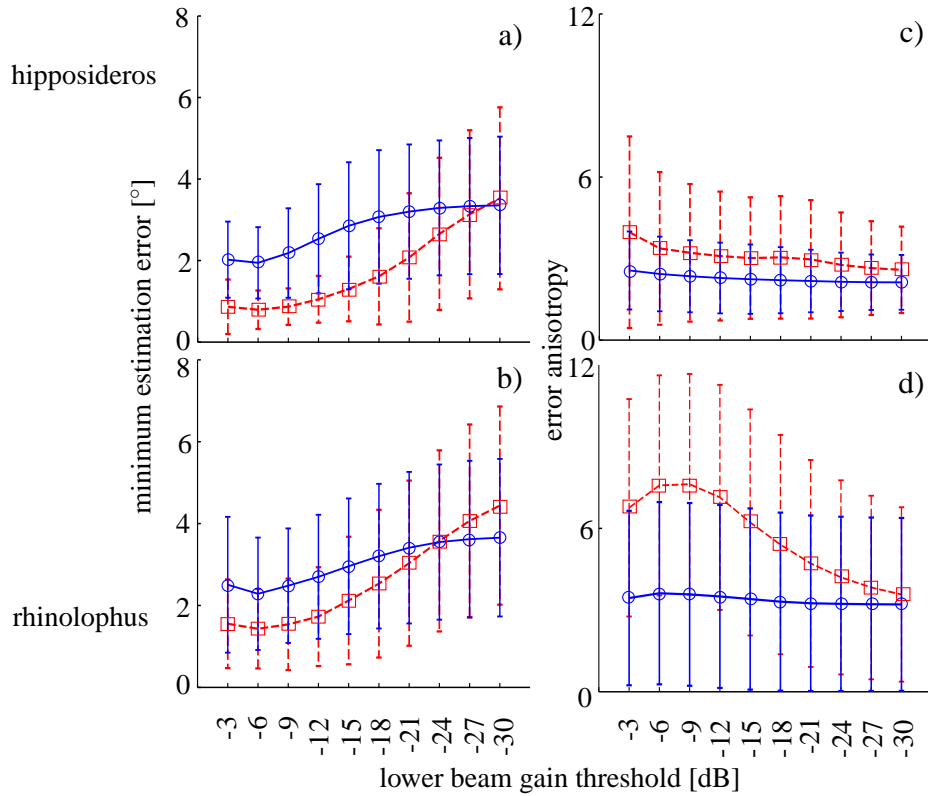


Figure 3.11: Minimum estimation error and error anisotropy for emission and reception beampatterns in rhinolophids and hipposiderids. Panel a) and panel b) represent the mean and standard deviation values for the Minimum estimation error (length of minor axis of the error ellipse) as a function of lower beam gain threshold for emission (\circ) and reception (\square) beampatterns in hipposiderids (a) and rhinolophids (b). Similarly panel c) and panel d) represent the mean and standard deviation values for the error anisotropy (ratio of major and minor axis lengths) as a function of lower beam gain threshold for emission (\circ) and reception (\square) beampatterns in hipposiderids (c) and rhinolophids (d). The markers represent the mean values while the bars represent the standard deviation.

As evident from Figure 3.11, the accuracy afforded by the reception beampatterns is slightly higher than that of emission beampatterns in particular at higher beam gain thresholds. However, these differences are small i-e about 1.2° for Hipposideros

and 0.95° for *Rhinolophus* at -3dB. Similarly, the error ellipses for reception beam-patterns are found to be more anisotropic than those for emission, in particular for rhinolophids.

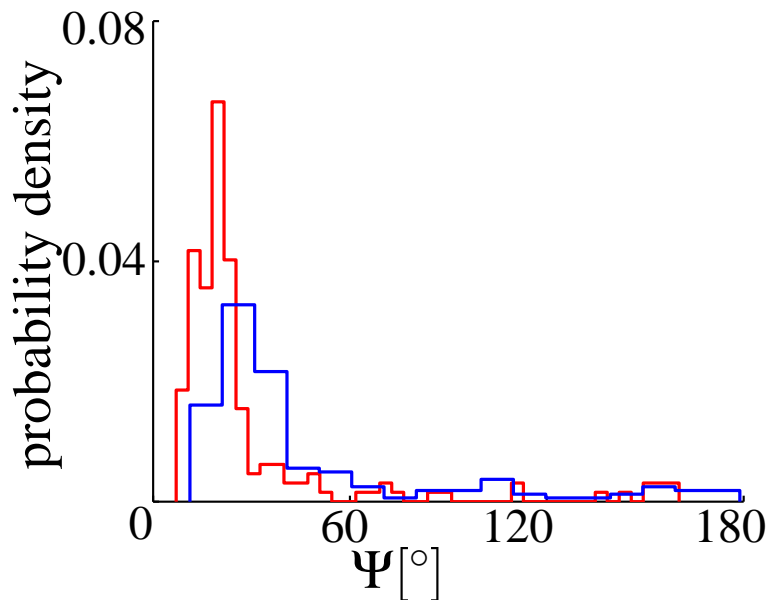


Figure 3.12: Histogram for the values of angle, Ψ , between the points of maximum sensitivity and minimum estimation error. Solid red and blue lines represent the histogram for the ear and noseleaf respectively.

For both emission and reception beampatterns, the regions with the best estimation performance were found to fall in the vicinity of the respective beampattern's amplitude maximum. For emission, the angular difference between the direction of the beam gain maximum and the direction of the best direction-finding performance (smallest minor axis) was less than 104° for 90% of all cases. For reception, the 90th percentile of the angular differences was 49° .

Classification of beampatterns could also be achieved based on the structure of the echolocation call associated with the beampatterns. Using such a basis, bats in the current dataset were classified into two categories, low duty cycle bats⁶⁴ and high duty cycle bats⁶⁵. Low duty cycle bats separate the emitted pulses and the returning echo in the time domain while high duty cycle bats separate them in the frequency domain. The current study investigated various species of bats in the family Hipposideridae and Rhinolophidae which constitute CFFM bats (High duty cycle bats)

as well as species from the family Vespertilionidae and Phyllostomidae that constitute FM Bats (Low duty cycle bats). For the purpose of analysis, values of metrics like minimum estimation error and maximum estimation error were calculated for each sample of species in the two groups at two lower beam gain thresholds (-18dB and -30 dB). The values of the metrics were then modelled using generalized extreme value distributions, the shape parameter for which at two lower beam gain thresholds of -30 dB and -18 dB are shown in Figure 3.13.

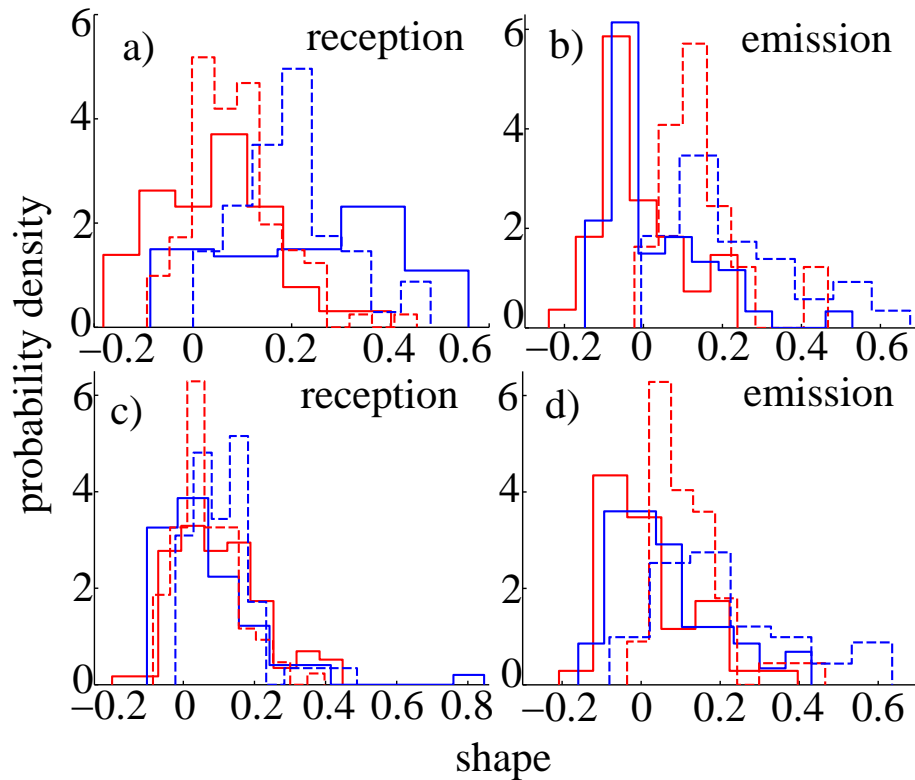


Figure 3.13: Distribution (histograms) of the shape parameters of generalized extreme value distributions that modelled the minor and major axes lengths in CFFM and FM bats. Red and blue lines in the graphs represent the histograms for the FM and CFFM bats respectively while solid and dashed lines represent the histograms for length of minor and major axis. Panel a) and panel c) represent the distribution of shape parameter for ear samples with a lower beam gain threshold of -18 dB and -30 dB respectively while panel b) and d) represent the distribution of shape parameter for noseleaf samples at lower beam gain threshold of -18 dB and -30 dB respectively.

As can be seen from the Figure 3.13, the two types of beampattern are vividly different only in the case of reception beampatterns and that too at higher values of lower beam gain thresholds (i-e -18 dB). This can be observed from the differences in the histograms of the shape parameter for CFFM and FM bats in Figure 3.13 a). In all other cases where either the lower beam gain threshold is low or the beampatterns belong to noseleaf, the differences between the shape parameter for the CFFM bats and FM bats are minute compared to the inter family differences in the values of shape parameters as evident from the Figure 3.13 b), Figure 3.13 c) and Figure 3.13 d) and Figure 3.14.

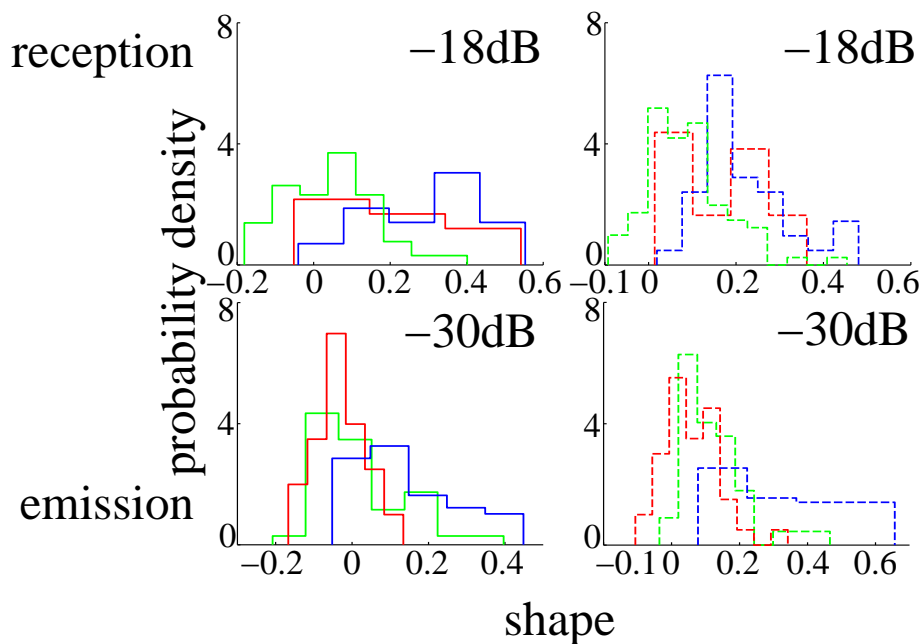


Figure 3.14: Inter family and inter duty cycle differences in the distribution of shape parameter for the reception and emission beampatterns at lower beam gain threshold of -18 dB and -30 dB respectively. Solid and dotted lines represent distribution of shape parameters for the case of length of minor and major axis respectively. Red and blue lines represents the plots for family Hipposideridae (CFFM) and Rhinolophidae (CFFM) respectively while green lines represent the plots for the families, Vespertilionidae (FM) and Phyllostomidae (FM) in reception and emission categories respectively. Inter duty cycle differences in terms of shape parameter for the length of minor and major axis are stronger in reception beampatterns at -18 dB threshold than inter family differences in the same respect and vice versa for the case of emission beampatterns at -30 dB threshold.

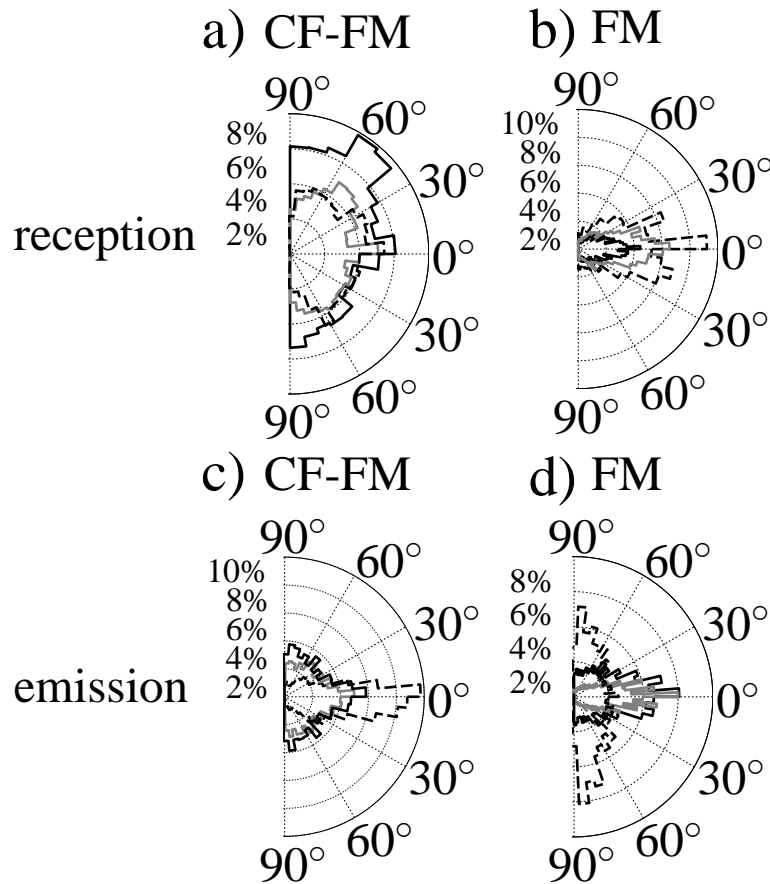


Figure 3.15: Circular distribution of the orientation angle of error ellipses in the case of CFFM and FM bats. Panel a) and panel b) represent the orientation angle of error ellipses for the reception beampatterns of CFFM bats and FM bats respectively while panel c) and d) represent the orientation angle of error ellipses for emission beampattern of CFFM bats and FM bats respectively.

The two groups of beampatterns are also different in terms of orientation angle of the error ellipses. Figure 3.15 a) and Figure 3.15 b) represents the orientation angle of error ellipses in the case of reception beampatterns of CFFM bats and FM bats with the circular standard deviation of the former and the latter being given in table 3.1. Clearly most of the error ellipse in the case of reception beampatterns in FM bats are oriented in the same direction. This is in sharp contrast to the case of reception beampatterns in CFFM bats where error ellipses are directed in all

directions. This is because inter frequency variations in the position of maximum sensitivity in reception beampatterns are much more in the case of FM bats than in CFFM (Figure 3.16 a,b), thereby creating comparatively more notches and peaks and hence producing stronger effects due to monaural cues that help in direction finding along the elevation direction. CFFM bats compensate for this by changing the shape and the orientation of the ear, thereby changing the geometry of the beampattern and hence obtaining the required effects (i-e steering of a beam). In the case of noseleaf, the differences between the circular histogram of the two groups (CFFM bats and FM bats) are much smaller and so as the differences in between their inter frequency variations in the position of maximum sensitivity (Figure 3.16 c,d).

Baffle Type	Type of Duty cycle	Family	Circular standard deviation (radians)
Ear	high	Hipposideridae	0.87
		Rhinolophidae	0.83
		Molossidae	0.81
Ear	low	Vespertilionidae	0.67
		Pteropodidae	0.60
		Emballonuridae	0.63
Nose	high	Hipposideridae	0.84
		Rhinolophidae	0.81
		Molossidae	0.58
Nose	low	Megadermatidae	0.70
		Nycteridae	0.55
		Phyllostomidae	0.97

Table 3.1: Circular standard deviation

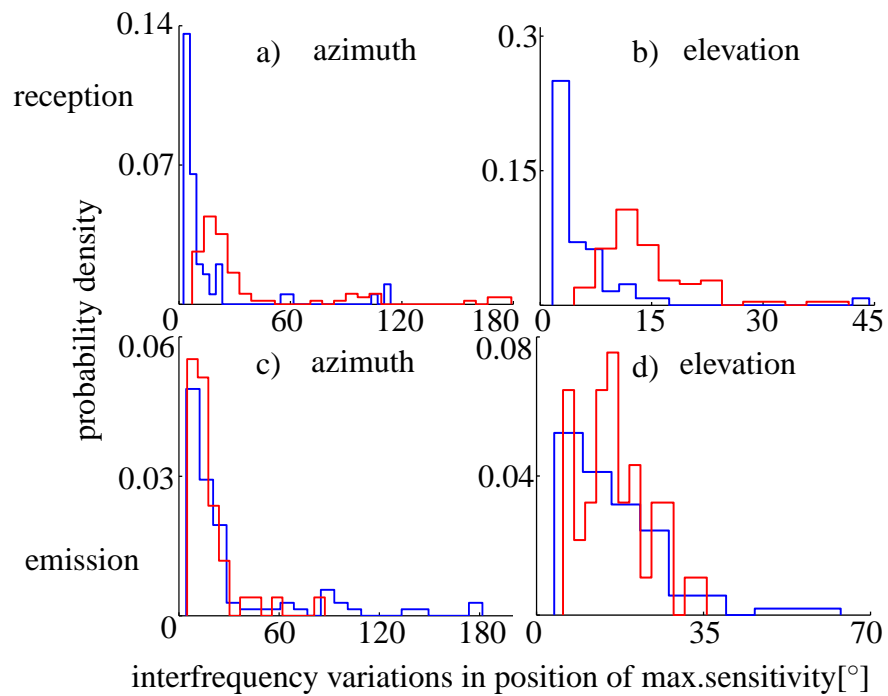


Figure 3.16: Interequency variations in the position of maximum sensitivity in reception beampatterns are much bigger in FM bats than in CFFM bats. Red and blue lines represent the histograms for FM and CFFM bats respectively. Panel a),b) and panel c),d) represent the plots for reception and emission beampatterns respectively while panel a),c) and b),d) represent interfrequency variations in the position of maximum sensitivity along azimuth and elevation direction respectively.

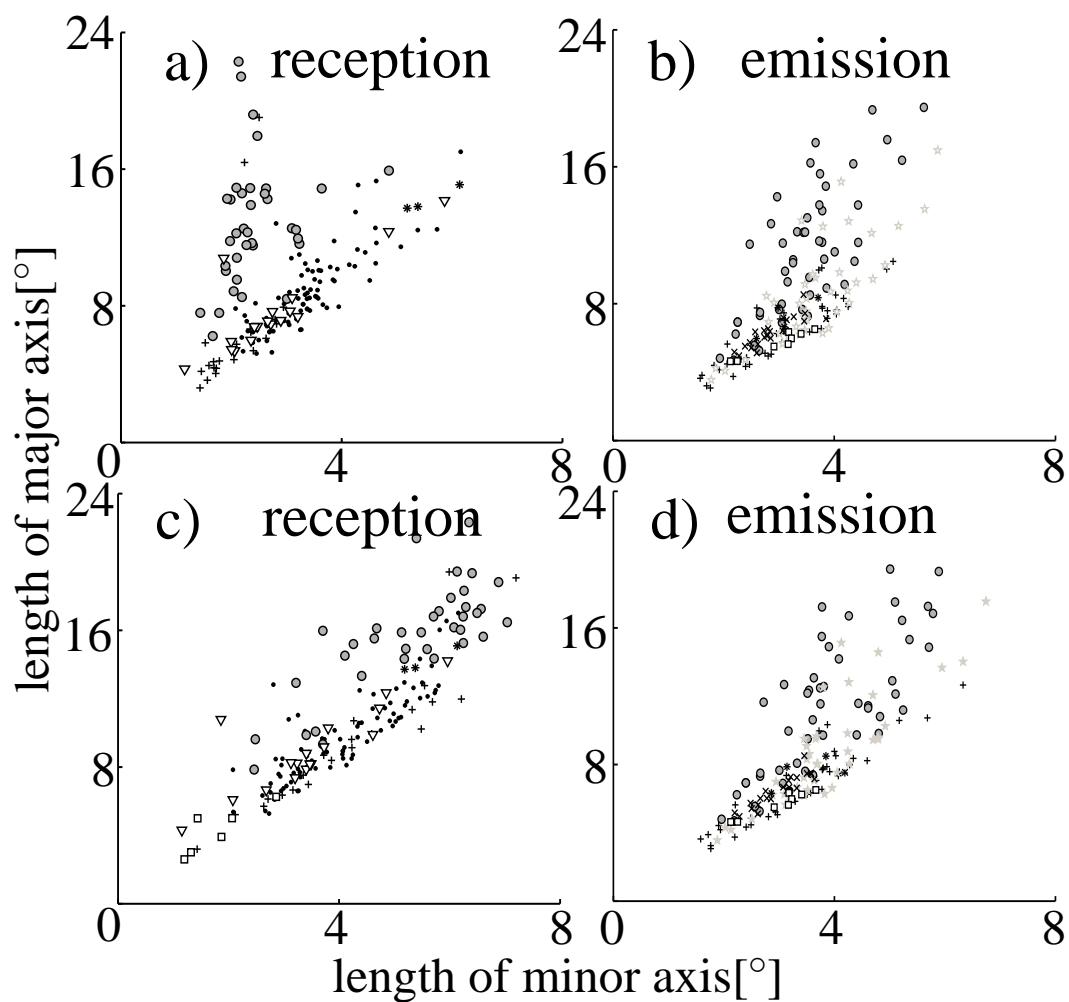


Figure 3.17: Distribution of individual samples (marked by family) with respect to average values of error ellipse size. Panel a),c) and b),d) represent the distribution of average values of major and minor axis length for ear and noseleaf samples respectively. Values in panel a),b) and c),d) are calculated at lower beam gain threshold of -18dB and -30dB respectively. The families are with the following markers: \circ Rhinolophidae, $+$ Hipposideridae, \bullet Vespertilionidae, \times Nycteridae, ∇ Pteropodidae, \star Phyllostomidae, \square Megadermatidae, $*$ Molossidae.

Finally, the average values of minimum estimation error and maximum estimation error at a lower beam gain threshold of -18 dB and -30 dB for individual samples of

bats are plotted in Figure 3.17. The values of the metrics for eight different families of bats tend to form clusters with the overlap between them being much less at higher beam gain threshold (-18dB) than at lower beam gain threshold. The overlap between the cluster is also much less in the case of ear than in the case of noseleaf. Hipposideridae (represented by +) for example forms a cluster at the lower left corner of the Figure 3.17 a) indicating the best estimation performance among all families of bats in terms of minimum as well as maximum estimation error. Vespertilionidae and Pteropodidae, in the same figure, represented by \bullet and ∇ respectively shows average performance while Rhinolophidae represented by \bigcirc has the biggest values of maximum estimation error. Rhinolophidae also has, usually the highest values of maximum estimation error at any beam gain thresholds as well as for any type of baffle shape whether ear or noseleaf. One apparent reason for this is the disregard of any effects on the estimation performance of Rhinolophidae due to the dynamic motion of its noseleaf and pinna. Such effects have been considered in the next chapter.

3.4 Discussion

The work presented here is the first study to apply an immediate and quantitative measure of estimation accuracy to a large and taxonomically diverse set of bat biosonar beampattern data. Hence, the present results provide the first opportunity to make predictions of the direction-finding performance across many bat species and to investigate the diversity in bat biosonar beampatterns as it relates to the accuracy of direction finding.

Describing the estimation error in terms of orthogonal minor and major axes do not require any knowledge regarding the frame of reference that the bat uses. This is a desirable feature of the current approach, because information about the bat's frame of reference is not easily deduced from the isolated noseleaf and pinna samples that were used in this study. Furthermore, it is not clear whether the bats use a constant frame of reference at the beampattern level since the beampattern orientation in the external world could vary substantially due to rotations of the head or rotations of the ears relative to the head. While the results presented here on the lengths of minor and major axes and the error anisotropy are not impacted by this complication, the findings about the ellipse orientations should be interpreted with caution since it cannot be ascertained that errors in the relative alignment of the samples does not affect the results.

The estimates for the average estimation error depicted in Figure 3.6 are well aligned with the results of behavioral experiments for angular resolution. For example, the angular resolution for elevation in the big brown bat (*Eptesicus fuscus*) was determined to be 3° ⁶⁸, which is close to the 3.9° and 2.81° average lower bounds on the error found here. Similarly, the results of behavioral experiments have estimated the angular resolution for azimuth in the same species to be around 1.5° ³⁸. While still fairly close to the average values found here, angular resolution in azimuth likely makes use of binaural cues that were not included in the analysis conducted here.

The values presented here depend on the assumed signal-to-noise ratio. While the signal-to-noise of 60 dB that has been used here is certainly favorable, it is not unrealistic and could be achieved, for example, with 100 dB SPL emission level⁶⁹, a total loss of -40 dB (due to target strength and propagation), and a 0 dB SPL hearing threshold⁷⁰. For higher emission levels⁷³, larger losses or higher hearing thresholds would be possible. Since the boundary values scale linearly with the signal-to-noise ratio (σ^2 in Eq. 3.29) it is straightforward to scale the results presented here to match different assumptions about the signal-to-noise ratio.

Irrespective of signal-to-noise ratio, the positive skew seen in the distributions for the lengths of the major and minor axes of the error ellipses indicates that the bat biosonar beampatterns contain regions of comparatively low estimation accuracy. If the positive skew of the distributions is a property that is present *in vivo*, it could be the cause for behavioral adaptations, i.e., the use of prior knowledge by the bats to orient their beampattern to avoid the occurrence of targets in regions of low accuracy. This could fit behavioral observations which have been interpreted as the bats using the slopes of their beampatterns for direction finding⁶⁶.

The consistent effects of the frequency band on the overall distributions characterizing the size of the error ellipses is consistent with beampatterns created by higher frequencies having narrower main and side lobes and – as a result – steeper flanks. The small size of the observed effects (less than 1°) can be explained by the comparatively small bandwidth used by bats. The wavelengths found within these frequency bands differ only by factors that are typically well below ten. While bat biosonar beampatterns created at higher frequencies tend to be narrower and have additional sidelobes, they are still qualitatively similar to those at lower frequencies and this similarity is reflected in the small effects obtained here.

In the current study, the diversity in the biosonar beampattern geometries, e.g., in terms of the number, shape, and relative orientation of the lobes, was found to be reflected in a likewise diverse pattern of error ellipses. This is not unexpected since

the error ellipses of the CRLB are directly tied to the geometry of the beampattern through the partial derivatives of the beam gain function. However, it is noteworthy that within this diversity, some common trends were found. The most notable of these trends is in the preferred orientation of the error ellipses. Since the major axes of the error ellipses were scattered in the horizontal direction, the largest accuracy that can be achieved is in the vertical, i.e., in elevation. This finding matches the pivotal role of spectral cues for finding the elevation of a target, whereas binaural cues dominate determination of azimuth in mammals such as humans⁷⁴ and cats⁷⁵ as well as in birds⁷⁶. The only notable exception to this trend that was found in the current data set are the emission beampatterns of the phyllostomids where the major axes of error ellipses had a preferred direction along the vertical.

The current study has evaluated emission and reception beampatterns separately. This is a complete characterization only in the case of reception beampatterns employed in a “passive sonar” mode, i.e., for listening to signals from foreign sources. For active sonar sensing, emission and reception beampatterns are used in series and the CRLB will hence depend on the shape of both beampatterns. In order to estimate the CRLB for the entire sonar system (emission and reception), the proper, i.e., *in-vivo*, alignment of the emission and reception beampattern would have to be known. This is not the case for the current data set since it was derived from numerical beampattern estimates that were made for isolated noseleaf and pinna samples. Nevertheless, the CRLB values computed for the emission beampattern alone can be used as an indication for how well the emission beampatterns are suited to support direction finding accuracy and how they compare to reception beampatterns.

Differences between emission and reception beampatterns have already been reported in previous studies that used other characterization approaches not directly related to estimation performance^{32;33}. The current results show that the categorical differences between emission and reception beampatterns include effects that could be relevant to the accuracy of direction finding. The most conspicuous difference between emission and reception beampatterns found in the present study was that the distribution of major axes of the error ellipses revealed much more scatter for emission than for reception. It is not obvious how to interpret this difference. Excluding the phyllostomid emission beampatterns with their – in general – vertically oriented error ellipses (Fig. 3.15c) from this analysis reduces the width of the distribution for major-axis orientations for emission slightly. It does not, however, substantially reduce the difference between the distributions for emission and reception beampatterns. Hence, the distinctive properties of the phyllostomid emission beampatterns cannot explain this difference. If it is true that the spectral cues generated by the

beam patterns are primarily for determining elevation, then the narrower distribution of the major-axis directions for reception could be seen as an indication that reception beam patterns play a greater functional role and are hence subject to stronger evolutionary pressures on the alignment of the error ellipses. However, it could also be that the individual pairs of emission and reception beam patterns complement each other to produce the desired result – which may or may not be entirely focused on elevation estimation. Future work is needed to study the alignments between emission and reception beam patterns and determine if any relationships exist between them.

Chapter 4

Local shape features and dynamic motion

4.1 Introduction

Biosonar has enabled bats to thrive in extremely different environments. This has been possible primarily due to the ability of the bats to come up with solutions to their problems under different set of constraints. Such solutions are reflected in morphological variation seen across large ensemble of baffle shapes (Figure 2.2,2.3). In-depth analysis of such variations could shed light on different informational needs and beamforming strategies required to meet them⁷⁷. Current array signal processing techniques are useful in achieving adaptive beamforming operations, however, baffle based beamforming seen in nature surpasses them in aspects of complexity and computational cost by achieving major signal processing in physical domain thereby making the following stages simpler. Example of such baffle based beamforming in bats include the effect on directionality from local shape features like ripples^{78;79}, tragus^{39;80;45}, the effect of ripple and tragus together⁷⁸, lancet⁸¹, sella^{82;83} etc. To get a true hold of such contributions made by local shape features to the bat biosonar performance, static local shape features like ridges, incision, antitragus and dynamic local shape features like lancet that produces nonrigid deformations will be discussed in the current work and their acoustic need and relevance will be assessed.

4.2 Static local shape features in pinna

A pinna in a bat is an interface between the outside world and the bat's subsequent neural signal processing stages. Such an interface encodes useful information from the animal's surrounding through the use of scattering of ultrasonic waves in a direction and frequency dependent manner. Major components of pinna responsible for achieving this ultrasonic diffraction are shape features like ripples, ridges, incision, tragus, antitragus etc whose geometry, size and layout are tuned to specific tasks that bats are supposed to perform. Analysis of such tasks has been carried out in several studies^{84;53}. From one such study⁸⁴, an example of an actual pinna of a Horseshoe bat and its prototype are shown in Figure 4.1.

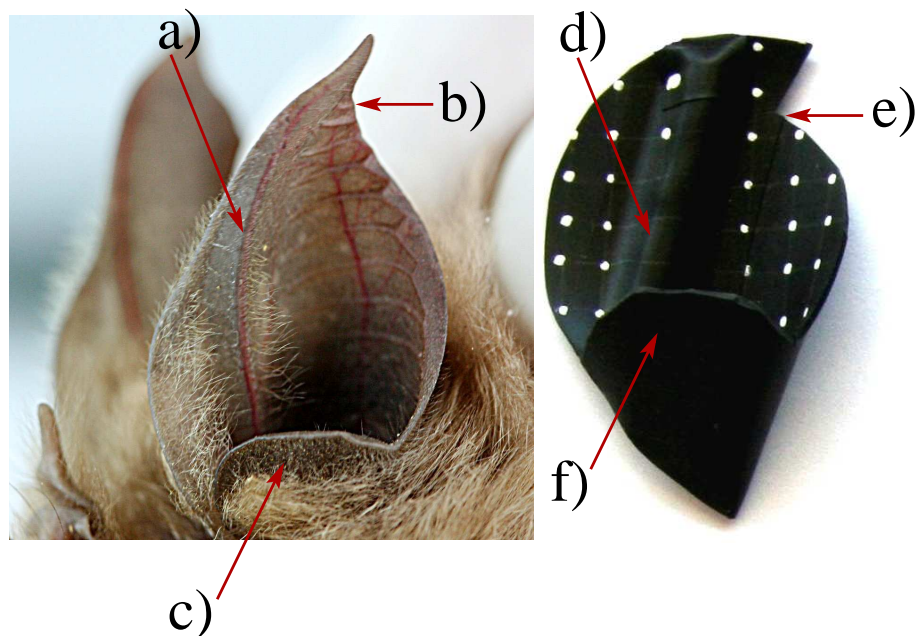


Figure 4.1: Local shape features in an actual horseshoe pinna and in its prototype. a), b) and c) represent ridge, incision and antitragus respectively in an actual horse shoe pinna while d) e) and f) represent ridge, incision and antitragus in its prototype. Reproduced with permission from the author⁸⁵.

The pinna in Figure 4.1 consist of three important local shape features, vertical ridge, incision and antitragus which can be added either separately and together to an obliquely truncated cone. The simple obliquely truncated cone represents the

simplified mammalian pinna⁸⁶ as well as an average pinna shape in the case of 100 different pinna shapes⁷⁷. The eight different prototypes produced as a result of combining three local shape features are shown in Figure 4.2

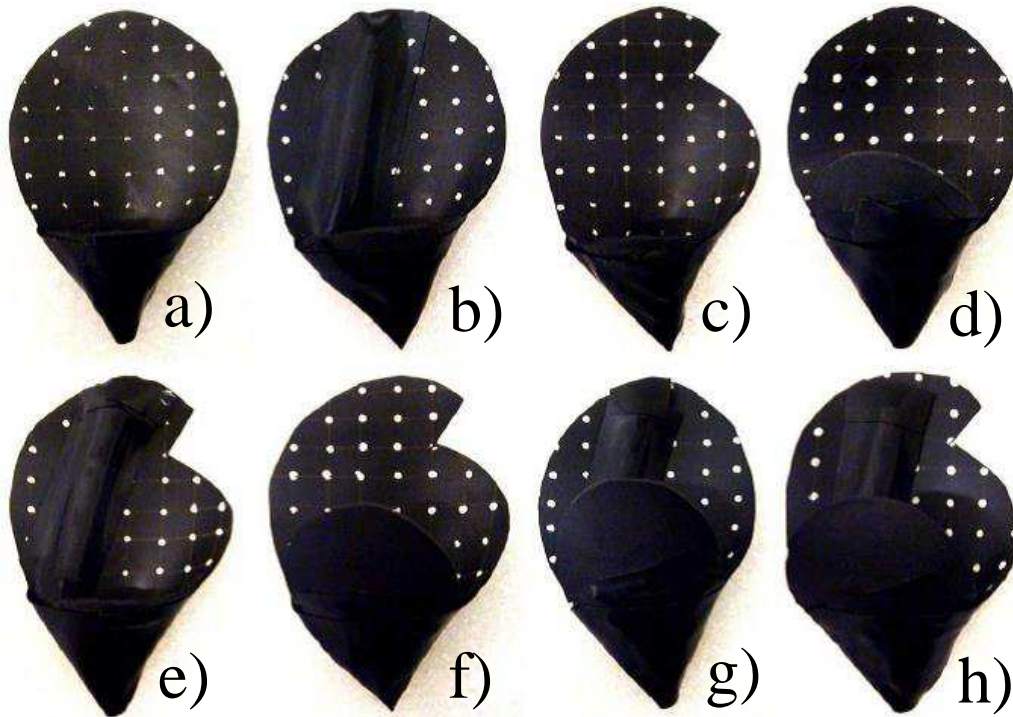


Figure 4.2: Obliquely truncated cone augmented with three local shape features in a stepwise manner, thereby producing eight different prototypes. a) no feature b) ridge c) incision d) antitragus e) ridge+incision f) incision+antitragus g) ridge+antitragus h) ridge+incision+antitragus; Reproduced with permission from the author⁸⁵.

Previous work⁸⁴ on 8 different prototypes mentioned in Figure 4.2 reported small changes in beampattern as each local shape feature was added independently however in cases where two or three local shapes features were added simultaneously, interaction between the local shape features and the bending of pinna tip produced significant changes in the beampatterns in the form of sidelobes. The current work takes this investigation one step forward by describing the impact of these changes on the biosonar performance of bats. The average beampatterns and the respective error ellipses for eight different prototypes of the pinna are shown in the Figure 4.3.

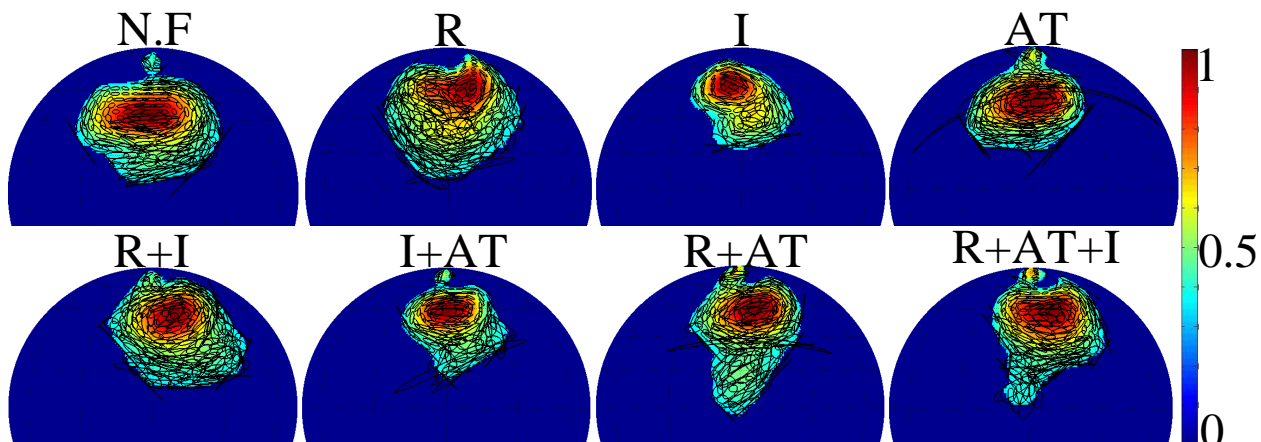


Figure 4.3: Beampatterns for the truncated cone to which combination of local shape features are added in a stepwise manner. The description of labels for the eight circular histograms are : N.F(No feature), R(Ridge), I(Incision), AT(Antitragus), R+I(Ridge+Incision), I+AT(Incision+antitragus), R+AT(Ridge+antitragus), R+I+AT(Ridge+Incision+Antitragus).

From the study of the average directivity for eight different prototypes at a lower beam gain threshold of -9dB (Figure 4.3), it was found that addition of ridge to the pinna produces asymmetry in the directivity pattern and removes any sidelobes present in the directivity of the original pinna. Addition of incision to the original pinna produces a smaller major lobe and a stronger side lobe. It also reduces the size of the error ellipses throughout the directivity pattern of the pinna. Addition of antitragus to the original pinna, rotates the major lobe by a few degrees, increases the size of error ellipses by a small amount and produces a sidelobe. Addition of incision to the already added ridge restores the symmetry in the directivity pattern and increases the size of the error ellipses besides producing a weak side lobe. Incision, on the other hand, when added to the antitragus reduces the size of the major lobe, decreases the strength of side lobe and makes the error ellipses slightly smaller. Addition of antitragus to the ridge restores a relative symmetry to the directivity pattern of the ridge besides producing sidelobes and making the error ellipses smaller. Finally adding all the features together generates a major lobe with a shape that matches more closely to a circle than to a rectangle which matches the major lobe of the pinna carrying no feature.

In terms of average value of the product of estimation errors (minimum and maximum), the ridge and antitragus were found to have the worst estimation performance

among the three individual local shape features (Table no. A.1). However, the two local shape features together provided the best or close to the best performance possible in combinations. This transition from the worst to the best estimation performance was not the only surprise. Incision which provided the best estimation performance among all local shape features and their combinations when present alone, together with ridge provided the worst estimation performance out of all the four combinations. The percent difference in the average values of the product of estimation errors between the incision and any other single local shape feature or their combinations ranged between 23.6 % to 45.6 %. The results were obtained at a lower beam gain threshold of -9 dB. Similar results were obtained at lower beam gain threshold of -18 dB. The detailed results are presented in the appendix (Table no. A.1).

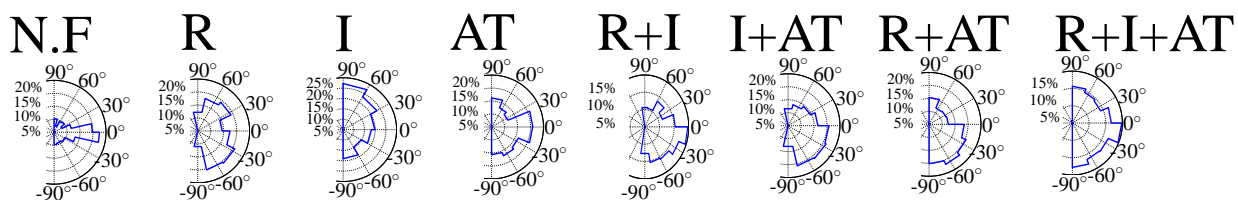


Figure 4.4: Angular histogram for the direction of maximum estimation error in the case of pinna prototypes augmented with different local shape features. The description of labels for the eight circular histograms are : N.F(No feature), R(Ridge), I(Incision), AT(Antitragus), R+I(Ridge+Incision), I+AT(Incision+antitragus), R+AT(Ridge+antitragus), R+I+AT(Ridge+Incision+Antitragus).Freedman Diacanis rule has been used to compute the number of bins in each plot.

As for the preferred orientation of the error ellipses, the circular histogram for the pinna model with no local shape features added to it, resembled the circular histogram of numerical pinna discussed in the previous chapters (Figure 4.4). With the addition of individual features, the circular histogram changed in a peculiar way with antitragus appearing to have the least effect. In cases where a pair of local shape feature were added to the original pinna, the effects of incision were always suppressed by the accompanying local shape feature. Finally for the case where all local shape features were added to the pinna, the circular histogram turned out to be extremely different from the case where the pinna carried no local shape features.

4.3 Dynamic motion in baffle shapes

A bat in its pursuit of target has to modify its sonar for tasks ranging from detection to classification and localization. Each of these tasks has its own requirement which at times are contradictory. For example, maximum detection requires the portion of beampattern with maximum sensitivities to be directed at the target for all the frequencies. This results in a maximum signal to noise ratio, besides producing a flat spectrum for the pulse on which target spectrum could be imprinted in the returning echo which further helps in classification. For best localization, however, the portion of beampattern with maximum variations in sensitivity needs to be directed towards the target so that the directional information of the target could be imprinted on the echo. This requires on the part of the pulse, a spectrum far different from a flat one i-e a pulse spectrum that changes a lot with frequency and direction. Thus to accommodate these conflicting requirements while switching from one task to another, some species of bats have developed special kind of features and muscles on their emission and reception sides respectively which helps them in switching from one type of beampatterns to another. An example of the effect of such kind of muscles on the reception side of a horseshoe bat is shown in Figure 4.5.

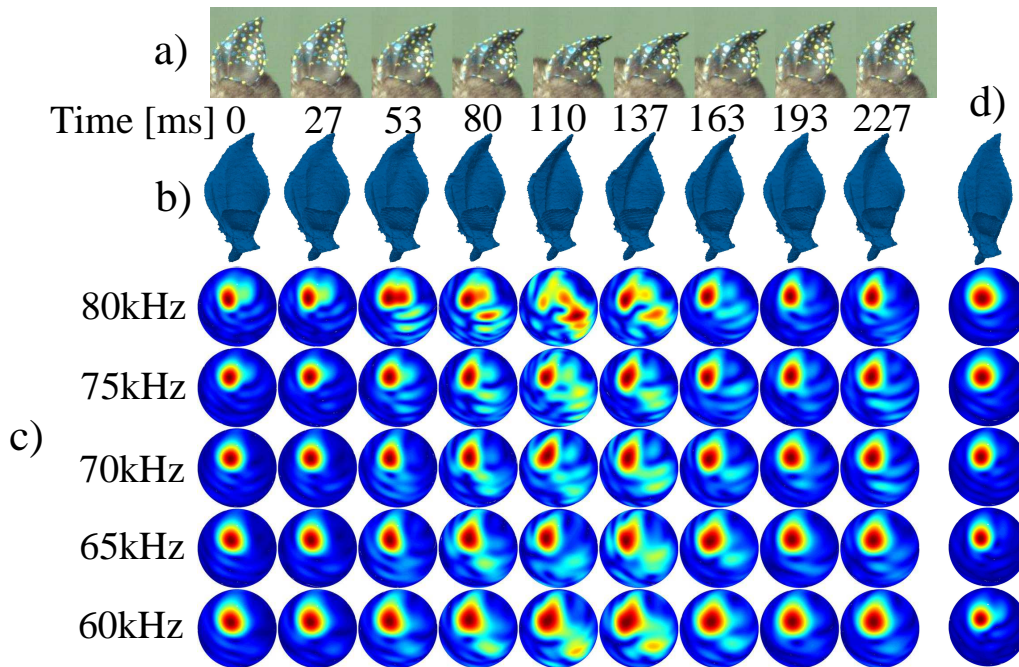


Figure 4.5: Depiction of non rigid motion of pinna in a Horseshoe bat using high speed video images, numerical models of pinna and numerical beam pattern estimates. Panel A represents the high speed video images of a pinna deformation from an upright position to the bent position and back to the upright position. The digits below panel A represent the recording time. Panel b represents the numerical models of pinna for each respective position shown in panel A. Panel c represents the numerical estimates of beam pattern for each respective position. The different rows in panel c represent different frequencies. Panel d represent the numerical model of a pinna and its respective beam pattern estimates without taking into consideration any type of dynamic motion of pinna. Reproduced with permission from the author⁸⁷

Panel A represents the high-speed images of a pinna moving from its upright position, shown in frame 1 to the bent position, shown by frame 5 and back to its upright position (frame 9). During this process, the numerical beam pattern estimates obtained through the numerical model of the pinna, shown in panel B, transform from a type of beam pattern that has only major lobe (column 1 of panel C) to the one where sensitivity is distributed into major and minor lobes (column 5 of panel C). Panel D represent the numerical beam pattern estimates obtained without taking into consideration any type of dynamic motion in pinna. Clearly the dynamic motion adds a lot of new information to the bat which is being shown by the changes in

the beampattern estimates. Such a motion in which the tip of the pinna moves down and to the side is also termed as nonrigid deformation as it changes the geometry of the pinna and hence the beampattern also. Aside from this, the pinna of a horseshoe bat also undergoes rigid motion in which the pinna as a whole moves forward and backward, thereby changing the orientation of the pinna and hence the orientation of beampattern. The importance of such motion has been established through anatomical work⁸⁹ as well as behavioral experiments³⁷. In the following analysis, physical and numerical models of baffle shapes have been used to understand the acoustic effects of dynamic motion on the estimation performance of a pinna and noseleaf in Horseshoe bat.

4.3.1 Dynamic motion in pinna

A horseshoe bat is an example of a heavy duty cycle bat that achieves superior performance in terms of navigation, hunting and other tasks, through the use of its noseleaf and pinna. The features on its baffle shapes and their motion produce direction dependent acoustic cues that encode useful information about the presence, location and characteristic of a sound source. In the current work, the dynamic motion of baffle shapes in horseshoe bat has been investigated using physical and numerical models. The purpose of this practice is to ascertain the effects of dynamic motion of shape features on the sensory information that is conveyed to the bat biosonar system. Furthermore an effort has been made to determine the usefulness of that information for localization of targets in bats.

Physical model of pinna

The use of a physical model for a baffle shape bears several advantages. For example, several aspects of a baffle shape like the local shape features and their dynamic motions can be modified which are either complicated or unethical to implement in the case of a live animal. A simplified version of the baffle shape can also provide greater opportunities to understand the underlying physical processes at a smaller or simpler scale. Additional modifications in the shape features and dynamics could be made to the extent that they may not be present in the living model but the study of which could prove to be insightful and technically useful. Experiments on physical models also provide a large amount of data which is reproducible⁸⁴.

In the current research, data from a physical model of a pinna, constructed in⁹⁰

and discussed in the previous section has been utilized for the purpose of analysis. The physical pinna was able to move from an upright position to the bent position in seven steps. At each step, five frequencies were used for the purpose of characterizing the performance of pinna. The average beam pattern and the resulting error ellipses plot due to the combined effect of 5 frequencies at an upright position of the pinna is shown in Figure 4.6 a). Figure 4.6 b) represents the average beam pattern and the corresponding error ellipses plot for the pinna in the case where dynamic motion is taken into consideration by including into the analysis all frequencies (5 at each stage) and all stages of dynamic motion (7 stages).

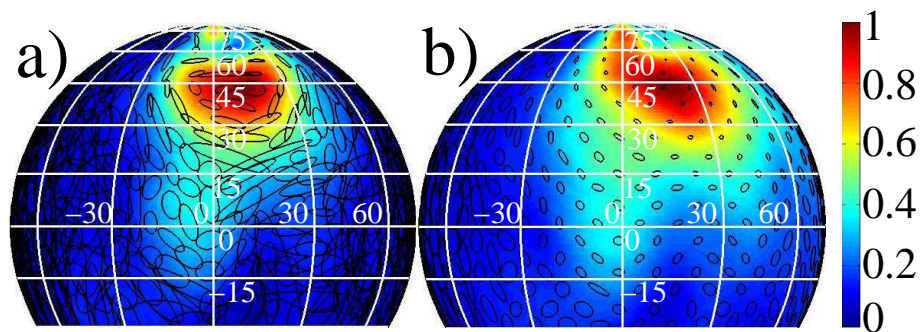


Figure 4.6: Depiction of the effects of bending in physical pinna on the localization performance of a bat using error ellipses plot. Bending of pinna encodes useful sensory information that reduces estimation error. Figure 4.6 a) and Figure 4.6 b) represents error ellipses plot with and without taking into consideration, bending of a physical pinna respectively. Numbers in white color along the vertical line represent the elevation values while numbers arranged along the horizontal direction represent azimuth values.

The changes in the size and the shape of the error ellipses are clearly visible in Figure 4.5 which can be further quantified through the use of metrics like maximum estimation error and error anisotropy, the histogram for which are shown below.

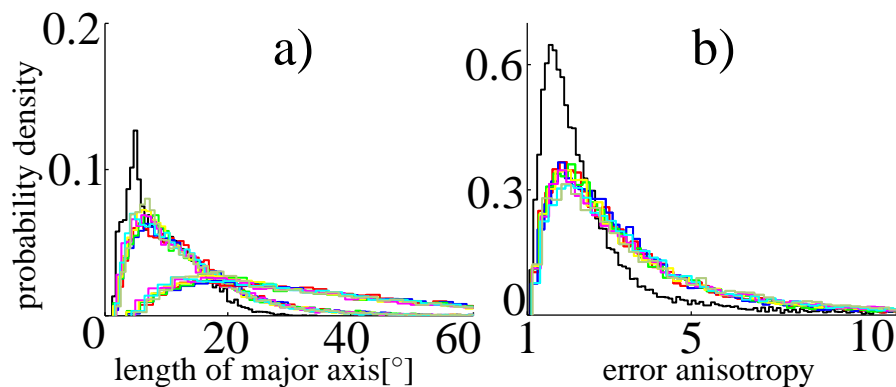


Figure 4.7: Effects of bending in physical pinna on metric values like maximum estimation error and error anisotropy. A pinna bending in stages (here 7) produces less estimation error than if it had stayed in a static position for the entire duration of bending. Bending also results in a final estimate that is less anisotropic. Black solid lines represent metric values obtained using beampatterns of seven different bending stages while plots of other color represent metric values obtained using either one or seven identical copies of beampatterns for a respective bending stage. Multiple identical copies of beampatterns have been included into the analysis to check whether the improvement in the estimation performance is due to increased number of observations or it is due to new information. The first group of colored curves towards the right side of the black solid line in Figure 4.7 a) represents plots of maximum estimation error obtained by taking into consideration seven identical copies of beampatterns for a specific bending stage while the second group of curves towards right side of the first group represents the metric values obtained using a single copy of beampatterns for a specific bending stage. As error anisotropy resulting from the analysis of a single beampattern is same as one resulting from several identical copies of it therefore there is no second group of curves in Figure 4.7 b). The color scheme used for different bending stages is, bending stage no.1 (Red Solid curve), bending stage no.2 (Blue Solid curve), bending stage no. 3 (Green Solid curve), bending stage no. 4 (Yellow solid curve), bending stage no. 5 (Magenta Solid curve), bending stage no.6 (Cyan Solid curve), bending stage no. 7 (Moss green Solid curve).

The average maximum estimation error obtained from the analysis of the directivity data (beampatterns) for seven different bending stages of a pinna (solid black line in Figure 4.7) is smaller than the average maximum estimation error obtained by

analyzing seven identical copies of the directivity data for any single bending stage (colored group of histograms encountered first while moving right from the black histogram in Figure 4.7). Quantitatively the percent differences between the average values of the two vary from 44.3 % to 35.8 %. The differences between the cases where bending is taken into consideration (solid black line) and the one where it is not (represented by the second group of colored histogram towards the right side of the black histogram) are starkest. The percent differences in the average values of maximum estimation error between these two groups vary from 122.4 % to 117.5 %.

Aside from the size of an error ellipse, the shape of an error ellipse in an error ellipses plot is also affected by bending of a pinna. Histogram for the error anisotropy, a metric, that characterizes the shape of an error ellipse is shown in Figure 4.7 b). Clearly bending results in less anisotropic estimates with percent differences between the average values of error anisotropy in the case where bending is taken into account and the one where it is not varying from 49.6 % to 30.9 %.

Numerical model of a pinna

Physical models of baffle shapes suffer from problems like noise, limited resolution, incompletely suppressed multipath or reverberations and variability in experimental conditions etc. Such models also provide limited flexibility in alteration of shape features and dynamics. Estimates of beampatterns obtained from numerical models of baffle shapes, on the other hand, provide higher resolution and can be obtained easily for a large number of frequencies and baffle shapes. The numerical 3D model of the baffle shape itself provides higher malleability, with options like rotation, scaling or removal of local shape features etc. In the current research work, beampattern estimates from numerical models of pinna were used for the purpose of analysis. The pinna was able to move from an upright position to the bent position in five steps. Five frequencies were used for the purpose of characterizing the performance of the pinna at each step of the dynamic motion. The resultant average beampattern and the respective error ellipses plot for the case where bending is taken into consideration and for the case where it is not are shown in Figure 4.8.

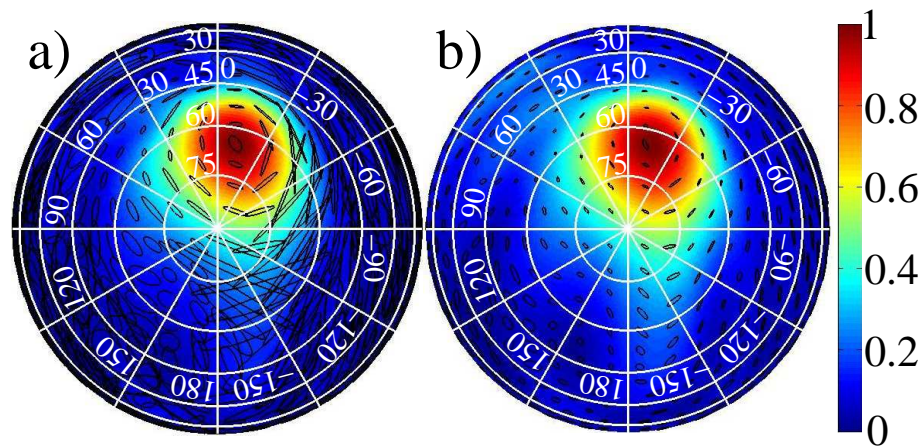


Figure 4.8: Depiction of the effects of bending in numerical pinna on the localization performance of a bat using error ellipses plot. Bending of pinna encodes useful sensory information that reduces estimation error. Figure 4.8 a) and Figure 4.8 b) represents error ellipses plot with and without taking into consideration, bending of a numerical pinna respectively. Numbers in white color along the vertical line represent the elevation values while numbers arranged in a circular format represent azimuth values.

Quantitatively the average value of maximum estimation error decreases by 87 % to 26 % as measurements are taken at different bending stages rather than having the same number of measurements at any single static bending stage except at bending stage number 5. In the case of bending stage number 5, repeated measurements outperform an equal number of different measurements in terms of maximum estimation error by 4.1 %. In the case where bending is taken into consideration, error anisotropy assumes an average value 31 % to 77 % lower than its average value in cases where bending is not taken into consideration. The results are shown in Figure 4.9.

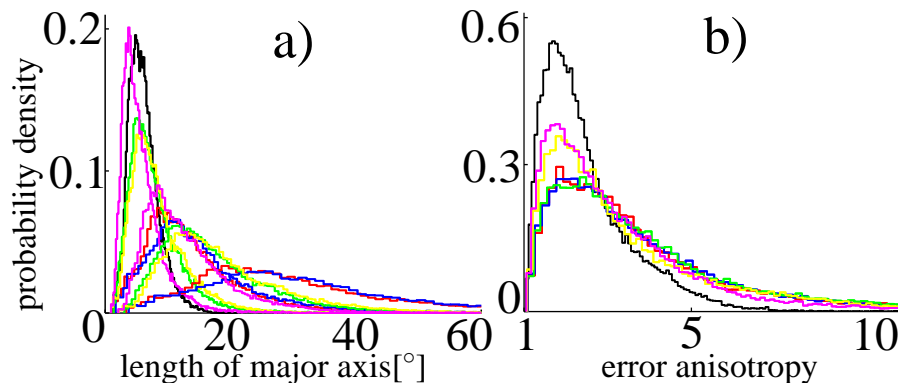


Figure 4.9: Effects of bending in numerical pinna on metric values like maximum estimation error and error anisotropy. A pinna bending in stages (here 5) produces less estimation error than if it had stayed in a static position for the entire duration of bending. Bending also results in a final estimate being less anisotropic. Black solid lines represent metric values obtained using beampatterns of five different bending stages. The first group of colored curves towards the right side of the black solid line in Figure 4.9 a) represents plots of maximum estimation error obtained by taking into consideration five identical copies of beampatterns belonging to a specific bending stage while the second group of curves towards right side of the first group represents the metric values obtained using a single copy of beampatterns for a specific bending stage. As error anisotropy resulting from the analysis of a directivity data (beampatterns) for a specific bending stage is same as one resulting from the analysis of several identical copies of the directivity data for the same bending stage therefore there is no second group of curves in Figure 4.9 b). The color scheme used for different bending stages is, bending stage no.1 (Red Solid curve), bending stage no.2 (Blue Solid curve), bending stage no. 3 (Green Solid curve), bending stage no. 4 (Yellow solid curve), bending stage no. 5 (Magenta Solid curve), all stages combined (Black solid curve)

4.3.2 Dynamic motion in noseleaf

The noseleaf of a horseshoe bat consist of features like an anterior leaf, posterior leaf(lancet), resonance cavities, sella etc. Each of these features undergoes motion that is assumed to have functional significance. For example, the walls of the anterior leave twitch forward and inward during emission of the pulses. The amount of displacement in the position of the walls could be as significant as one-quarter of

the wavelength used by a bat in its narrowband pulses. Furthermore, the twitching motion of the anterior leaf is actively controlled by the bat and can be turned on or off when needed. Such alignment of twitching motion with pulses and its active control provides evidence for the functional role of twitching motion in bats⁹¹. Sella^{92;93}, resonance cavities^{47;93} and lancet are other important features in the noseleaf that are assumed to play a vital role in controlling beamwidth. In the current research, physical as well as numerical models have been used to understand the acoustic effect of dynamic motion in noseleaf and the results are discussed in detail below.

Physical model of Noseleaf

A physical model of noseleaf⁹⁴ constructed using an elastic material was used for the purpose of analysis. The geometry and details of the model were obtained in⁹⁴ by μ CT scanning an actual noseleaf of a horseshoe bat. The size of the model was kept twice that of an actual noseleaf so as to allow for lower frequencies. The actuation of the lancet was achieved using a linear actuator which bent the lancet forward while pushing from behind. The lancet moved from an upright position to the bent position in six steps. At each step of the dynamic motion, six frequencies were used to characterize the performance the noseleaf. From the beampatterns for this baffle shape, the resulting error ellipses plot for the case where bending was taken into consideration and the case where it wasn't are shown in the Figure 4.10.

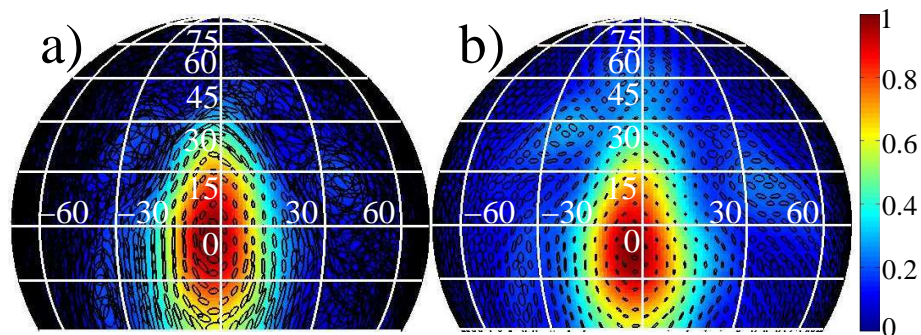


Figure 4.10: Bending of a lancet in noseleaf encodes useful sensory information that reduces estimation error. Figure 4.10 a) and Figure 4.10 b) represents error ellipses plot with and without taking into consideration, bending of lancet in physical noseleaf respectively.

Quantitatively, the average of the maximum estimation error obtained by evaluating

the data obtained during the course of bending of the lancet was 52 % to 17 % smaller than the average maximum estimation error that would have been obtained if the same number of measurements were taken while keeping the lancet stationary at any bending stage. If only one stage of dynamic motion with its performance being characterized through six frequencies was considered for the purpose of analysis then in comparison to the case where all the bending stages with all their frequencies were analyzed, the average value of the maximum estimation error rose by percent differences of 122.7 % to 97.4 % . The error anisotropy also changed as a result of taking into consideration bending of a lancet. The average error anisotropy decreased by 25.4 % to 21 % when evaluated data was embedded with the effect of bending.

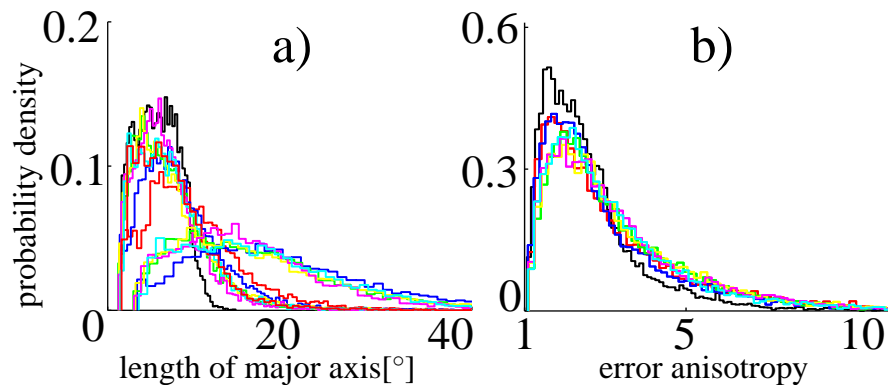


Figure 4.11: Effects of a bending lancet in physical noseleaf on metric values like maximum estimation error and error anisotropy. Average maximum estimation error obtained from the analysis of the directivity data (beampatterns) for six different stages of a bending lancet is smaller than the average maximum estimation error obtained by analyzing either a single or six identical copies of the directivity data for any single bending stage. Estimation error is also less anisotropic in the case where it has been generated using the directivity data for six different bending stages of a lancet. Black solid lines represent metric values obtained using beampatterns of six different bending stages. The first group of colored curves towards the right side of the black solid line in Figure 4.11 a) represents plots of maximum estimation error obtained by taking into consideration six identical copies of beampatterns for a specific bending stage while the second group of curves towards right side of the first group represents the metric values obtained using a single copy of beampatterns for a respective bending stage. As error anisotropy resulting from the analysis of a directivity data is same as one resulting from the analysis of several identical copies of it therefore there is no second group of curves in Figure 4.11 b). The color scheme used for different bending stages is, bending stage no.1 (Red Solid curve), bending stage no.2 (Blue Solid curve), bending stage no. 3 (Green Solid curve), bending stage no. 4 (Yellow solid curve), bending stage no. 5 (Magenta Solid curve), bending stage no.6 (Cyan Solid curve)

Numerical model of Noseleaf

A numerical model of the noseleaf can be obtained by μ CT scanning an actual noseleaf of a horseshoe bat. The resulting 3d numerical model can be rigged and animated to obtain numerical beampattern estimates of noseleaf with a lancet at

different positions. In the current work, the numerically generated lancet was able to move from an upright position to the bent position in four steps with its performance being characterized at each step of the bending through 5 frequencies. The resultant analysis is shown below:

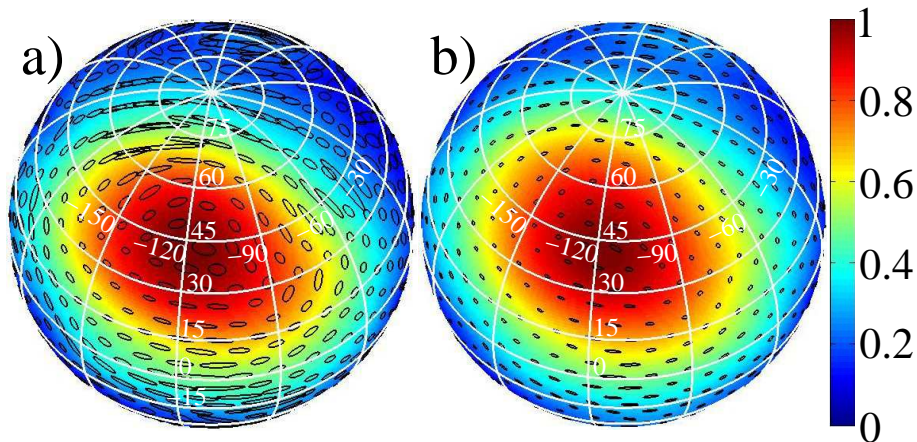


Figure 4.12: Depiction of the effects of bending in numerical noseleaf on the localization performance of a bat using error ellipses plot. Bending of lancet encodes useful sensory information that reduces estimation error. Figure 4.12 a) and Figure 4.12 b) represents error ellipses plot with and without taking into consideration, bending of a numerical noseleaf respectively.

The average value of maximum estimation error like the previous cases decreased as bending was taken into consideration. The percent decrease in the average values of maximum estimation error in the case where all bending stages were taken into consideration to the case where an identical number of measurements were taken at any single bending stage was in between 11 to 27 %. For the case where the comparison was carried out between the maximum estimation error, calculated using data at all different bending stages and the data at any single bending stage, the percent difference between the average values varied from 76 % to 90 %. Error anisotropy also decreased as bending was taken into consideration. The percent decrease was though limited to 14 to 21.6 %.

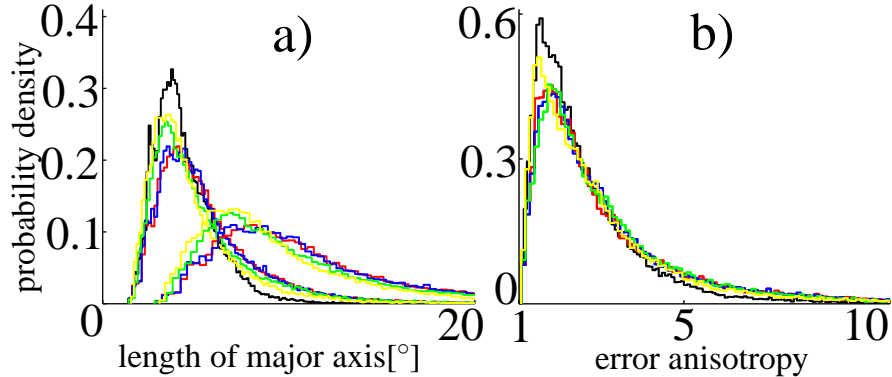


Figure 4.13: Effects of a bending lancet in numerical noseleaf on metric values like maximum estimation error and error anisotropy. Estimation error obtained from the analysis of the directivity data (beampatterns) for four different stages of a bending lancet is smaller than the estimation error obtained by analyzing either a single or four identical copies of the directivity data for any single bending stage. Estimation error is also less anisotropic in the case where it has been generated using the directivity data for four different bending stages of a lancet. Black solid lines represent metric values obtained using beampatterns of 4 different bending stages. The first group of colored curves towards the right side of the black solid line in Figure 4.13 a) represents plots of maximum estimation error obtained by taking into consideration four identical copies of beampatterns for a specific bending stage while the second group of curves towards right side of the first group represents the metric values obtained using a single copy of beampatterns for a respective bending stage. As error anisotropy resulting from the analysis of a directivity data is same as one resulting from the analysis of several identical copies of it therefore there is no second group of curves in Figure 4.13 b). The color scheme used for different bending stages is, bending stage no.1 (Red Solid curve), bending stage no.2 (Blue Solid curve), bending stage no. 3 (Green Solid curve), bending stage no. 4 (Yellow solid curve)

4.4 Combined effect of static shape features and their dynamic motion

The interaction of static local shape features and their effect on estimation performance while undergoing dynamic motion can also be studied. For this purpose the

physical model of pinna with different shape features constructed in⁹⁰ was utilized for the purpose of analysis. The said pinna was able to move from an upright position to the bent position in seven steps. As a result of bending, profound changes in the directivity pattern of pinna were observed. The directivity pattern for the pinna in an upright position consisted of mainly one major lobe which broke down into many when the pinna went into the bent position. (Figure 4.14 bending in pinna carrying no local shape features). Among the individual local shape features and their combinations, the pinna carrying only incision had the lowest estimation error for the first five bending stages. For the last two bending positions, the pinna with all local shape features added to it (ridge, incision and antitragus) had the best estimation performance while the combination of incision with ridge, had the worst estimation performance among all the combinations as well as individual shape features.

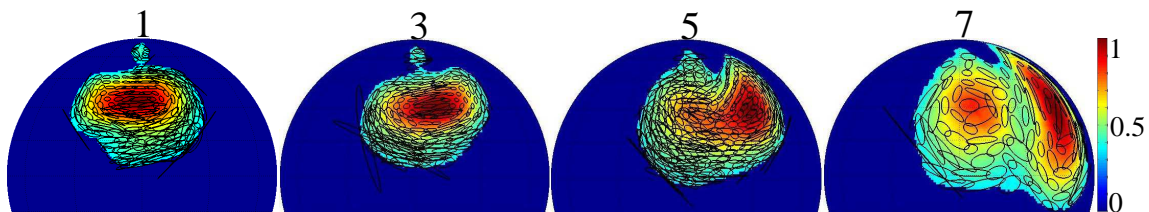


Figure 4.14: Error ellipses plot for the prototype of a horseshoe pinna carrying no local shape features. The labels from 1 to 7 represent the pinna positions with 1 and 7 representing the upright position and the bent position while the numbers in between represent the intermediate stages.

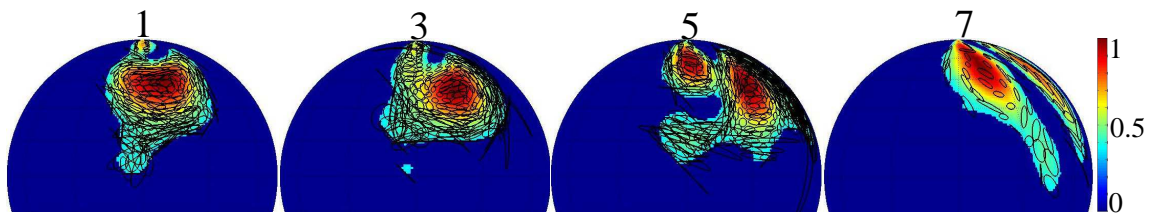


Figure 4.15: Error ellipses plot for the prototype of a horseshoe pinna augmented with all the features (ridge, incision and antitragus). The labels from 1 to 7 represent the pinna positions with 1 and 7 representing the upright position and the bent position while the numbers in between represent the intermediate stages.

4.5 Discussion

Static and dynamic shape features in bats play an important role in navigation, foraging and localization of a target. Static shape features consist of geometrical shapes like ridges, antitragus, incision etc. which interact with each other as well as with bended surface of the pinna. In the current work, an effort is made to determine the functionality of these local shape features by analyzing the data obtained from their simple prototypes. Each physically implemented local shape feature was found to have a unique characteristic and their combinations were able to achieve results that were not achievable through individual features. Different dynamic motions and their impact on the estimation performance of baffle shapes was also studied. Such dynamic motions were studied using several discrete positions of baffle shapes. In nature, the motion of the baffle shapes are continuous and therefore, any actual results obtained from that kind of continuous motion are expected to be much better than the ones obtained here. The effect seen on the estimation performance as a result of bending of a baffle shape were nearly the same across all datasets with the exception of numerical pinna in the case of which, maximum estimation error for the identical copies of one bending stage outperformed the result obtained using multiple bending stages. In all other cases, as well as in the case of error anisotropy that became less as lancet was bent, the similarity in the results despite the fact that the four datasets were generated in very different ways points to the conclusion that the effect seen here could not be attributed to any methodological artifacts. As numerical baffle shapes are a detailed reproduction of the geometric features of a live animal whereas the physical baffle shapes are highly simplified biomimetic models of the baffle shapes in alive animals, presence of similar effect in the analysis of both types of datasets points towards the robustness of the effects produced by dynamic motion. i.e the effects due to dynamic motion of the baffle shape are not very sensitive to any fine details of the noseleaf or pinna. This robustness of the effects is important for potential engineering applications because it suggests that the fundamental dynamic encoding phenomena could be exploited in man-made sensing systems even if these differ substantially from the specific biological shapes and configurations that inspired them.

Chapter 5

Summary

5.1 Research findings and their brief explanation

- The current work applies for the first ever time a quick and quantitative measure of estimation accuracy to a large and taxonomically diverse set of bat biosonar beampattern data. Such an effort provides an opportunity to make predictions about the direction-finding performance of bats across many species and families and hence to investigate the diversity in bats from the perspective of direction finding. The results clearly indicated as expected a large diversity in the size, shape and orientation of the error ellipses in the different beampattern samples analyzed. Within each beampattern of the analyzed samples, error ellipses differ (in some cases, more than others) in their properties, depending upon their exact location in the beampattern and the expected role of that portion of the beampattern. For example error ellipses at the center of the major lobe which is used for the detection purposes were found to be fat and big compared to the error ellipses on the edges of the major lobe which are small and hence used for localization purposes.
- The average values for the two important properties of error ellipses, the major and minor axes length across all analyzed samples and all directions that were evaluated for each sample supported the notion that bat biosonar beampatterns support fairly precise direction finding at the signal-to-noise ratio (60 dB) assumed here. The average lengths of the minor axis were 3.9° and 2.81° at lower beam gain thresholds of -30 dB and -18 dB respectively which are well aligned with the results of behavioral experiments (3°) for angular resolution in big

brown bat (*Eptesicus fuscus*).

- A positive skew was seen in the distributions for the lengths of the major and minor axes of the error ellipses, indicating that the bat biosonar beampatterns contain regions of comparatively low estimation accuracy. A probable reason for this could be the behavioral adaptations in bats, i.e., the use of prior knowledge by the bats to orient their beampattern to avoid the occurrence of targets in regions of low accuracy examples of which include bats using the slopes of their beampatterns for direction finding⁶⁶.
- Major differences were observed between the two types of beampatterns (emission and reception beampatterns) in terms of preferred orientation of the error ellipses. Most of the error ellipses in reception beampatterns were aligned in nearly the same direction (i.e. azimuth) perhaps owing to the fact that an ear has to sense weak signals for which it has to align the region of maximum sensitivity at different frequencies together as much as possible at least in the detection phase. It also shows that the estimation accuracy obtained from the use of monaural cues is better along the elevation direction than in azimuth. In the case of noseleaf, the error ellipses were oriented in all directions with ones in the azimuth slightly more in number than in other directions. The likely reason for this asymmetry is the complementary role of noseleaf in assisting the ear in detection phase. The noseleaf serves this purpose by distributing the energy in all directions but slightly more along the elevation thus improving the signal to noise ratio in the direction in which ears are most sensitive.
- Bats can be classified broadly into two categories, FM bats and CFFM bats, based on the design of their echolocation signal. Only reception beampatterns belonging to these two groups of bats were distinctly different from each other in terms of the distribution of their magnitude of estimation errors across the direction space at higher beam gain thresholds. The reception beampatterns for the two groups also differed in terms of preferred orientation of error ellipses with CFFM bats having a larger scatter in their orientation of the error ellipses than FM bats. The apparent reason for this could be the large inter frequency variations in the position of maximum sensitivity in FM bats that produces comparatively more notches and peaks and hence makes the effect of monaural cues stronger thereby making the direction finding along the elevation direction better. This can be recognized by the orientation of a large number of error ellipses in the azimuth direction in FM case.
- The average values of the minimum and maximum estimation error for the eight

different families of bats tended to form clusters with the overlap between them being much less at higher beam gain threshold (-18dB) than at lower beam gain threshold (-30dB). At higher beam gain threshold (-18dB), the overlap between the cluster was also much less in the case of ear than in the case of noseleaf. Hipposideridae had the lowest values for the minimum and maximum estimation error among all families of bats. Vespertilionidae and Pteropodidae respectively showed average performance while Rhinolophidae had the highest values of maximum estimation error at any beam gain thresholds as well as for any type of baffle shape whether ear or noseleaf. One apparent reason for this is the disregard of the effects that appear on the estimation performance of Rhinolophidae due to the dynamic motion in their noseleaf and pinna. Such effects have been incorporated later in the research for the bats in the family Rhinolophidae.

- In the second part of the research, effects of local shape features on the estimation performance of baffle shapes were studied. For this purpose, physically recorded beampattern estimates obtained after modifying local shape features were analyzed. Local shapes features demonstrated interesting properties. For example among the three individual local shape features, ridge, incision and antitragus, the incision had the best estimation performance while the ridge and antitragus were found to have the worst estimation performance. However the two local shape features (ridge and antitragus) together, provided the best or close to the best performance possible in combinations. Similarly incision together with ridge provided the worst estimation performance out of all the possible four combinations of the three local shape features.
- In terms of directivity of the pinna, addition of a ridge to the pinna produced asymmetry in the directivity pattern and removed any sidelobes present in the directivity of the original pinna. Addition of Incision to the original pinna produced a smaller major lobe and a stronger side lobe. It also reduced the size of the error ellipses throughout the directivity pattern of the pinna. Addition of antitragus to the original pinna, rotated the major lobe by a few degrees, increased the size of error ellipses by a small amount and produced a sidelobe. Addition of Incision to the already added ridge restored the symmetry in the directivity pattern and increased the size of the error ellipses besides producing a weak side lobe. Adding incision to the antitragus reduced the size of the major lobe, decreased the strength of side lobe and made the error ellipses slightly smaller. Addition of antitragus to the ridge restored the relative symmetry to the directivity pattern of the ridge, produced sidelobes and made the error

ellipses smaller. Finally adding all features together produced a major lobe with a shape closer to a circle than to a rectangle which matched the major lobe of the pinna carrying no feature

- The preferred orientation of error ellipses in the case of a physically implemented pinna with no local shape feature added to it, resembled the circular histogram of the numerical pinna in which the majority of the error ellipses are oriented in the horizontal direction. With the addition of each individual feature, the circular histogram changed in a peculiar way with antitragus appearing to have the least effect. In the case where a pair of local shape features were added, the effects of incision were always suppressed by the accompanying local shape feature. Finally for the case where all local shape features were added to the pinna, the circular histogram came out to be extremely different from the case where the pinna carried no local shape features.
- Some species of bats in the family Rhinolophidae undergo dynamic motion in their baffle shapes during the echolocation process. Two such types of dynamic motions are the motion of lancet and pinna from an upright position to the bent position. In the current work, through the analysis of beampatterns generated by numerical models as well as through physical models it has been demonstrated that bats use dynamic motion for encoding useful information.
- In terms of the directivity of the pinna, the effect of bending on a pinna carrying different local shape features was profound. The directivity pattern for the pinna in the upright position consisted of mainly one major lobe which broke down into many when the pinna went into the bent position. The estimation error was lowest in the case of pinna carrying only incision, for the first five bending stages. For the last two bending positions, the pinna with all local features added to it (ridge, incision and antitragus) had the best estimation performance. In terms of estimation performances of the combinations, the combination of incision with ridge, had the worst estimation performance among all the combinations as well as individual shape features.

5.2 Suggestions for future work

Future work could include an extension of the current analysis to eigenbeams that were obtained in³³ by decomposing 273 numerical beampatterns into a set of components beams, the weighted sum of which could produce any of the 273 numerical

beampatterns. Understanding the acoustic functionality of each eigenbeam and their interaction with each other in terms of direction finding performances could prove to be a stepping stone. Such a step could be coupled with the lessons learned from the study⁷⁷ that decomposed around 100 pinnae shapes into eigenears (a set of simple ears shapes, combination of which could produce any of the complicated 100 pinnae shapes) and the study of eigennoseleaf which is currently underway. Additional help could be obtained from the separate study of functionality of individual static and dynamic local shape features. The performance of such local shape features depends upon parameters (for example in the case of ripples, there are at least three parameters, amplitude, position and orientation of ripples). Combination of these parameters for different local shape features form a parameter space out of which parameters could be selected to design special baffle shapes to achieve specific tasks. Such a process could be automated as suggested in⁷⁸ by using genetic algorithms etc. It could also be made computationally less expensive through the use of less dense numerical meshes(that still retain the basic shape of the baffle but are made up of fewer points and are quick to produce beampatterns). Such a venture also requires a working knowledge of the connection between the eigenshapes and eigenbeams in the form of linkages that extend from the eigenear space or eigennoseleaf space to the eigenbeam space and are eventually connected to the biosonar performances.

The current work in itself could be improved by considering the dynamic motion of baffle shapes in families like Hipposideridae, Rhinolophidae etc, figuring out the alignment information between ear and noseleaf beampatterns, incorporation of inter aural intensity differences and inter aural time differences into the method for obtaining localization performance along the azimuth direction as well as incorporating any signal spectrum changes during detection, classification, localization or prey capture phases etc.

References

- [1] Sofla A.Y.N, Meguid S.A, Tan K.T, and Yeo W.K. *Shape morphing of aircraft wing : Status and challenges*. Elsevier Sci., Mater. Des., 31:1284–1292, March 2010.
- [2] Kesel A, Hielicke W, Stamhuis E. *Using bird flight modes to enhance overall flapping wing micro air vehicle performance*. SEB, July 2011.
- [3] Daniel L, Wei S, Mats B. *Flapping and flexible wings for biological and micro air vehicles*. Prog. Aerosp. Sci., 35:455–505, July 1999.
- [4] Dan K, Philip H, Robert J, and John G. *The dynamics of legged locomotion: Models, analyses, and challenges*. Siam Rev., 48:207–304, June 2006.
- [5] Meyers M.A, Lin Y.S, Lin A.Y.M. *The cutting edge: Sharp biological materials*. Jom, 60:19–24, March 2008.
- [6] Duncan G.R. *Tunable structural colour*. Nat. Photonics, 3:551–553, October 2009.
- [7] Sambles J.R and Vukusic P. *Photonic structures in biology*. Nature, 424:852–855, August 2003.
- [8] Bensaid S, Centi G, Garrone E, Perathoner S, Saracco G. *Towards artificial leaves for solar hydrogen and fuels from carbon dioxide*. Chemsuschem, 5:500–521, March 2012.
- [9] Akella K. *Biomimetic designs inspired by seashells*. Resonance, 17:573–591, June 2012.
- [10] Eisenbach M. and Balaban M. *Sensing and Response in Microorganisms*. Elsevier Science Publishers, Amsterdam, 1986.

- [11] Colombetti G. and Lenci F. *Membranes and sensory transduction*. Plenum Press, New York, 1984.
- [12] Park M, Tsai S.L, and Chen W. *Microbial biosensors: Engineered microorganisms as the sensing machinery*. *Sensors*, 13:5777–5795, May 2013.
- [13] Mandyam V, Srinivasan, Friedrich G, Barth, Joseph A.C, Humphrey. *Frontiers in sensing, from biology to engineering*. Springer-Verlag, Wien/Vienna, 2012.
- [14] Cowles R.B. Bullock T.H. *Physiology of an infrared receptor: The facial pit of pit vipers*. *Science*, 115:541–543, May 1952.
- [15] Krochmal A.R, LaDuc T.J, Bakken G.S. *Heat in evolution's kitchen: evolutionary perspectives on the functions and origin of the facial pit of pitvipers (viperidae: Crotalinae)*. *J. Exp. Biol.*, 207:4231–4238, 2004.
- [16] Klocke D, Schmitz A, Soltner H, Bousack H, and Schmitz H. *Infrared receptors in pyrophilous (fire loving) insects as model for new un-cooled infrared sensors*. *Beilstein J Nanotechnol.*, 2:186–197, 2011.
- [17] Goodman K, McCravy K.W. *Pyrophilous insects*. *Encyclopedia of Entomology*, Springer, pages 3090–3093, 2008.
- [18] Heiligenberg W. *Principles of Electrolocation and Jamming Avoidance in Electric Fish: A Neuroethological Approach*. Springer-Verlag, Berlin, Heidelberg, New York 1977.
- [19] Vischer H.A. *Electroreceptor development in the electric fish eigenmannia: a histological and ultrastructural study*. *J. Comp. Neurol.*, 30:81–100, 1995.
- [20] Wiltschko R. and Wiltschko W. *Sensing in Nature*, volume 1, chapter Magnetoreception, pages 126–141. Landes Bioscience and Springer Science+Business Media, New York, 2012.
- [21] Ritz T, Adem S, and Schulten K. *A model for photoreceptor-based magnetoreception in birds*. *Biophys. J.*, 78:707–718, February 2000.
- [22] Ritz T, Mouritsen H. *Magnetoreception and its use in bird navigation*. *Curr. Opin. Neurobiol.*, 15:406–414, August 2005.
- [23] Knight K. *Lateral line helps fish determine sound direction*. *J. Exp. Biol.*, 214: 1–1, 2011.

- [24] Ghysen A. Pichon F. *Evolution of posterior lateral line development in fish and amphibians*. *Evol. Dev.*, 6:187–193, May-June 2004.
- [25] Zelick R. Bleckmann H. *Lateral line system of fish*. *Integr. Zool*, 4:13–25, March 2009.
- [26] Müller R. and Kuc R. *Biosonar-inspired technology: goals, challenges and insights*. *Bioinspir. Biomim.*, 2:S146–S161, 2007.
- [27] Surlykke A, Fay R.R, Nachtigall P.E. and Popper A.N. *Biosonar*. Springer-Verlag New York 2014.
- [28] Müller R. *Numerical analysis of biosonar beamforming mechanisms and strategies in bats*. *J. Acoust. Soc. Am.*, 128:1414–1425, September 2010.
- [29] Nachtigall P.E and Moore P.W.B. *Animal Sonar, Processes and performance*. Plenum Press, New York, 1988.
- [30] Hill R.W, Anderson M, Wyse G.A. *Animal Physiology*. Sinauer Associates, Inc, Publishers, Sunderland, Massachusetts, 2012.
- [31] Wimsatt W.A. *Biology of bats*, volume 3, chapter Acoustic Orientation. Academic Press, New York, San Francisco and London, 1977.
- [32] Motamedi M. and Müller R.. *Characterization of the diversity in bat biosonar beam patterns with spherical harmonics power spectra*. *J. Acoust. Soc. Am*, 135: 3613–3619, June 2014.
- [33] Caspers P. and Müller R. *Eigenbeam analysis of the diversity in bat biosonar beam patterns*. *J. Acoust. Soc. Am*, 137:1081–1087, March 2015.
- [34] Gilani S.U, Müller R. *An assessment of the direction-finding accuracy of bat biosonar beam patterns*. *J. Acoust. Soc. Am.*, 139:569–580, 2016.
- [35] edited by Wilson D.E and Reeder D.M. *Species of the World: A Taxonomic and Geographic Reference, vol 1, 3rd Edition* Baltimore, Md: Johns Hopkins University Press, PP 312-529
- [36] Vaughan T.A, Ryan J.M, Czaplewski N.J. *Mammalogy, Fifth Edition*. Jones and Bartlett Publishers, Sudbury, Massachusetts, 2011.

- [37] Mogdans J, Ostwald J, and Schnitzler H.U. *The role of pinna movement for the localization of vertical and horizontal wire obstacles in the greater horseshoe bat, Rhinolophus ferrumequinum.* J. Acoust. Soc. Am., 84:1676–1679, 1988.
- [38] Lawrence B.D, Simmons J.A, Kick S.A. *Acuity of horizontal angle discrimination by the echolocating bat, eptesicus fuscus.* J. Comp. Physiol., 153:321–330, 1983.
- [39] Simmons J.A. and Lawrence B.D. *Echolocation in bats: the external ear and perception of the vertical positions of targets.* Science, 218:1034–1041, October 1982.
- [40] Simmons J.A and Wotton J.M. *Spectral cues and perception of the vertical position of targets by the big brown bat, eptesicus fuscus.* J. Acoust. Soc. Am., 107:1034–1041, February 2000.
- [41] Webster F.A and Brazier O.G. *Experimental studies on target detection, evaluation and interception by echolocating bats.* Technical Report TDR, Aerospace Medical Division, USAF Systems Command, Tuscon, Az., AMRL-tr-65-172, 1965.
- [42] Ghose K. and Moss C.F. *The sonar beampattern of a flying bat as it tracks tethered insects.* J. Acoust. Soc. Am., 114:1120–1131, 2003.
- [43] Brinklov S, Jakobsen L. and Surlykke A. *Intensity and directionality of bat echolocation signals.* Front Physiol., 4:89, April 2013.
- [44] Fuzessery P.B, Buitenhoff P, Andrews B, Kennedy J. *Passive sound localization of prey by the pallid bat (antrozous p. pallidus).* J. Comp. Physiol., 171:767–777, 1993.
- [45] Müller R. *A numerical study of the role of the tragus in the big brown bat.* J. Acoust. Soc. Am., 116:3701–3712, 2004.
- [46] Dreyer D. and Estorff. O.V. *Improved conditioning of infinite elements for exterior acoustics.* Int. J. Numer. Meth. Eng., 58:933–953, 2003.
- [47] Zhuang Q. and Müller R. *Noseleaf furrows in a horseshoe bat act as resonance cavities shaping the biosonar beam.* Phys. Rev. Lett., 97:218701, 2006.
- [48] Obrist M.K, Eger J.L, Fenton M.B and Schlegel P.A. *What ears do for bats: A comparative study of pinna sound pressure transformation in chiroptera.* J. Exp. Biol., 180:119–152, March 1993.

- [49] Kalkan Y. *Cramé-rao bounds for target position and velocity estimations for widely separated mimo radar*. Radioengineering, 22:1156–1161, December 2013.
- [50] Censi A. *On achievable accuracy for range-finder localization*. IEEE Int. Conf. Robot., pages 4170–4175, April 2007.
- [51] Wang J, Liu Z. and Chen W. *Localizability estimation for mobile robots based on probabilistic grid map and its applications to localization*. IEEE Int. Conf. Robot. Autom., pages 46–51, September 2012.
- [52] Pourhomayoun M. and Fowler M. *Cramé-rao lower bounds for estimation of phase in lbi based localization systems*. Forty Sixth ASILOMAR Conf., pages 909–911, November 2012.
- [53] Müller R, Lu H, and Buck J.R. *Sound-diffracting flap in the ear of a bat generates spatial information*. Phys. Rev. Lett., 100:108701, March 2008.
- [54] Yovel Y, Arditi G., Weiss A.J. *Object localization using a biosonar beam: how opening your mouth improves localization*. R. Soc. Open Sci., 2:909–911, August 2015.
- [55] Kay S. *Fundamentals of Statistical Signal Processing*, volume 1, chapter Cramé Rao Lower Bound, pages 27–77. Prentice hall, New Jersey, 2nd Edition, 1993.
- [56] Husson F, Le S. and Pages J. *Confidence ellipse for the sensory profiles obtained by principal component analysis*. Food Qual. Prefer., 16:245 – 250, 2005.
- [57] Eberly D. *Information about ellipses*, Geometric tools, LLC, <http://www.geometrictools.com/>, USA, 2011.
- [58] Press. W.H *Numerical recipes in C: The art of scientific computing*, volume 1, chapter Modeling of data, pages 689–699. 2nd edition, Press Syndicate of the University of Cambridge, New York, USA, 1992.
- [59] Hoover W.E. *Algorithms for confidence circles and confidence ellipses* Noaa Technical Report, 107:, September 1984.
- [60] Hivon E, Gorski K.M. and Banday A.J. *Healpix: A framework for high-resolution discretization and fast analysis of data distributed on the sphere*. Astrophys. J., 622:759–771, April 2005.
- [61] Coles S. *An introduction to the statistical modeling of extreme values*. Springer-Verlag London, 2001.

- [62] Batschelet E. *Circular Statistics in Biology (Mathematics in biology)*. Academic Press Inc, London, 1981.
- [63] Berens P. *Circstat: A matlab toolbox for circular statistics*. J. Stat. Softw., 31: 1–21, September 2009.
- [64] Lazure L, Fenton M.B. *High duty cycle echolocation and prey detection by bats*. J. Exp. Biol., 214:1131–1137, September 2011.
- [65] Fenton MB, Faure PA, Ratcliffe JM. *Evolution of high duty cycle echolocation in bats*. J. Exp. Biol., 215:2935–44, September 2012.
- [66] Moss C.F, Yovel Y, Falk B. and Ulanovsky N. *Optimal localization by pointing off axis*. Science, 327:701–704, February 2010.
- [67] UU UA. *Characterisation of time varying directivity of sound emission and sound reception for the different bat species*. Chiroping deliverable D.2.1.1, chiroping consortium, pages 1–24, 2010.
- [68] Lawrence B.D. and Simmons J.A. *Echolocation in bats: The external ear and perception of the vertical positions of targets*. Science, 218:481–483, 1982.
- [69] Grinnell A.D. and Schnitzler H.U. *Directional sensitivity of echolocation in the horseshoe bat, rhinolophus ferrumequinum*. J. Comp. Physiol., 116:51–61, 1977.
- [70] Long G.R and Schnitzler H.U. Behavioral audiograms from the bat, rhinolophus ferrumequinum. *J. Comp. Physiol.*, 100:211–219, 1975.
- [71] Stoica P. and Babu P. The Gaussian Data Assumption Leads to the Largest Cramé-Rao Bound [Lecture Notes]. *IEEE Signal Process. Mag.*, 28:132–133, 2011.
- [72] Park S., Serpedin E. and Qaraqe K. Gaussian Assumption: The Least Favorable but the Most Useful. *IEEE Signal Process. Mag.*, 30:183–186, 2013.
- [73] Surlykke A. and Kalko EK. *Echolocating bats cry out loud to detect their prey*. Plos One, 3:e2036, April 2008.
- [74] Blauert J. *Spatial Hearing: The Psychophysics of Human Sound Localization*. The MIT Press, Cambridge, Massachusetts, 1999.
- [75] Tollin DJ. *The lateral superior olive: A functional role in sound source localization*. Neuroscientist, 9:127–143, April 2003.

- [76] Poganiatz I, Jacobson G. and Nelken I. *Synthesizing spatially complex sound in virtual space: an accurate offline algorithm*. J. Neurosci. Methods, 106: 29–38, March 2001.
- [77] Ma J. and Müller R. *A method for characterizing the biodiversity in bat pinnae as a basis for engineering analysis*. Bioinspir. Biomim., 6:026008, 2011.
- [78] Müller R. and Hallam J.C.T. *From bat pinna to sonar antennae: Augmented obliquely truncated horns as a novel parametric shape model*. SAB 2004 (MIT, Cambridge, MA, 2004), pages 87–95, 2004.
- [79] Kuc R. *Model predicts bat pinna ridges focus high frequencies to form narrow sensitivity beams*. J. Acoust. Soc. Am., 125:3454–3459, May 2009.
- [80] Wotton J.M, Haresign T, and Simmons J.A. *Spatially dependent acoustic cues generated by the external ear of the big brown bat, *Eptesicus fuscus**. J. Acoust. Soc. Am., 98:1423–1445, 1995.
- [81] Weikai H, Pedersen S.C, Gupta A.K, Simmons J.A, and Müller R. *Lancet dynamics in greater horseshoe bats, *rhinolophus ferrumequinum**. Plos One, 10: e0121700, April 2015.
- [82] Müller R, Zhang Z, and Truong S.N. *The acoustic implications of sella length in horseshoe bats*. J. Acoust. Soc. Am. , 125:2678–2678, 2009.
- [83] Zhang Z, Truong S.N, and Müller R. *Acoustic effects accurately predict an extreme case of biological morphology*. Phys. Rev. Lett., 103:038701, July 2009.
- [84] Pannala M. *Investigation of dynamic ultrasound reception in bat biosonar using a biomimetic pinna model*. Doctoral dissertation, Virginia Tech, page 85, 2013.
- [85] Pannala M, Meymand S.Z, and Müller R. *Interplay of static and dynamic features in biomimetic smart ears*. Bioinspir. Biomim., 8:026008, 2013.
- [86] Fletcher N.H and Thwaites. S. *Obliquely truncated simple horns:idealized models for vertebrate pinna*. Acust., 65:194–204, 1988.
- [87] Balakrishnan S. *A Numerical Elastic Model for Deforming Bat Pinnae* Master’s Thesis, Virginia Tech, page 49, 2010.
- [88] Gao L, Balakrishnan S, He W, Yan Z, and Müller R. *Ear deformations give bats a physical mechanism for fast adaptation of ultrasonic beampatterns*. Phys. Rev. Lett., 107:214301, Nov 2011.

- [89] Schneider H and Möhres F.P. *Die Ohrbewegungen der Hufeisenfledermäuse (Chiroptera, Rhinolophidae) und der Mechanismus des Bildhörens.* J. Comp. Physiol. A, 44:1–40, 1960.
- [90] Müller R, Pannala M, Reddy O.P.K, and Meymand S.Z. *Design of a dynamic sensor inspired by bat ears.* Smart Mater. Struct., 21:094025, 2012.
- [91] Lu H, Feng L, Gao L. and Müller R. *Noseleaf dynamics during pulse emission in horseshoe bats.* Plos One, 7, May 2012.
- [92] Zhang Z, Truong S.N, and Müller R. *Acoustic effects accurately predict an extreme case of biological morphology.* Phys. Rev. Lett., 103:038701, July 2009.
- [93] Zhuang Q. and Müller R. *Numerical study of the effect of the noseleaf on biosonar beamforming in a horseshoe bat.* Phys. Rec. E., 76:1–11, November 2007.
- [94] Fu Y. *Dynamic emission baffle inspired by horseshoe bat noseleaves.* Doctoral dissertation, Virginia Tech, 2016.
- [95] Coe D. and Moustakas L.A. *Cosmological Constraints from Gravitational Lens Time Delays* Astrophys. J., 706:1–11, 2009.

Appendices

Appendix A

A.1 Physically implemented local shape features

Position 1 -Upright position

Local shape feature	major axis	minor axis	ratio (major/minor)	\sqrt{area}
NF	14.65 ± 10.95	3.05 ± 1.51	7.83 ± 12.79	10.97 ± 5.07
R	16.65 ± 10.82	4.01 ± 2.21	7.22 ± 13.50	13.46 ± 6.48
I	11.83 ± 6.94	2.40 ± 1.56	9.04 ± 14.02	8.65 ± 3.84
AT	16.22 ± 10.66	2.91 ± 1.32	8.78 ± 13.72	11.19 ± 4.10
R+I	15.92 ± 8.42	4.35 ± 2.08	6.83 ± 13.36	13.76 ± 5.10
I+AT	15.20 ± 10.10	3.09 ± 2.16	9.24 ± 14.96	11.05 ± 5.65
R+AT	14.60 ± 8.91	3.29 ± 1.68	8.16 ± 14.28	11.29 ± 4.31
R+AT+I	15.14 ± 10.01	3.60 ± 2.15	7.87 ± 13.54	12.05 ± 5.71

Table A.1: Metric values for the local shape features ridge, incision, antitragus and their combinations, when the pinna is in position no. 1 (The upright position)

Position 2

Local shape feature	major axis	minor axis	ratio (major/minor)	\sqrt{area}
NF	15.35 ± 11.04	2.77 ± 1.39	8.56 ± 13.19	10.59 ± 4.83
R	18.06 ± 11.40	4.23 ± 2.46	7.45 ± 13.53	14.35 ± 6.81
I	12.17 ± 7.20	2.41 ± 1.52	9.45 ± 15.45	8.77 ± 3.90
AT	14.20 ± 7.84	3.03 ± 1.41	8.13 ± 13.97	10.75 ± 3.84
R+I	16.42 ± 9.32	4.73 ± 2.27	6.02 ± 11.45	14.64 ± 5.74
I+AT	16.45 ± 10.49	3.60 ± 2.48	8.59 ± 15.06	12.45 ± 6.41
R+AT	14.45 ± 8.76	3.42 ± 1.60	7.27 ± 12.51	11.47 ± 4.17
R+AT+I	15.68 ± 11.74	3.70 ± 2.15	7.79 ± 14.62	12.35 ± 6.20

Table A.2: Metric values for the local shape features ridge, incision, antitragus and their combinations, when the pinna is in position no. 2.

Position 3

Local shape feature	major axis	minor axis	ratio (major/minor)	\sqrt{area}
NF	14.42 ± 10.30	2.81 ± 1.40	7.85 ± 12.76	10.44 ± 5.14
R	18.95 ± 13.15	4.27 ± 2.21	6.76 ± 11.99	14.80 ± 7.05
I	15.10 ± 12.79	2.53 ± 1.51	8.83 ± 13.94	10.11 ± 6.02
AT	13.91 ± 7.86	3.56 ± 1.92	6.97 ± 12.86	11.61 ± 5.14
R+I	16.84 ± 9.58	4.71 ± 2.06	5.89 ± 10.70	14.83 ± 5.39
I+AT	16.84 ± 11.66	3.80 ± 2.64	8.05 ± 14.44	12.96 ± 7.21
R+AT	15.53 ± 10.36	3.55 ± 1.64	7.36 ± 12.42	12.10 ± 4.59
R+AT+I	15.49 ± 11.98	3.96 ± 2.33	6.97 ± 13.57	12.61 ± 6.08

Table A.3: Metric values for the local shape features ridge, incision, antitragus and their combinations, when the pinna is in position no. 3.

Position 4

Local shape feature	major axis	minor axis	ratio (major/minor)	\sqrt{area}
NF	15.02 ± 13.86	3.26 ± 1.63	7.11 ± 12.52	11.36 ± 5.83
R	19.40 ± 13.72	4.54 ± 2.28	6.47 ± 11.88	15.41 ± 7.20
I	13.46 ± 9.93	2.74 ± 1.43	8.01 ± 14.10	9.96 ± 4.86
AT	16.15 ± 10.38	4.11 ± 2.46	6.93 ± 12.19	13.34 ± 6.45
R+I	17.14 ± 9.90	4.61 ± 2.61	6.71 ± 12.04	14.62 ± 6.25
I+AT	15.69 ± 10.10	3.66 ± 2.43	8.11 ± 14.10	12.15 ± 5.70
R+AT	16.18 ± 10.25	3.66 ± 1.64	6.96 ± 11.33	12.64 ± 4.64
R+AT+I	14.94 ± 10.47	3.99 ± 2.48	6.65 ± 12.85	12.43 ± 5.98

Table A.4: Metric values for the local shape features ridge, incision, antitragus and their combinations, when the pinna is in position no. 4.

Position 5

Local shape feature	major axis	minor axis	ratio (major/minor)	\sqrt{area}
NF	15.71 ± 11.34	3.88 ± 1.96	6.77 ± 12.54	12.79 ± 6.10
R	19.28 ± 13.24	4.64 ± 2.43	6.58 ± 12.42	15.55 ± 7.20
I	15.08 ± 9.01	3.29 ± 1.52	7.38 ± 12.71	11.67 ± 4.78
AT	18.84 ± 11.69	4.09 ± 2.33	8.01 ± 13.48	14.28 ± 6.12
I+AT	17.94 ± 12.04	4.09 ± 3.00	8.15 ± 12.95	13.84 ± 7.64
R+AT	16.97 ± 10.50	3.84 ± 1.74	6.94 ± 11.31	13.29 ± 4.77
R+AT+I	17.71 ± 12.57	3.86 ± 2.36	8.05 ± 13.48	13.47 ± 7.34

Table A.5: Metric values for the local shape features ridge, incision, antitragus and their combinations, when the pinna is in position no. 5.

Position 6

Local shape feature	major axis	minor axis	ratio (major/minor)	\sqrt{area}
NF	17.12 ± 11.13	4.40 ± 2.10	6.39 ± 11.66	14.20 ± 5.63
R	20.01 ± 14.64	4.72 ± 2.40	6.22 ± 11.34	15.93 ± 7.58
I	16.77 ± 12.29	4.29 ± 2.34	6.71 ± 12.78	13.84 ± 6.52
AT	24.26 ± 17.78	4.83 ± 2.91	8.37 ± 12.91	17.35 ± 8.07
R+I	23.26 ± 19.87	5.86 ± 5.51	9.08 ± 16.14	18.92 ± 15.75
I+AT	20.21 ± 14.62	4.41 ± 2.91	8.20 ± 13.21	15.21 ± 7.62
R+AT	18.51 ± 11.53	4.27 ± 2.49	7.50 ± 12.22	14.51 ± 6.07
R+AT+I	14.83 ± 9.43	2.88 ± 1.58	9.06 ± 13.36	10.55 ± 4.37

Table A.6: Metric values for the local shape features ridge, incision, antitragus and their combinations, when the pinna is in position no. 6.

Position 7 -Bent position

Local shape feature	major axis	minor axis	ratio (major/minor)	\sqrt{area}
NF	20.18 ± 13.65	4.68 ± 2.18	6.85 ± 11.80	15.88 ± 6.25
R	20.24 ± 15.75	4.78 ± 2.50	6.71 ± 12.90	16.13 ± 7.76
I	24.92 ± 18.90	4.85 ± 3.09	8.27 ± 13.31	17.73 ± 9.57
AT	31.17 ± 23.02	6.22 ± 4.23	8.88 ± 13.23	22.33 ± 11.49
R+I	24.78 ± 18.85	6.32 ± 4.45	6.74 ± 10.44	20.72 ± 13.03
I+AT	20.57 ± 12.95	4.36 ± 2.43	8.19 ± 13.03	15.24 ± 6.11
R+AT	24.04 ± 18.46	4.75 ± 2.96	8.09 ± 12.15	17.45 ± 9.39
R+AT+I	18.50 ± 11.95	3.54 ± 2.48	10.28 ± 15.76	12.85 ± 5.94

Table A.7: Metric values for the local shape features ridge, incision, antitragus and their combinations, when the pinna is in position no. 7 (The bent position).

Appendix B

B.1 Hipposideridae (Reception beampatterns)

Hipposideridae	major axis	minor axis	ratio (major/minor)
Aselliscus stoliczkanus	19.4	6.0	4.6
	19.1	7.2	3.7
Coelops frithii	8.4	3.9	2.4
	9.6	4.2	2.6
Hipposideros armiger	6.4	3.0	2.3
	5.7	2.6	2.2
	7.5	3.4	2.4
Hipposideros cineraceus	12.8	5.5	2.6
	9.9	4.6	2.4
	3.2	1.4	2.4
Hipposideros galeritus	11.8	5.7	2.3
	12.0	6.2	2.2
	10.2	5.5	2.0
Hipposideros larvatus	11.4	5.3	2.3
	8.7	3.7	2.6
	7.0	3.4	2.2
Hipposideros lylei	6.7	3.2	2.2
	9.1	4.2	2.3
Hipposideros pomona	10.7	4.3	2.8
	6.1	2.7	2.4
	5.2	2.1	2.7

Table B.1: Values of major axis, minor axis and error anisotropy for the reception beampatterns in family Hipposideridae

B.2 Rhinolophidae (Reception beampatterns)

Rhinolophidae	major axis	minor axis	ratio (major/minor)
Rhinolophus acuminatus	9.3	3.7	2.9
	15.9	5.1	3.9
	14.3	5.7	3.2
Rhinolophus affinis	12.9	3.2	4.8
	14.9	5.6	3.4
Rhinolophus (Cambodia)	16.2	6.1	3.6
	17.3	6.6	3.6
	13.3	4.4	3.6
Rhinolophus (Cat Tien NP)	15.5	4.6	4.2
	16.8	6.2	3.5
Rhinolophus ferrumequinum	14.3	5.2	3.6
	7.9	2.5	3.6
	9.6	2.5	4.7
Rhinolophus luctus	18.3	6.3	4.0
Rhinolophus macrotis	15.2	4.3	5.0
	21.4	5.4	4.9
Rhinolophus malayanus	17.4	6.3	4.1
	15.3	6.2	3.3
Rhinolophus marshalli	22.3	6.4	5.4
Rhinolophus paradoxolophus	15.6	6.6	3.0
	16.0	6.2	3.3
Rhinolophus pearsoni	9.9	3.4	3.5
	14.9	5.2	3.6
	14.5	4.1	4.4
Rhinolophus pusillus	17.1	5.8	4.1
	16.0	3.7	5.6
Rhinolophus rouxi	16.5	7.0	3.0
	16.8	5.7	5.4
Rhinolophus sinicus	17.9	6.0	4.2

	15.9	5.5	3.9
	10.1	3.6	3.5
Rhinolophus thomasi	16.1	4.7	4.8
	19.4	6.1	4.6
	19.3	6.4	4.6
Rhinolophus sp.	18.8	6.9	3.8
	17.0	6.5	3.8

Table B.2: Values of major axis, minor axis and error anisotropy for the reception beampatterns in family Rhinolophidae

B.3 Vespertilionidae (Reception beampatterns)

Vespertilionidae	major axis	minor axis	ratio (major/minor)
Barbastella leucomelas	10.6	4.4	2.8
	16.6	5.9	3.8
	10.3	3.8	3.3
	16.0	5.8	3.7
	8.5	2.9	3.5
Eptesicus serotinus	10.7	5.0	2.4
	7.4	3.3	2.4
iaio	11.0	3.3	3.9
	11.1	5.0	2.5
	10.9	5.1	2.5
	8.7	4.2	2.2
	10.1	3.4	3.2
	17.0	6.2	3.9
	10.9	5.1	2.5
	9.1	3.7	2.7
	9.7	3.7	2.9
	8.5	4.1	2.3
	9.6	4.0	2.6
	12.3	4.6	3.2
	8.1	4.1	2.2
	8.1	3.0	2.9
	10.4	4.3	2.7

Kerivoula sp	8.0	3.8	2.3
	7.7	3.2	2.7
	7.7	3.3	2.5
	8.7	4.1	2.4
	7.6	2.9	2.8
	7.0	2.8	2.8
Miniopterus schreibersi	5.3	2.7	2.1
	8.9	3.8	2.6
	9.1	4.1	2.5
	8.5	4.2	2.2
Murina Cyclotis	7.5	2.9	2.7
	7.9	3.6	2.4
	10.9	4.7	2.5
	11.5	4.8	2.6
	10.8	3.1	4.0
Myotis altarium	12.5	4.4	3.3
	11.4	4.6	2.8
Myotis blythii	8.9	3.5	2.9
	8.0	3.4	2.6
	5.4	2.1	2.8
	9.6	3.7	2.9
	7.8	2.1	4.3
Myotis formosus	7.9	3.5	2.5
	7.1	3.1	2.5
Myotis natterer	6.6	3.3	2.2
	6.6	3.3	2.2
	9.5	4.5	2.3
Myotis ricketti	13.0	5.2	3.0
	12.6	5.0	3.0
	10.7	4.9	2.6
Myotis sp.(myosp)	8.4	3.5	2.7
	8.9	4.1	2.4
	6.9	3.0	2.5
	7.9	3.3	2.7
Myotis sp.(myovsp)	9.0	3.3	3.1
	6.5	2.8	2.8
	8.5	3.0	3.3
Myoxxxx	8.4	3.5	2.7

	8.9	4.1	2.4
Nyctalus noctula	12.8	5.8	2.5
	12.0	5.5	2.5
	10.1	3.9	2.8
	11.6	5.2	2.5
Nyctalus plancyi	5.4	2.7	2.2
	6.1	2.8	2.4
Pipistrellus nathusii	12.6	5.3	2.7
	14.3	5.5	3.9
Pipistrellus pipistrellus	13.9	5.7	3.1
Pipistrellus sp.	12.9	5.5	2.6
	12.1	5.6	2.6
	12.3	5.7	2.6
	11.8	4.9	2.7
Pipistrellus sp.	10.1	3.4	3.4
Plecotus auritus	10.0	3.6	3.3
	6.3	2.6	2.7
	6.6	3.0	2.5
Scotophilus sp.	11.8	5.2	2.6
	8.6	3.4	3.0
	10.4	5.0	2.4
Scotophilus kuhlii	10.6	4.4	2.8
	12.8	2.8	5.7
	8.8	3.7	2.7
	6.7	3.0	2.5
Scotomanes ornatus	9.7	4.3	2.6
	10.1	4.8	2.4
Tylonycteris pachypus	10.1	3.6	3.0
	12.5	5.7	2.5

Table B.3: Values of major axis, minor axis and error anisotropy for the reception beampattern in family Vespertilionidae

B.4 Pteropodidae (Reception beampatterns)

Pteropedia	major axis	minor axis	ratio (major/minor)
------------	------------	------------	---------------------

Cynopterus brachyotis	7.9	3.4	2.6
	8.8	3.4	2.8
Cynopterus sphinx	8.2	3.5	2.5
	6.1	2.1	3.1
	8.2	3.2	2.8
Eonycteris spelaea	10.3	3.8	3.0
	9.2	3.7	2.7
	11.4	4.7	2.7
Macroglossus sobrinus	10.8	1.9	6.6
	4.3	1.2	4.0
	9.9	4.6	2.4
Pteropus lylei	6.7	2.7	2.7
	8.3	3.1	2.9
	8.2	3.5	2.5
Rousettus leschenoulti	7.4	3.2	2.6
	14.2	6.0	3.0
	12.3	4.9	2.9

Table B.4: Values of major axis, minor axis and error anisotropy for the reception beampattern in family Pteropedia

B.5 Megadermatidae (Reception beampatterns)

Megadermatidae	major axis	minor axis	ratio (major/minor)
Megaderma lyra	5.0	2.1	2.6
	2.6	1.2	2.3
	6.3	2.9	2.3
Megaderma spasma	3.0	1.3	2.4
	3.9	1.9	2.2
	5.0	1.4	3.9

Table B.5: Values of major axis, minor axis and error anisotropy for the reception beampatterns in family Megadermatidae

B.6 Molossidae (Reception beampatterns)

Molossidae	major axis	minor axis	ratio (major/minor)
Tadarida teniotis	13.8	5.4	3.6
	13.7	5.2	3.2
	15.1	6.1	3.4

Table B.6: Values of major axis, minor axis and error anisotropy for the reception beampatterns in family Molossidae

B.7 Hipposideridae (Emission beampatterns)

Hipposideridae	major axis	minor axis	ratio (major/minor)
Aselliscus stoliczkanus	4.4	1.9	2.6
	5.6	2.2	2.8
	3.9	1.7	2.5
Asellia tridens	12.7	6.3	2.4
	7.9	3.9	2.2
	7.7	3.8	2.2
Coelops frithii	6.2	3.5	1.9
	7.1	3.7	2.0
	5.2	2.9	1.8
Hipposideros armiger	3.7	2.2	1.8
	3.1	1.8	1.8
	4.9	2.5	2.1
Hipposideros caffer	7.3	4.1	1.9
	7.7	3.8	2.1
	8.5	4.0	2.2
Hipposideros cervinus labuanensis	7.6	3.9	2.1
	6.3	3.6	1.8
	7.8	3.8	2.1
Hipposideros cineraceus	8.8	4.0	2.4
	6.5	3.8	1.8
	10.0	3.7	2.8
Hipposideros commersoni	5.4	2.9	1.9
	4.5	2.5	1.8

	3.6	1.6	2.4
Hipposideros diadema griseus	5.1	3.0	1.8
	5.8	3.3	1.8
	3.3	1.8	1.9
Hipposideros dyacorum	7.5	4.1	1.9
	10.6	5.2	2.3
	8.0	4.3	1.9
Hipposideros galeritus galeritus	7.6	4.1	1.9
	8.4	4.3	2.1
	10.7	5.7	2.1
Hipposideros lankadiva	10.3	3.9	3.1
	7.4	3.1	2.5
	4.2	1.9	2.3
Hipposideros larvatus neglectus	4.3	2.4	1.9
	8.2	4.6	1.9
	7.5	4.2	1.9
Hipposideros lylei	4.9	2.8	1.8

Table B.7: Values of major axis, minor axis and error anisotropy for the emission beampatterns in family Hipposideridae

B.8 Rhinolophidae (Emission beampatterns)

Rhinolophidae	major axis	minor axis	ratio (major/minor)
Rhinolophus acuminatus	5.3	2.6	2.1
	6.9	3.1	2.4
	5.5	2.6	2.3
Rhinolophus affinis	4.8	2.0	2.7
	6.2	2.2	3.1
	4.7	2.2	2.3
Rhinolophus celebensis	9.7	4.4	2.4
	9.8	4.8	2.3
	6.4	3.2	2.2
Rhinolophus denti	7.4	3.6	2.2
	12.9	5.0	3.1
	11.2	5.2	2.5

Rhinolophus ferrumequinum	6.9	2.4	3.3
	6.9	2.4	3.3
	8.1	3.3	2.7
Rhinolophus landeri	11.6	2.7	5.1
	14.9	5.7	3.5
	12.1	5.1	2.9
Rhinolophus luctus	11.4	4.6	2.9
	9.7	3.8	2.9
	12.3	3.5	4.3
Rhinolophus macrotis	12.5	3.7	4.4
	19.3	5.9	6.7
	16.8	5.8	5.6
Rhinolophus marshalli	17.5	5.1	4.8
	19.4	5.0	6.4
Rhinolophus mehelyi	12.6	3.8	4.2
	15.3	5.4	4.4
	17.3	5.7	5.1
Rhinolophus paradoxolophus	7.7	3.0	2.7
	7.3	2.7	3.0
	7.5	2.7	3.2
Rhinolophus pearsoni	7.6	3.5	2.4
	10.6	3.6	3.5
	11.5	3.7	3.8
Rhinolophus pusillus	16.4	5.2	4.8
	12.7	3.1	5.1
	14.2	4.1	5.1
Rhinolophus rex	17.2	3.8	6.0
	11.6	4.4	3.1
Rhinolophus sedulus	10.8	4.8	2.6
	11.3	4.6	3.0
Rhinolophus thomasi	9.5	3.5	3.0
	10.0	3.2	3.6
	12.2	3.5	4.4
Rhinolophus trifoliatus	13.1	3.6	4.6
	15.5	3.8	6.0
	16.7	4.3	6.0
	14.9	3.9	5.6

Table B.8: Values of major axis, minor axis and error anisotropy for the emission beampatterns in family Rhinolophidae

B.9 Phyllostomidae (Emission beampatterns)

Phyllostomidae	major axis	minor axis	ratio (major/minor)
Artibeus jamaicensis	9.5	4.8	2.3
	6.3	3.8	1.7
	6.6	4.0	1.8
Brachyphylla cavernarum	9.5	3.7	2.8
	8.3	3.5	2.5
	9.6	3.7	2.9
Chrotopterus auritus guiana	8.6	3.5	2.8
	14.6	4.8	4.3
	9.5	3.5	3.2
Desmodus rotundus	9.1	3.5	3.0
	7.2	3.4	2.2
	9.8	4.2	2.6
Diaemus youngi	8.8	4.2	2.2
	12.1	4.7	2.9
	7.5	4.0	2.0
Erophylla sezekorni	12.5	3.8	4.0
	12.8	4.3	3.5
	15.1	4.1	4.2
Lonchorhina orinocensis	8.0	4.3	2.0
Lonchophylla thomasi	6.7	3.3	2.1
	10.3	4.9	2.2
	9.4	4.7	2.1
Phyllostomus discolor	9.6	4.8	2.1
	8.0	3.7	2.3
	6.5	3.5	2.0
Phyllostomus hastatus panamensis	17.5	6.7	3.8
	13.7	5.9	2.7
	14.0	6.3	2.7
Platyrrhinus helleri	7.0	2.9	2.6

	6.3	3.1	2.2
	4.8	2.5	2.0
Phaeronycteris toxophyllum	5.7	3.1	1.9
	7.1	3.6	2.1
	6.1	3.2	2.0
Trachops cirrhosus	6.2	3.5	1.9
	8.0	3.7	2.4
	6.2	2.9	2.3
Vampyrum spectrum	4.3	2.0	2.3
	4.2	2.1	2.1
	3.6	1.9	1.9

Table B.9: Values of major axis, minor axis and error anisotropy for the emission beampatterns in family Phyllostomidae

B.10 Nycteridae (Emission beampatterns)

Nycteridae	major axis	minor axis	ratio (major/minor)
Nycteris arge	5.6	2.6	2.4
	6.4	2.8	2.6
	7.1	3.2	2.4
Nycteris aurita	5.7	2.5	2.6
	6.0	2.9	2.3
	6.5	3.1	2.2
Nycteris grandis	7.4	3.6	2.3
	6.0	2.7	2.5
	7.3	3.2	2.5
Nycteris hispida	7.5	3.5	2.3
	7.2	3.3	2.5
	8.5	3.5	2.8
Nycteris intermedia	5.2	2.2	2.7
	5.1	2.6	2.1
	7.5	4.2	1.9
Nycteris javanica	7.2	3.6	2.1
	6.0	2.8	2.4
	6.6	3.3	2.2

Nycteris thebaica	5.4	2.5	2.3
	6.7	3.2	2.3
	6.7	3.1	2.5
Nycteris tragata	5.0	2.3	2.4
	6.4	3.2	2.3
	7.5	3.6	2.3

Table B.10: Values of major axis, minor axis and error anisotropy for the emission beampatterns in family Nycteridae

B.11 Megadermatidae (Emission beampatterns)

Megadermatidae	major axis	minor axis	ratio (major/minor)
Cardioderma cor	5.5	2.9	2.0
	6.3	3.2	2.2
	6.0	3.2	1.9
Macroderma gigas	6.2	3.4	1.9
	6.5	3.7	1.8
Megaderma lyra	4.6	2.1	2.4
	5.6	3.2	1.9
	4.6	2.2	2.3

Table B.11: Values of major axis, minor axis and error anisotropy for the emission beampatterns in family Megadermatidae

B.12 Molossidae (Emission beampatterns)

Molossidae	major axis	minor axis	ratio (major/minor)
Nycteris macrotis	6.3	2.9	2.4
	8.5	3.8	2.4
	7.9	3.1	2.8

Table B.12: Values of major axis, minor axis and error anisotropy for the emission beampatterns in family Molossidae